博士論文

Study on Electrical Conductivity and Thermoelectric Properties of Redox Active Coordination Polymers
(酸化還元活性な配位高分子の電気伝導性及び熱電特性に関する研究)

Shraddha Gupta

2022

Abstract

Metal-organic frameworks (MOFs) are among the most studied materials in the last three decades because of their diverse applications in nanotechnology, chemistry, physics and medicine. [1] They belong to a new class of porous materials. Because of their extraordinary features, such as large surface area, permanent porosity and chemical tunability, this field has been explored, for a wide range of applications, such as gas storage, [2–7] gas separation,[7–12] sensing and catalysis.[14–19] Moreover, other than the typical use of MOF for gas storage and separation, they also have the potential to be explored as an energy storage device,[20–24] capacitors,[25] and electrocatalysis,[26–30] conducting materials[31–35] etc. But unfortunately, these applications are limited by the insulating and redox inactive nature of the MOFs.[36] Although, a revolutionary change was realized in the field of electrically conductive MOFs. In recent years, various strategies have been introduced, including designing, synthesizing, and post-synthetic modifications etc., through which the electrical conductivity can be modified.[37] There are two ways through which conductive MOFs can be realized. One is a direct method, in which conductive MOFs are synthesized by incorporating strategies such as through bond, through space, and conjugated planes. Most of these MOFs have intrinsic conductivity. Another method is a post-synthetic modification, which includes modification of the electronic state of the MOFs by means of incorporating electroactive guest molecules such as TCNQ, Iodine, polyiodide etc. This strategy turns out to be miraculously helpful for the MOFs, which possess very low intrinsic conductivity. Doping redox-active guest molecules into the pores of the MOF can modify the electronic state of MOFs and contribute to the enhancement of conductivity, employing either guest-guest or guest-host interactions. Iodine and

polyiodide doping is mostly explored for the guest-promoted enhancement of electrically conductive MOFs.[31,38–42] There are plenty of studies on conductive MOFs that have been reported in the last ten years. Researchers are only focusing on obtaining electrically conductive MOFs, and almost no focus has been paid to the fundamental electronic properties such as conductive carrier types and power factors of the MOFs. In this work, we reported new conducting coordination polymers and investigated the charge carrier type by measuring thermoelectromotive force. Thermoelectric force is basically the generation of open circuit voltage across a material when there is temperature difference applied. Thermoelectric property is one of the powerful tools to investigate the electronic structure and the efficiency of thermoelectric materials. One of the applications of thermoelectromotive force is that it can give you information about the majority of charge carriers responsible for the conduction and information about the Fermi energy level. The positive and negative sign of the Seebeck coefficient indicates the majority of charge carriers are holes and electrons, respectively.

Chapter 2. In this study, we investigated the effect of continuous and controlled halogen doping on structural, optical, semiconducting and thermoelectric properties of $Cu[Cu(pdt)_2]$ (pdt = 2,3-pyrazinedithiolate). $Cu[Cu(pdt)_2]$ is a prototype of electron conductive MOF [43] and possesses permanent porosity (a BET surface area of 280 $m^2 g^{-1}$).[44] Halogen doping was performed by exposing $Cu[Cu(pdt)_2]$ to Br_2/I_2vapor in an N_2 atmosphere. We Studied the effect of stoichiometric halogen doping on structural, optical semiconducting and thermoelectric properties of the doped MOF. The MOF skeleton was maintained upon halogen doping, which implies that halogen doping does not change the intrinsic structure of the MOF. Whereas the unit cell parameter continuously changed.

Interestingly, we illustrated that the same material could behave as both p- and n-type semiconductors while tuning the stoichiometry of the doped Br/I in $Br_x/I_x@Cu^{II}[Cu^{II}(pdt)_2]$. This means that a change in the conducting carrier was realized, and the mode of transportation has changed from holes in pristine MOF to electrons upon doping of a certain fraction of halogen. Halogen molecules act as an oxidizing agent, Which causes the selective oxidation of $[Cu^{II}(pdt)_2]^{2-}$ in the host framework to form $[Cu^{III}(pdt)2]–$. The electrical conductivity measurements indicate an enhancement of 10-fold of conductivity upon doping.

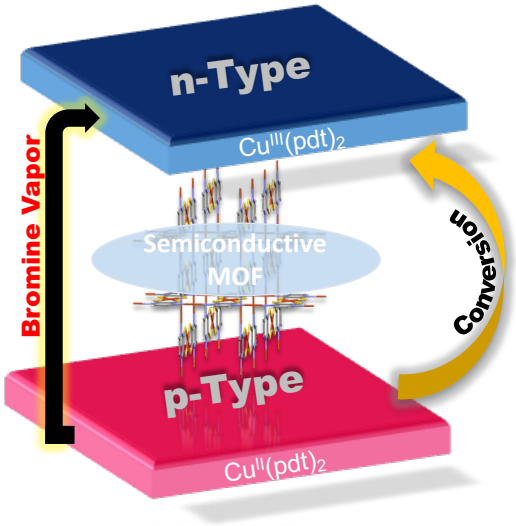

Chapter 3. Besides 2,3-pyrazinedithiolate ligand, we also explore $dhbq^{2-}$ based MOF $[Fe_2(dhbq)_3]$. Coordination polymers of 2,5- dihydroxy-1,4- benzoquinone and its derivative have been immense out as a new exciting material because of the appealing feature of acquiring variable oxidation states.[46] Redox activity and lower molecular weight of $dhbq^{n-}$ based ligands further provides the opportunity to be explored as a high energy-

density storage material. There are two important factors that needs to be considered to enhance the specific capacity of a material, 1. Low-density molecules, which can be obtained by removing the possibility of cations. Larger cations usually occupy the pore of the MOF, which also limits the application of MOFs for further doping purposes. 2.Both the metal and ligands should possess redox activity. Herein, we report the synthesis, characterization and physical properties of three-dimensional neutral conducting MOF based on 2,5-dihydroxy-1,4-benzoquinone ligand without using any cation, formulated as $[Fe_2(dhbq)_3]$, having a molecular weight of 525.92. The MOF buildup of Fe(III) and $dhbq^{2-}$ ligand exhibit redox activity based on both metal and ligand with a theoretical capacity of 408 mAh / g. It showed relatively high electrical conductivity of 1.6×10^{-2} S cm^{-1} as a consequence of strong d-π conjugation, which corresponds to the strong covalency between metal and ligand. Thermoelectromotive force measurements showed that it has electrons as a majority of charge carriers, and so it behaves as an n-type semiconductor. Nitrogen adsorption illustrates that unlike the other reported benzoquinone derivatized three dimensional MOFs, it shows permanent porosity with a pore diameter of 0.46 nm. We further explored the redox activity and electrochemical behaviour of $[Fe_2(dhbq)_3]$ and reported that it shows redox activity based on metal as well as ligand with a first discharge capacity of 322 mAh / g. Redox behavior of the Fe was evidenced by ex-situ XANES spectral analysis. Magnetic properties showed that the MOF showed antiferromagnetic coupling at a lower temperature range.

Chapter 4. Dithiolene-based metal complexes have gained considerable attraction over the last few decades due to their curious electronic structure and interesting solid-state properties like molecular conductors and superconductors. In the case of molecular

conductors, designing strategy is very important. Stacks of the square planar dithiolene-based metal complexes are one of the prelim requirements for the SCMM. Which provides a delocalized band structure upon establishing effective orbital overlapping between the two stacks. In this chapter, a new semiconducting $Na[Pt(pdt)_2].2H_2O$, 3-D coordination polymer with a face-to-face stacked arrangement, was reported. We investigated the electrical conductivity, conduction carriers and mode of charge transportation. Coordination polymer was synthesized using electro-crystallization method, and black fiber-like single crystals were obtained. Crystal structure analysis reveals a strong π-π interaction between the ligands in the '*a*' direction, resulting in a 3D extended framework as shown in **Figure 4.1**. Complete face-to-face stacking of the *bc* plane caused effective overlapping of wave function between the planes and results in an extraordinary conductivity of the order 10^{-2} S cm^{-1}. Single crystal conductivity measurements showed a relatively high electrical conductivity of 1.6×10^{-2} Scm^{-1} at 300K which was the highest among the other pdt^{2-} based coordination polymers.[45] Thermoelectromotive force measurements showed that it possesses holes as a majority of charge carriers, and hence it is a p-type semiconductor.

Contents

Chapter1. Introduction

1.1 Metal organic Frameworks

Metal-organic frameworks (MOFs) are among the most studied materials in the last three decades because of their diverse applications in the field of nanotechnology, chemistry, physics and medicine.[1] It belongs to a family of porous materials and is also known as porous coordination polymers. They are constructed with metal clusters and are connected with the help of an organic ligand as a linker to yield one-, two or three-dimensional coordination polymers.

This field has gained immense attention because of the extraordinary features it has, such as functional diversity, structural flexibility and chemical tunability. The striking features of a MOF are its large surface area, permanent porosity and chemical tunability.[36] Moreover, all of these properties can be tuned upon modifying its building blocks which include linkers as well as metal ions. There are three significant characteristics, 1. inorganic parts which is constructed of metal clusters, 2. organic ligands and 3. the topology of frameworks.[53] Length of the organic ligand between two SBUs units and the expanded size of metal cluster ensures the high porosity of the framework. Longer the length of the ligand, more will be the pore diameter. And the topology of the MOF can be controlled by changing the conformation of ligands as a result of incorporating the steric effect.[54] Because of their striking features such as chemical stability, porous structure and high surface area, it has been explored a lot in the field of gas storage,[2–7] gas separation,[7–12] sensing and heterogeneous catalysis,[14–19] drug delivery. The flexibility to modify the interiors of MOF, such as introducing unsaturated open metal sites and linkers with various functional groups, makes it more promising to adsorb gas molecules by enhancing the interaction with the MOF surface.[54]

The diversity of metal cations ranging from monovalent to tetra valent and a variety of ligands including carboxylate, phosphonates, oxo, nitrogen, and sulfur donor atoms create more scope for research. The freedom of suitable flexibility opens myriads of opportunities for researchers to explore its physical and chemical properties.[1]

1.2 Conducting MOFs

Other than the typical use of MOF for gas storage and separation, they also have the potential to be explored as an energy storage device,[20–24] capacitors,[25] and electrocatalysis,[26–30] conducting materials[31–35] etc. But unfortunately, these applications are limited by the insulating and redox inactive nature of the MOFs. Unsurprisingly, a vast majority of MOFs reported in last two decades were insulating in nature because of fully occupied metal orbitals (closed shell metal center), insulating nature of organic linkers which are often constructed with redox inactive ligand and their poor spatial orbital overlapping.[36] And that is why only a handful of reports are there in the field of electronics. However, over the last few years, a revolutionary change has been realized in the field of electrically conductive MOFs. A variety of strategies have been introduced over the years, including designing, synthesizing, and post-synthetic modifications etc., through which the electrical conductivity can be modified.[37] As a result of which, the field is expanding at an enormous rate. And a number of reports on conductive MOFs is coming very frequently. This consequently opens doors of opportunities for energy storage, electrochemical sensor, electrical devices, thermoelectric materials etc.

Electrical conductivity is a fundamental property of a conductive MOF. It is determined as the equation 1 given below. [37]Charge density (η) and carrier mobility (μ) are the two deciding factors for a material to be conductive.

$$\sigma = e\ (\mu_e \eta_e + \ \mu_h \eta_h) \qquad \text{equation 1}$$

$\sigma =$ Electrical conductivity
$\mu =$ Mobility of electron
$\eta =$ Carrier density
$e =$ Charge on electron
e and $h =$ electrons and holes respectively

In a framework, high-energy electrons and holes could be a charge carrier. They can be derived from metal centre, or redox-active ligands such as TTF, X_2dhbq etc.[55] Along with the redox active motif, effective frontier orbital overlapping between metal and ligand ensures the charge mobility.

1.3 Mechanism involves in charge transportation of MOFs

Fundamentally there are two modes of transportation, 1. hopping transport and 2. bandlike (ballistic) are responsible for the charge transport in conductive MOFs.[37] In hopping transportation, the charge transport takes place by means of jumps between discrete nonbonded sites, i.e. stepping from one localized state to another, as shown in **Figure 1.3.1a**. Common examples are organic semiconductors and glasses. On the other hand, in the latter one, the charges are allowed to move in delocalized energy levels **(Figure 1.3.1b)**, which are formed as a result of strong interaction between the metal centre and ligands. Inorganic materials often follow this mode of transportation. So

basically, materials formed by strong covalent bonding are expected to follow band-like transportation whereas ionic material are supposed to follow the hopping mechanism.

Figure for band like and hopping transportation

a)

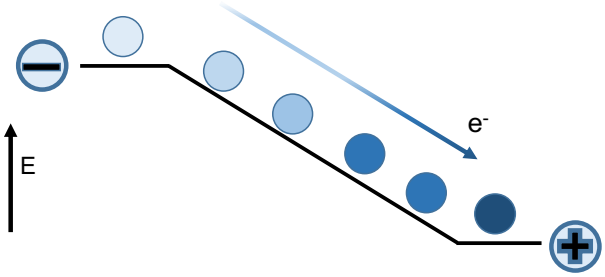

b)

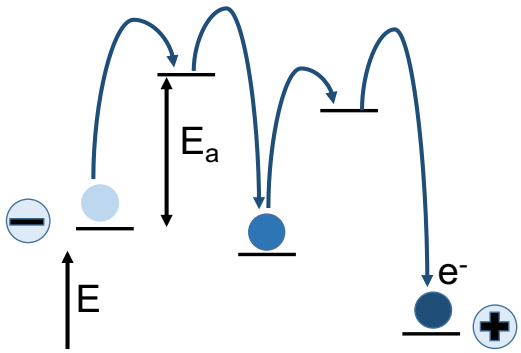

Figure 1.3.1 Schematic representation of **(a)** band like transport and **(b)** hopping transport.

MOF-based semiconductors often follow band-like transportation mechanisms. And their conductivity shows an Arrhenius dependency, $\sigma = \sigma_o \exp\left[-\left(\frac{E_a}{kT}\right)\right]$. Where E_a term

represents activation energy and the value of it gives the band gap width. **Figure 1.3.2** illustrates the band structure of the metal, semiconductor and insulator.

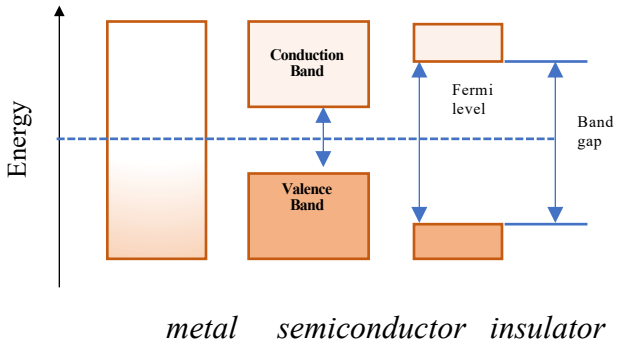

Figure1.3.2 Energy band diagram of metal, semiconductor and insulator.

1.4 Mode of transportation in conductive MOFs

Design and strategies

A number of strategies have been introduced over the last few years in order to design and synthesize electrically conductive MOFs. For example, Through-Bond Pathways, Extended Conjugation, Through-Space Pathways, Redox Hopping and last but not least Guest-Promoted Transport.[37]

1.4.1 Through-Bond Pathways: As the name suggest well-matched energy levels and effective overlapping of orbitals ensure the facile charge transportation. Through bond mainly focuses on the bonding between metal center and the ligands irrespective of the organic core of the ligand. (**Figure 1.4.1**) The stronger the bonding between them, the more efficiently they promote the charge transportation. This strategy utilizes softer ligands, for example Nitrogen, Sulphur (-M-S-) based, unlike traditionally used carboxylate-based(-M-O-) linkers.[55] Because the softer ligands provide well-matched

energy levels and effective orbital overlapping in contrast to ionic bonding, which in turn results in narrow band gaps and allow significant charge mobility.[56–58] Whereas the carboxylate-based linkers lead to the ionic bonding between ligands and the metal center, which lacks the effective orbital overlapping and hence results in localized energy levels which lead to lower conductivity. 1-D pathway[56–58] is the most common among 2-D and 3-D.[59,60]

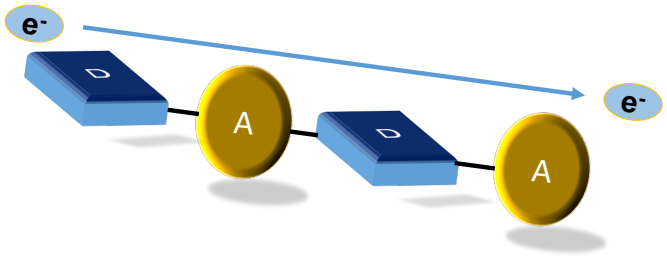

Figure 1.4.1 Through-bond pathways for charge transportation in conducting MOFs

1.4.2 Extended Conjugation

Extended conjugation is also known as the through plane pathway. Where the strategy is to pairing metals with ligands which possess conjugated organic core and chelating functional groups for example dithiols, diamines, ortho-diols.[37] The critical point to keep in mind is that binding atoms should possess the same energy level and should be in conjugation with the core of the ligand in order to facilitate the charge transportation. 2D MOFs with above-mentioned ligands have been considered as the analogues of graphene, and d-π conjugation in a 2D plane allows effective delocalization of charges, and MOFs having such a system showed the highest conductivity among the others.[61–63]

1.4.3 Through-space pathways

MOFs with organic components having π- π interactions can lead to charge transportation through-space pathways. Small separation between the stacked layer causes the overlapping of the wave function in the stacked direction and hence creating charge transport pathways. (**Figure 1.4.3**) In contrast to metal-ligand bonding, it focuses on the intermolecular interaction of ligands only. Common examples of organic components that possess π- π stacking are planar conjugated ligands such as tetracyanoquinodimethane (TCNQ),[64–66] tetrathiafulvalene (TTF),[67–69] anthracene, naphthalene naphthalenediimide.[70–72]

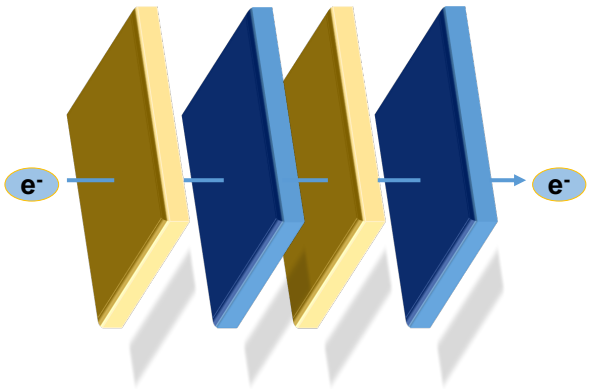

Figure 1.4.3 Through-space pathways for charge transportation in conducting MOFs.

1.4.4 Redox Hopping

It is quite difficult to distinguish, through which mechanism charge transport is taking place (band-like or hopping). Some MOFs which do not possess crystallographic pathways responsible for band-like transport can be categorized under the hopping transport mechanism. In such materials, the presence of redox-active metals or linkers, as well as the close distance between them, can promote charge hopping.[73–75] However, in some cases, they contain redox-active moiety, and those are separated enough to avoid the

orbital overlap. In these cases, charge hopping is the most probable conduction mechanism. Hopping could be categorized into three parts. 1. Metal based, 2. Ligand-based and 3. Mixed metal and ligand-based.

1.4.5 Guest promoted

It is also recognized as post-synthetic modification strategy, where; redox active guest molecules are introduced into the pores of the MOFs. And they can contribute to the enhancement of conductivity employing either guest-guest or guest-host interactions. This strategy turns out to be miraculously helpful for the MOFs, which possess very low intrinsic conductivity. The most common interaction that led to an increment in the conductivity is charge transfer between the guest and the framework. Other than that, guest molecules can also act as oxidants or reductants for the frameworks and can modify the electronic structure of the MOF. Iodine and polyiodide doping is the most familiar example of the guest-promoted enhancement of electrically conductive MOFs. [31,38–41]

1.5 Redox Active MOFs

Redox-active MOFs are categorized as a unique class of MOFs. And are known for their unique properties to show the switchable physical behaviour upon modulating the redox state of the material. It has attracted new exciting research interest in the field of Energy storage,[21,22] porous conducting polymers,[76,77] magnetism,[78,79] electrochemical sensing[80] and electrocatalysis. Redox activity of the MOF can be realized by incorporating redox-active metal or ligand as a building block material, or in the case of post-synthetic

modification, doping of electroactive material is performed in order to make it redox-active. Some of the redox active ligands are mentioned in **Figure 1.5.**

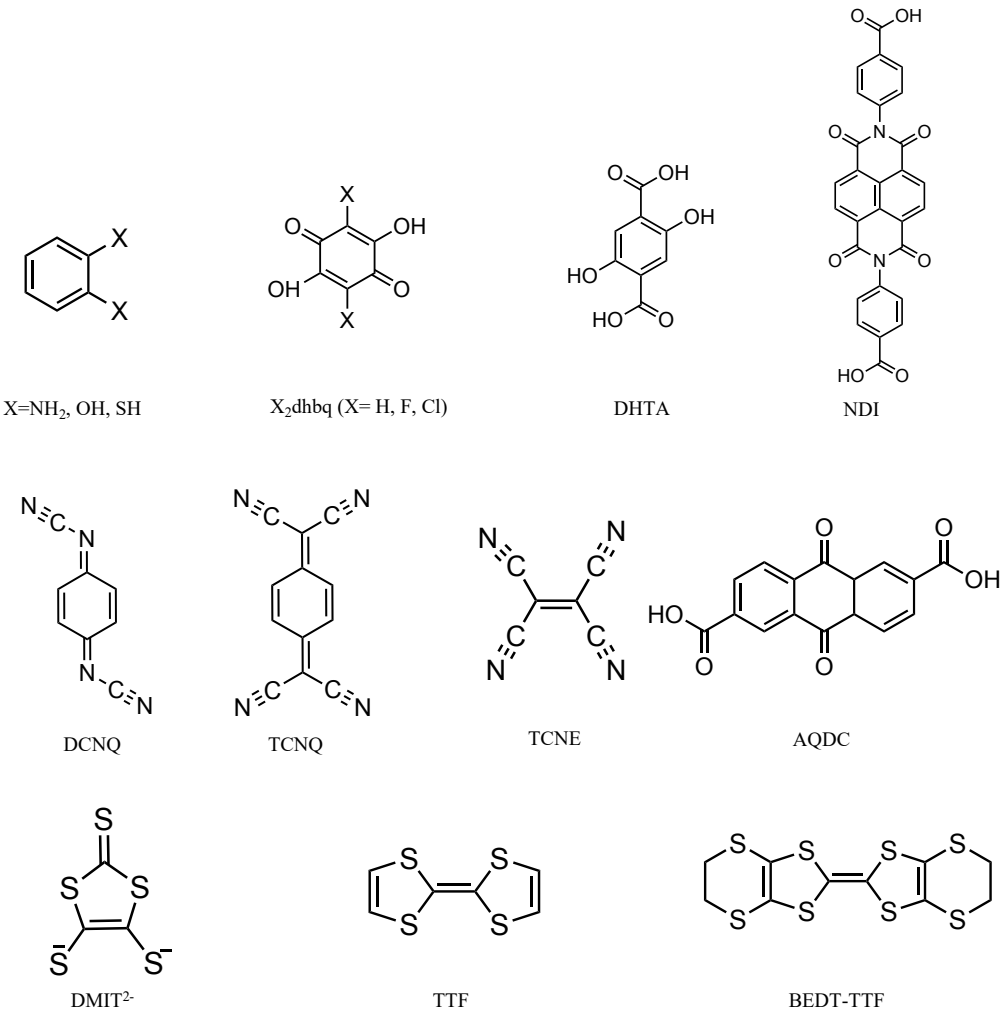

Figure 1.5 List of some of the famous redox active ligands.

1.6 Application of Redox active MOFs

1.6.1 Energy storage

Awaga and coworker have reported the MOF-based cathode material for the purpose of lithium-ion battery. Where the MOF exhibited redox activity based on metal as well as ligand and possess permanent porosity. They reported a 2-D redox-active Cu(2,7-AQDC) (2,7- H_2AQDC = 2,7-anthraquinonedicarboxylic acid) MOF.[81] Anthraquinone and the copper exhibits $2e^-$ and $1e^-$ reversible redox activity respectively. The permanent porosity of the MOF provides the large no of Li-ion insertions, and redox activity of both metal and ligand provides more electrons uptake. The Charge-discharge profile reveals that it possesses a specific capacity of 147 $mAhg^{-1}$ during the first cycle, which was comparable to the conventionally used inorganic material, i.e., $LiCoO_2$ (148 $mAhg^{-1}$). (**Figure 1.6.1.1**) However, within 50 cycles, it has decreased and stabilized to 105 $mAhg^{-1}$. Although it exhibited multiple redox activities, but the theoretical capacity is not so large as compared to inorganic materials. One reason for this is the lower conductivity of the MOF towards the charge transfer and another one could be the irreversible transportation of lithium ions through the pores because of the inhomogeneity of the crystal size. The Large molecular weight of H_2AQDC limits the high theoretical specific capacity.

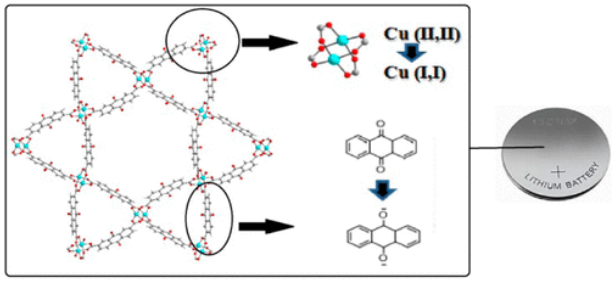

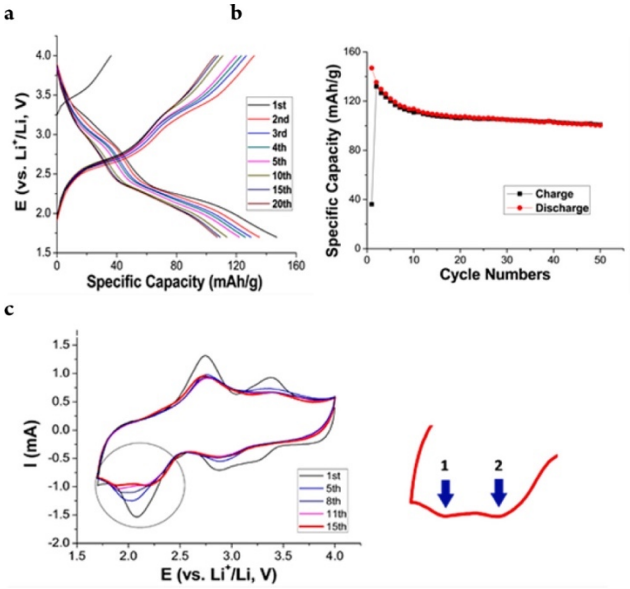

Figure 1.6.1.1 (a) Charge–discharge profile of MOF battery (10 wt % active material) **(b)** Cyclic performance of battery up to 50 cycles. **(c)** Solid state cyclic voltammetry of battery. Where arrow 1 and 2 indicates the separation of the two reduction peaks. Reprinted with permission.

Considering the impact of lower molecular weight on the specific capacity, our group recently came up with 2,5-dihydroxy-1,4-benzoquinone based one dimensional [Fe(dhbq)] MOF [22] having a molecular weight of 193.9g. Fe(dhbq) MOF is an electrically conductive MOF synthesized using 2,5-Dihydroxy-1,4 benzoquinone (dhbq). Properties like Redox activity, electrical conductivity and permanent porosity made it suitable to be explored as an appealing candidate for cathode material in the secondary battery. With an electrical conductivity of 5×10^{-6} S cm^{-1} upon incorporation as a cathode material, it shows a excellent specific capacity of 264 mA hg^{-1} in the first discharge cycle. (**Figure 1.6.1.2**) Electrochemical properties were investigated using cyclic voltammetry (CV) and charge-

discharge profile in the solid-state using Fe(dhbq) as a cathode material in a LIB cell. The value of specific capacity corresponds to the $2e^-$ redox behaviour of the $dhbq^{2-}$ ligand, which was supported by solid CV.

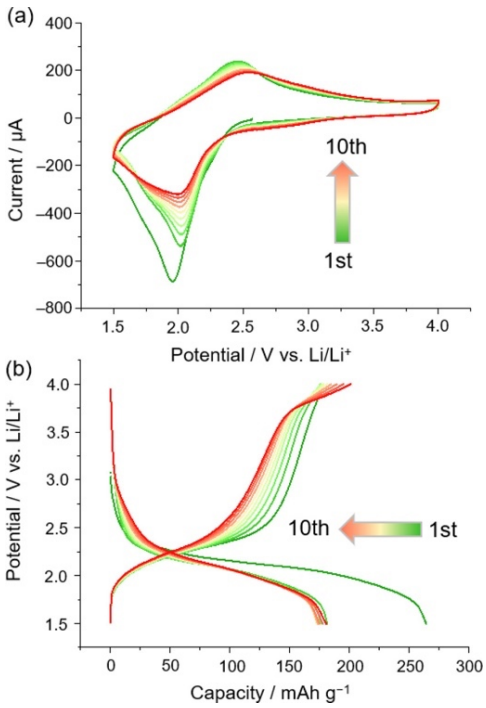

Figure 1.6.1.2 (a) Solid-state CV at a scan rate of 0.5 mV s^{-1} **(b)** Charge-discharge profile of Fe(dhbq) at a rate of 0.1 C. Working electrode consists of Fe(dhbq) (50 wt %), acetylene black (AB, 40 wt %), and polytetrafluoroethylene (PTFE, 10 wt %). Reprinted with permission.

1.6.2 Conductive MOFs

Apart from using the redox-active ligands and metals as building block units to synthesize conductive MOFs, there is another strategy to realize conductive MOFs i.e., Post synthetic modification. Post synthetic modification involves modification of the electronic state of MOFs by means of incorporating some electroactive guest molecules such as TCNQ,

iodine and polyiodide etc. This method has gained a lot of attraction among the MOFs, which are intrinsically insulating in nature. Because, doping some electroactive materials inside the pore can modify the electronic state of metal and ligand and causes an introduction of charge transportation pathways. Iodine and polyiodide doping is the most familiar example of the guest-promoted enhancement of electrically conductive MOFs.

A very famous example of the Iodine doping effect on conductivity was reported by Kobayashi et al. They reported $Cu[Ni(pdt)_2]$ (pdt^2 = pyrazine-2,3-dithiolate), [31] which is a 3D porous coordination polymer. It exhibited an electrical conductivity of the order of 1×10^{-8} S cm^{-1} quite low as compared to the it copper analogue i.e. Cu[Cu(pdt)2] ($\sigma = 6 \times 10^{-4}$ Scm^{-1}).[43] Utilizing the low reduction potential and permanent porosity of the MOF, iodine doping was performed. I_2 molecules act as an oxidizing agent and as a result causes the partial oxidation of the framework. As a consequence of that, an increment of 10^4 fold electrical conductivity was achieved (**Figure 1.6.2.1**). Partial oxidation of Ni causes the generation of high-energy free electrons as a charge carrier and redox-active ligand backbone provides through bond pathway for the charge transport between the partially oxidized Ni centre. With the aforementioned results, it was shown that the optical bandgap of the MOFs can be tuned upon doping, and it changed from 0.49 in pristine to 0.18 eV in the doped one.

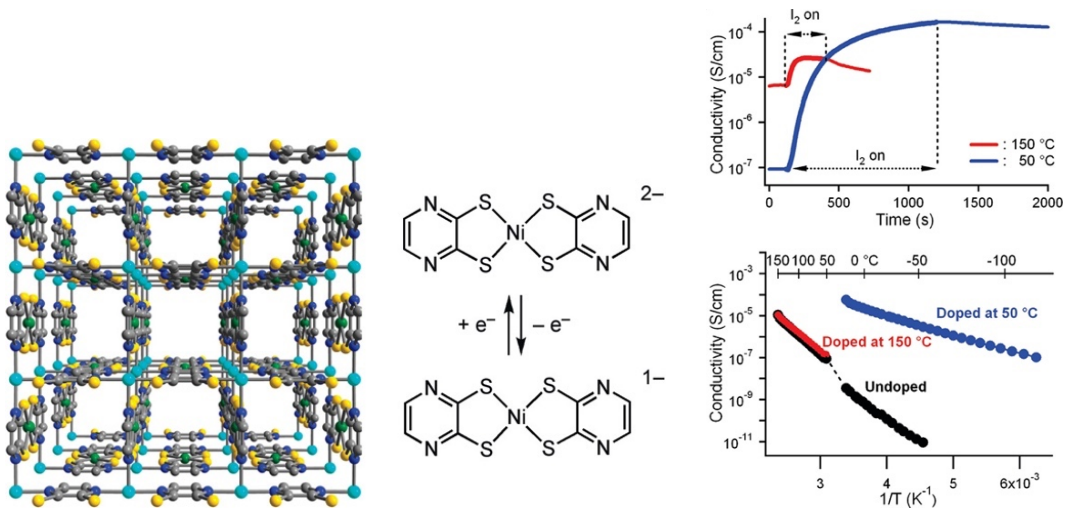

Figure 1.6.2.1 Left part represent the crystal structure of the Cu[Ni(pdt)2], (light blue (Cu), green(Ni), yellow(S), blue(N), and gray(C). Middle part shows redox behavior of $[Ni(pdt)2]^{2-}$. Right part shows conductivity details upon I_2 loading. Reprinted with permission.

Other than the iodine and polyiodide doping, porosity of MOF also provides the opportunity to large conjugated to be incorporated. Talin et al. Reported the effect of encapsulation of large conjugated molecule i.e., TCNQ in to a very well-known Cu and benzoic acid-based MOF $Cu_3(BTC)_2$ (HKUST-1; BTC, benzene-1,3,5-tricarboxylic acid).[82] The intrinsic conductivity of the pristine MOF is of the order of 10^{-8} Scm^{-1}. The author utilizes the axial coordination site of Cu centers and doped with TCNQ an electroactive material. Doping was performed after removing the water molecules by heating at 190 °C for 30 mins. The resultant MOF was immediately transferred to Saturated solution of TCNQ in CH_2Cl_2. PXRD pattern analysis revealed that TCNQ molecules occupied the axial site of copper atom and resulting a strong coupling between

Cu centers. The resultant MOF showed increase in electrical conductivity to 0.07 Scm^{-1} as a consequence of facile charge transfer (**Figure 1.6.2.2**). Further investigation suggest that TCNQ instead of acting as dopants, introduced localized region for conduction leads to the charge transfer between Cu(II) and TCNQ.

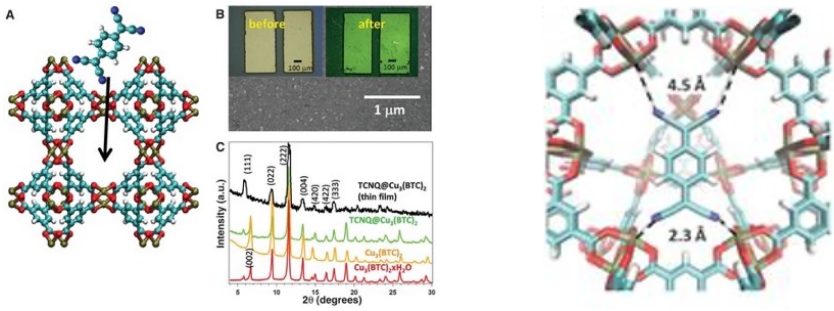

Figure 1.6.2.2 In the left half **A**. TCNQ molecule is shown along with $Cu_3(BTC)_2$ MOF. White (H), blue(N) cyan(C), red(O), light brown(Cu). **B.** SEM image along with optical image before and after TCNQ incapsulation. **C.** PXRD data for a thin film. In the right half interaction of TCNQ with MOF is shown. Reprinted with permission.

As a result of the introducing aforementioned strategies, plenty of conductive MOFs have been reported over the last one decade. All the attention was been paid on realizing a conductive MOF and investigating charge transport pathways. However, almost no attention has been paid on conductive carriers, what type of charge carriers are responsible for the current flow. Identification of conductive carriers can be performed using thermoelectromotive force measurement.

1.7 Thermoelectric properties

1.7.1 Importance of thermoelectric materials

The significance of thermoelectric materials comes from the need of renewable green source of energy.[83] A major issue of current generation is deterioration of human health and environment health because of the accumulation of the disastrous gases such as carbon dioxide, carbon monoxide and methane. Which is a major consequence of excessive use of fossils fuels. So, the current focus of research is to realize an alternate source of energy by means of opting the other earth abundant and renewable source of energy such as solar energy, wind and biomass. There is another source of energy i.e., electricity which could be converted from the heat sources. A major portion of energy got wasted in the form of heat on daily basis activities which includes fossil fuels combustion, sun light and in many industries such as chemical and nuclear reactors. These heat energies can be converted to electricity. And here, comes the role of thermoelectric materials. Thermoelectric materials are solid state-based devices that convert thermal energy into electrical energy and the process involved is called “Seebeck effect”.[83]

1.7.2 Seebeck effect

Seebeck effect is basically the generation of open circuit voltage as a result of temperature difference across the material. [84] It is the opposite of the “Peltier effect” that is generation of temperature difference upon apply voltage across the material. Thermoelectric materials can contribute in energy conservation by harvesting waste heat. The scope of the material in solving the energy problems depend on how efficient these materials are.

1.7.3 Efficiency of thermoelectric materials

The efficiency of the material is determined by the parameter called thermoelectric figure of merit represented by ZT and Carnot efficiency as shown by equation 2.

$$\eta = \frac{\Delta T}{T_{hot}} \frac{\sqrt{1 + ZT_{avg}} - 1}{\sqrt{1 + ZT_{avg}} + \frac{T_{cold}}{T_{hot}}} \qquad \text{equation 2}$$

Where,

T_{hot} = Temperature of hot end.

T_{cold} = Temperature of cold end.

ΔT = Temperature difference

T_{avg} = Average Temperature

As equation 2 indicates, efficiency of the material demands high value of both ZT as well as the temperature difference across the material.[84] So, in order to realize the high value of ZT, one should understand the factor that affects the ZT value. Equation 3 represent ZT in terms of Seebeck coefficient, electrical conductivity and thermal conductivity.

$$ZT = (S^2 \sigma/\kappa)\mathrm{T} \qquad \text{equation 3}$$

Where,

S = Seebeck Coefficient

σ = Electrical conductivity

κ = Thermal conductivity

T = Temperature

As can be seen in equation **3,** Figure of merit (ZT) is a dimensionless quantity. Moreover, for a thermoelectric material large value of ZT rely on the high electrical conductivity,

large Seebeck coefficient and low thermal conductivity of the same material. However, these parameters are not independent of each other. As illustrated by equation 3, the term $S^2\sigma$ is called Power factor and is directly proportion to the high performance. High value of it corresponds to generation of high voltage and large current. On the other hand, κ value is consisting of two factors κ_{el} and κ_{latt} as shown by equation 4.[85]

$$\kappa = \kappa_{el} + \kappa_{latt} \qquad \text{equation 4}$$

Where,

κ_{el} = Thermal conductivity of carriers

κ_{latt}=Thermal conductivity from lattice vibration.

Intuitively, equation 3 and 4 indicates that the material must possess low thermal conductivity even at large ΔT. There are two important factor that should be consider, in order to obtained Increasing value of ZT, either maximized the power factor (ZT) or minimized thermal conductivity (κ).[84] Since both the factor are not independent on each other. Hence, To fulfill these requirements, new methodology or modification of existing materials (by means of doping) is required. While improving the value of power factor, one should understand the more details about Seebeck coefficient. It is expressed in the form of Mott equation as shown below.[86]

$$S = \frac{\pi^2}{3}\frac{k^2T}{e}\frac{dln\sigma(E)}{dE}\ at\ E = E_f \qquad \text{equation 5}$$

Where,

σ (E) = Electrical conductivity as a function of Fermi energy (E_f)

K = Boltzmann constant

The above equation indicates that Seebeck coefficient is directly related to the logarithmic derivative of density of state and is basically variation of σ (E) above and below the fermi level. Large value of lnσ(E) indicates the rapid change of DOS at fermi level and is the expected reason for larger value of Seebeck coefficient. Or in other words S signifies the asymmetry of electronic structure near fermi level. So, our aim should be to incorporate complexity in the electronic structure within a small energy range near E_f. [84]

Materials such as composites and doped compounds with complex electronic structure have a good opportunity to emerge as suitable material for high power factor.

Seebeck coefficient can also be expressed in the form of thermoelectromotive force (ΔV) and ΔT as shown in equation 6.[84]

$$S = -\frac{\Delta V}{\Delta T} \qquad \text{equation 6}$$

One of the applications of Seebeck coefficient is that it gives the information about the conductive carriers in an extrinsic semiconductor. Sign of Seebeck coefficient depend on type of majority of charge carrier. For example, p-type semiconductor will have a positive sign and n-type semiconductors will have negative sign. Let's understand the reason behind this. Let's take a n-type semiconductor and applied a temperature difference across the material. Put one end at high temperature and another end at low temperature. As a result of temperature difference across the material, electrons will try to diffuse towards cooler side and a positive potential will have to develop at hotter end to hold the electrons back in order to stop the current flow to give an open circuit situation. Since Seebeck coefficient is negative of the open circuit voltage, hence its negative for n-type

semiconductor. In contrast to n-type, negative potential will have to develop on the hotter side in case of p-type materials to hold the holes back. Hence its positive for p-type semiconductors.

a) For n-type (S < 0)

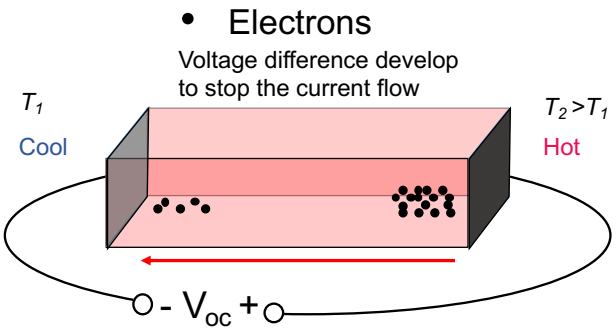

b) For p-type (S > 0)

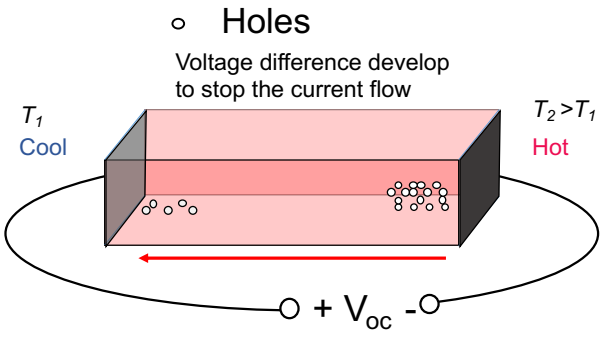

c)

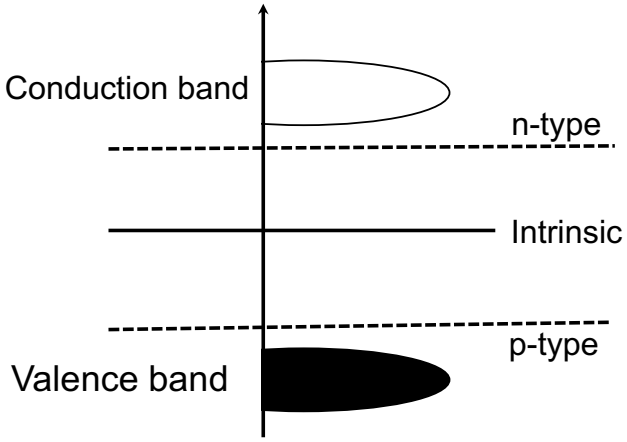

Figure 1.7.3 Schematic representation of generation of thermomotive voltage. **a)** n-type and **b)** p-type material **c)** Fermi energy of extrinsic semiconductors.

Recently, So and coworker reported theoretical and experimental perspective of charge transport properties of a 2-dimensional MOF upon metal substitution.[87] MOF is consisting of HITP (2,3,6,7,10,11-hexaaminotriphenylene) ligand and Ni as a metal center. Effect Pt doping on charge carrier type was reported. Charge carrier type was determined with the help of Seebeck coefficient measurement. And it was reported electronic structure of the MOF can be modify without changing the structure. And type of charge carrier has changed from electron to holes upon doping with Pt as evidenced by the change of sign of Seebeck coefficient from negative in pristine to positive in case of Pt doped one (**Figure 1.7.4**).

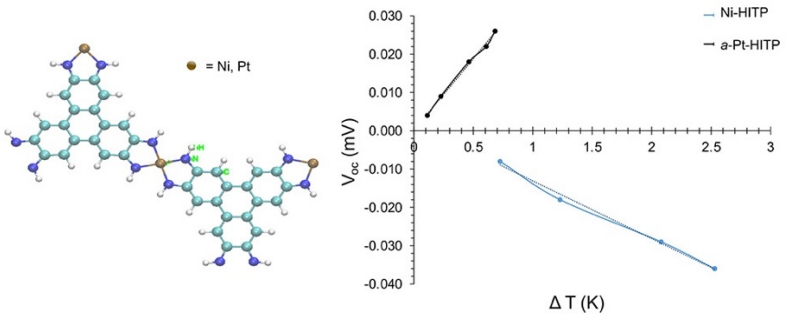

Figure 1.7.4 Left. Bonding between metal metal and HITP ligand. Right Thermoelectromotive characteristics of Ni and Pt compound. Reprinted with permission.

Recently Bao group have reported series of hexaaminobenzene (HAB) based metal organic frameworks using metals, Co, Ni, Cu. And studied the effect of changing the metal center on the electrical conductivity and the charge carrier type and the air-stability of the MOFs.[34] They reported the effect of atmospheric environment on type of charge carrier. It was found that the Cu and Co based MOFs exhibits n-type semiconductor i.e., majority of charge carriers were electrons. While Ni-HAB MOF showed change in charge carrier type from electron to holes upon changing the environment from ambient to nitrogen atmosphere. (**Figure 1.7.5**)

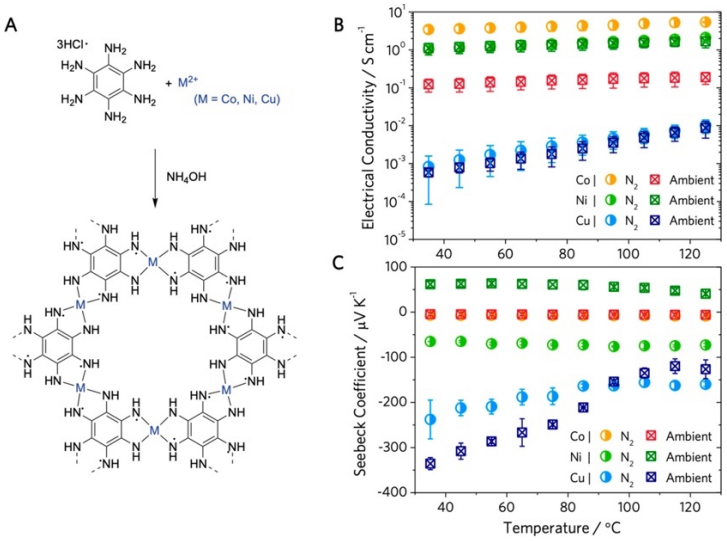

Figure 1.7.5 A. schematic representation of synthesis of MOF. B. electrical conductivity report, C. Seebeck coefficient report of M-HAB. Reprinted with permission.

References:

(1) Li, C.; Zhang, L.; Chen, J.; Li, X.; Sun, J.; Zhu, J.; Wang, X.; Fu, Y. Recent Development and Applications of Electrical Conductive MOFs. *Nanoscale* **2021**, *13* (2), 485–509. https://doi.org/10.1039/D0NR06396G.

(2) Rosi, N. L. Hydrogen Storage in Microporous Metal-Organic Frameworks. *Science* **2003**, *300* (5622), 1127–1129. https://doi.org/10.1126/science.1083440.

(3) Farha, O. K.; Özgür Yazaydın, A.; Eryazici, I.; Malliakas, C. D.; Hauser, B. G.; Kanatzidis, M. G.; Nguyen, S. T.; Snurr, R. Q.; Hupp, J. T. De Novo Synthesis of a Metal–Organic Framework Material Featuring Ultrahigh Surface Area and Gas Storage Capacities. *Nature Chem* **2010**, *2* (11), 944–948. https://doi.org/10.1038/nchem.834.

(4) Farha, O. K.; Eryazici, I.; Jeong, N. C.; Hauser, B. G.; Wilmer, C. E.; Sarjeant, A. A.; Snurr, R. Q.; Nguyen, S. T.; Yazaydın, A. Ö.; Hupp, J. T. Metal–Organic Framework

Materials with Ultrahigh Surface Areas: Is the Sky the Limit? *J. Am. Chem. Soc.* **2012**, *134* (36), 15016–15021. https://doi.org/10.1021/ja3055639.

(5) Suh, M. P.; Park, H. J.; Prasad, T. K.; Lim, D.-W. Hydrogen Storage in Metal–Organic Frameworks. *Chem. Rev.* **2012**, *112* (2), 782–835. https://doi.org/10.1021/cr200274s.

(6) Hu, Y.; Liu, Z.; Xu, J.; Huang, Y.; Song, Y. Evidence of Pressure Enhanced CO_2 Storage in ZIF-8 Probed by FTIR Spectroscopy. *J. Am. Chem. Soc.* **2013**, *135* (25), 9287–9290. https://doi.org/10.1021/ja403635b.

(7) Alezi, D.; Belmabkhout, Y.; Suyetin, M.; Bhatt, P. M.; Weseliński, Ł. J.; Solovyeva, V.; Adil, K.; Spanopoulos, I.; Trikalitis, P. N.; Emwas, A.-H.; Eddaoudi, M. MOF Crystal Chemistry Paving the Way to Gas Storage Needs: Aluminum-Based **Soc** -MOF for CH_4 , O_2 , and CO_2 Storage. *J. Am. Chem. Soc.* **2015**, *137* (41), 13308–13318. https://doi.org/10.1021/jacs.5b07053.

(8) Li, J.-R.; Kuppler, R. J.; Zhou, H.-C. Selective Gas Adsorption and Separation in Metal–Organic Frameworks. *Chem. Soc. Rev.* **2009**, *38* (5), 1477. https://doi.org/10.1039/b802426j.

(9) Chang, N.; Gu, Z.-Y.; Wang, H.-F.; Yan, X.-P. Metal–Organic-Framework-Based Tandem Molecular Sieves as a Dual Platform for Selective Microextraction and High-Resolution Gas Chromatographic Separation of *n* -Alkanes in Complex Matrixes. *Anal. Chem.* **2011**, *83* (18), 7094–7101. https://doi.org/10.1021/ac2014004.

(10) Li, J.-R.; Sculley, J.; Zhou, H.-C. Metal–Organic Frameworks for Separations. *Chem. Rev.* **2012**, *112* (2), 869–932. https://doi.org/10.1021/cr200190s.

(11) Herm, Z. R.; Bloch, E. D.; Long, J. R. Hydrocarbon Separations in Metal–Organic Frameworks. *Chem. Mater.* **2014**, *26* (1), 323–338. https://doi.org/10.1021/cm402897c.

(12) Liu, K.; Li, B.; Li, Y.; Li, X.; Yang, F.; Zeng, G.; Peng, Y.; Zhang, Z.; Li, G.; Shi, Z.; Feng, S.; Song, D. An N-Rich Metal–Organic Framework with an Rht Topology: High CO2 and C2 Hydrocarbons Uptake and Selective Capture from CH4. *Chem. Commun.* **2014**, *50* (39), 5031. https://doi.org/10.1039/c4cc00375f.

(13) Cadiau, A.; Adil, K.; Bhatt, P. M.; Belmabkhout, Y.; Eddaoudi, M. A Metal-Organic Framework-Based Splitter for Separating Propylene from Propane. *Science* **2016**, *353* (6295), 137–140. https://doi.org/10.1126/science.aaf6323.

(14) Fu, Y.; Sun, D.; Qin, M.; Huang, R.; Li, Z. Cu(Ii)-and Co(Ii)-Containing Metal–Organic Frameworks (MOFs) as Catalysts for Cyclohexene Oxidation with Oxygen under Solvent-Free Conditions. *RSC Adv.* **2012**, *2* (8), 3309. https://doi.org/10.1039/c2ra01038k.

(15) Sun, Z.; Li, G.; Liu, H.; Liu, L. Salen-Co(II) Complex Incorporated into Amino-Functionalized MIL-101(Cr) through Postsynthetic Modification as a Cooperative Catalyst for Cyclohexane Selective Oxidation. *Applied Catalysis A: General* **2013**, *466*, 98–104. https://doi.org/10.1016/j.apcata.2013.06.032.

(16) Fei, H.; Shin, J.; Meng, Y. S.; Adelhardt, M.; Sutter, J.; Meyer, K.; Cohen, S. M. Reusable Oxidation Catalysis Using Metal-Monocatecholato Species in a Robust Metal–Organic Framework. *J. Am. Chem. Soc.* **2014**, *136* (13), 4965–4973. https://doi.org/10.1021/ja411627z.

(17) Liu, F.; Xu, Y.; Zhao, L.; Zhang, L.; Guo, W.; Wang, R.; Sun, D. Porous Barium–Organic Frameworks with Highly Efficient Catalytic Capacity and Fluorescence Sensing

Ability. *J. Mater. Chem. A* **2015**, *3* (43), 21545–21552. https://doi.org/10.1039/C5TA03680A.

(18) Cohen, S. M.; Zhang, Z.; Boissonnault, J. A. Toward "MetalloMOFzymes": Metal–Organic Frameworks with Single-Site Metal Catalysts for Small-Molecule Transformations. *Inorg. Chem.* **2016**, *55* (15), 7281–7290. https://doi.org/10.1021/acs.inorgchem.6b00828.

(19) Pascanu, V.; González Miera, G.; Inge, A. K.; Martín-Matute, B. Metal–Organic Frameworks as Catalysts for Organic Synthesis: A Critical Perspective. *J. Am. Chem. Soc.* **2019**, *141* (18), 7223–7234. https://doi.org/10.1021/jacs.9b00733.

(20) Jiang, Q.; Xiong, P.; Liu, J.; Xie, Z.; Wang, Q.; Yang, X.-Q.; Hu, E.; Cao, Y.; Sun, J.; Xu, Y.; Chen, L. A Redox-Active 2D Metal–Organic Framework for Efficient Lithium Storage with Extraordinary High Capacity. *Angewandte Chemie International Edition* **2020**, *59* (13), 5273–5277. https://doi.org/10.1002/anie.201914395.

(21) Férey, G.; Millange, F.; Morcrette, M.; Serre, C.; Doublet, M.-L.; Grenèche, J.-M.; Tarascon, J.-M. Mixed-Valence Li/Fe-Based Metal–Organic Frameworks with Both Reversible Redox and Sorption Properties. *Angewandte Chemie* **2007**, *119* (18), 3323–3327. https://doi.org/10.1002/ange.200605163.

(22) Kon, K.; Uchida, K.; Fuku, K.; Yamanaka, S.; Wu, B.; Yamazui, D.; Iguchi, H.; Kobayashi, H.; Gambe, Y.; Honma, I.; Takaishi, S. Electron-Conductive Metal–Organic Framework, Fe(Dhbq)(Dhbq = 2,5-Dihydroxy-1,4-Benzoquinone): Coexistence of Microporosity and Solid-State Redox Activity. *ACS Appl. Mater. Interfaces* **2021**, *13* (32), 38188–38193. https://doi.org/10.1021/acsami.1c06571.

(23) Ziebel, M. E.; Gaggioli, C. A.; Turkiewicz, A. B.; Ryu, W.; Gagliardi, L.; Long, J. R. Effects of Covalency on Anionic Redox Chemistry in Semiquinoid-Based Metal–Organic Frameworks. *J. Am. Chem. Soc.* **2020**, *142* (5), 2653–2664. https://doi.org/10.1021/jacs.9b13050.

(24) Zhao, H.; Chen, H.; Xu, C.; Li, Z.; Ding, B.; Dou, H.; Zhang, X. Charge Storage Mechanism of an Anthraquinone-Derived Porous Covalent Organic Framework with Multiredox Sites as Anode Material for Lithium-Ion Battery. *ACS Appl. Energy Mater.* **2021**, *4* (10), 11377–11385. https://doi.org/10.1021/acsaem.1c02200.

(25) Sheberla, D.; Bachman, J. C.; Elias, J. S.; Sun, C.-J.; Shao-Horn, Y.; Dincă, M. Conductive MOF Electrodes for Stable Supercapacitors with High Areal Capacitance. *Nature Mater* **2017**, *16* (2), 220–224. https://doi.org/10.1038/nmat4766.

(26) Clough, A. J.; Yoo, J. W.; Mecklenburg, M. H.; Marinescu, S. C. Two-Dimensional Metal–Organic Surfaces for Efficient Hydrogen Evolution from Water. *J. Am. Chem. Soc.* **2015**, *137* (1), 118–121. https://doi.org/10.1021/ja5116937.

(27) Miner, E. M.; Fukushima, T.; Sheberla, D.; Sun, L.; Surendranath, Y.; Dincă, M. Electrochemical Oxygen Reduction Catalysed by Ni3(Hexaiminotriphenylene)2. *Nat Commun* **2016**, *7* (1), 10942. https://doi.org/10.1038/ncomms10942.

(28) Dong, R.; Zheng, Z.; Tranca, D. C.; Zhang, J.; Chandrasekhar, N.; Liu, S.; Zhuang, X.; Seifert, G.; Feng, X. Immobilizing Molecular Metal Dithiolene–Diamine Complexes on 2D Metal–Organic Frameworks for Electrocatalytic H2 Production. *Chemistry – A European Journal* **2017**, *23* (10), 2255–2260. https://doi.org/10.1002/chem.201605337.

(29) Downes, C. A.; Clough, A. J.; Chen, K.; Yoo, J. W.; Marinescu, S. C. Evaluation of the H_2 Evolving Activity of Benzenehexathiolate Coordination Frameworks and the

Effect of Film Thickness on H $_2$ Production. *ACS Appl. Mater. Interfaces* **2018**, *10* (2), 1719–1727. https://doi.org/10.1021/acsami.7b15969.

(30) Ali, M.; Pervaiz, E.; Noor, T.; Rabi, O.; Zahra, R.; Yang, M. Recent Advancements in MOF-Based Catalysts for Applications in Electrochemical and Photoelectrochemical Water Splitting: A Review. *International Journal of Energy Research* **2021**, *45* (2), 1190–1226. https://doi.org/10.1002/er.5807.

(31) Kobayashi, Y.; Jacobs, B.; Allendorf, M. D.; Long, J. R. Conductivity, Doping, and Redox Chemistry of a Microporous Dithiolene-Based Metal−Organic Framework. *Chem. Mater.* **2010**, *22* (14), 4120–4122. https://doi.org/10.1021/cm101238m.

(32) Kambe, T.; Sakamoto, R.; Kusamoto, T.; Pal, T.; Fukui, N.; Hoshiko, K.; Shimojima, T.; Wang, Z.; Hirahara, T.; Ishizaka, K.; Hasegawa, S.; Liu, F.; Nishihara, H. Redox Control and High Conductivity of Nickel Bis(Dithiolene) Complex π-Nanosheet: A Potential Organic Two-Dimensional Topological Insulator. *J. Am. Chem. Soc.* **2014**, *136* (41), 14357–14360. https://doi.org/10.1021/ja507619d.

(33) Talin, A. A.; Centrone, A.; Ford, A. C.; Foster, M. E.; Stavila, V.; Haney, P.; Kinney, R. A.; Szalai, V.; El Gabaly, F.; Yoon, H. P.; Léonard, F.; Allendorf, M. D. Tunable Electrical Conductivity in Metal-Organic Framework Thin-Film Devices. *Science* **2014**, *343* (6166), 66–69. https://doi.org/10.1126/science.1246738.

(34) Hinckley, A. C.; Park, J.; Gomes, J.; Carlson, E.; Bao, Z. Air-Stability and Carrier Type in Conductive M $_3$ (Hexaaminobenzene) $_{2,}$ (M = Co, Ni, Cu). *J. Am. Chem. Soc.* **2020**, *142* (25), 11123–11130. https://doi.org/10.1021/jacs.0c03500.

(35) Mohammad-Pour, G. S.; Hatfield, K. O.; Fairchild, D. C.; Hernandez-Burgos, K.; Rodríguez-López, J.; Uribe-Romo, F. J. A Solid-Solution Approach for Redox Active

Metal–Organic Frameworks with Tunable Redox Conductivity. *J. Am. Chem. Soc.* **2019**, *141* (51), 19978–19982. https://doi.org/10.1021/jacs.9b10639.

(36) Su, J.; Yuan, S.; Wang, T.; Lollar, C. T.; Zuo, J.-L.; Zhang, J.; Zhou, H.-C. Zirconium Metal–Organic Frameworks Incorporating Tetrathiafulvalene Linkers: Robust and Redox-Active Matrices for *in Situ* Confinement of Metal Nanoparticles. *Chem. Sci.* **2020**, *11* (7), 1918–1925. https://doi.org/10.1039/C9SC06009J.

(37) Xie, L. S.; Skorupskii, G.; Dincă, M. Electrically Conductive Metal–Organic Frameworks. *Chem. Rev.* **2020**, *120* (16), 8536–8580. https://doi.org/10.1021/acs.chemrev.9b00766.

(38) Hao, Z.; Yang, G.; Song, X.; Zhu, M.; Meng, X.; Zhao, S.; Song, S.; Zhang, H. A Europium(III) Based Metal–Organic Framework: Bifunctional Properties Related to Sensing and Electronic Conductivity. *J. Mater. Chem. A* **2014**, *2* (1), 237–244. https://doi.org/10.1039/C3TA13179C.

(39) Hu, Y.-Q.; Li, M.-Q.; Wang, Y.; Zhang, T.; Liao, P.-Q.; Zheng, Z.; Chen, X.-M.; Zheng, Y.-Z. Direct Observation of Confined I−···I2···I− Interactions in a Metal–Organic Framework: Iodine Capture and Sensing. *Chemistry – A European Journal* **2017**, *23* (35), 8409–8413. https://doi.org/10.1002/chem.201702087.

(40) Li, G.-P.; Zhang, K.; Zhao, H.-Y.; Hou, L.; Wang, Y.-Y. Increased Electric Conductivity upon I2 Uptake and Gas Sorption in a Pillar-Layered Metal–Organic Framework. *ChemPlusChem* **2017**, *82* (5), 716–720. https://doi.org/10.1002/cplu.201700063.

(41) Zhang, X.; da Silva, I.; Fazzi, R.; Sheveleva, A. M.; Han, X.; Spencer, B. F.; Sapchenko, S. A.; Tuna, F.; McInnes, E. J. L.; Li, M.; Yang, S.; Schröder, M. Iodine

Adsorption in a Redox-Active Metal–Organic Framework: Electrical Conductivity Induced by Host−Guest Charge-Transfer. *Inorg. Chem.* **2019**, *58* (20), 14145–14150. https://doi.org/10.1021/acs.inorgchem.9b02176.

(42) Marshall, R. J.; Griffin, S. L.; Wilson, C.; Forgan, R. S. Single-Crystal to Single-Crystal Mechanical Contraction of Metal–Organic Frameworks through Stereoselective Postsynthetic Bromination. *J. Am. Chem. Soc.* **2015**, *137* (30), 9527–9530. https://doi.org/10.1021/jacs.5b05434.

(43) Takaishi, S.; Hosoda, M.; Kajiwara, T.; Miyasaka, H.; Yamashita, M.; Nakanishi, Y.; Kitagawa, Y.; Yamaguchi, K.; Kobayashi, A.; Kitagawa, H. Electroconductive Porous Coordination Polymer Cu[Cu(Pdt) $_2$] Composed of Donor and Acceptor Building Units. *Inorg. Chem.* **2009**, *48* (19), 9048–9050. https://doi.org/10.1021/ic802117q.

(44) Peng, Y.-L.; Pham, T.; Li, P.; Wang, T.; Chen, Y.; Chen, K.-J.; Forrest, K. A.; Space, B.; Cheng, P.; Zaworotko, M. J.; Zhang, Z. Robust Ultramicroporous Metal–Organic Frameworks with Benchmark Affinity for Acetylene. *Angewandte Chemie International Edition* **2018**, *57* (34), 10971–10975. https://doi.org/10.1002/anie.201806732.

(45) Takaishi, S.; Ishihara, N.; Kubo, K.; Katoh, K.; Breedlove, B. K.; Miyasaka, H.; Yamashita, M. Paramagnetic–Diamagnetic Phase Transition Accompanied by Coordination Bond Formation–Dissociation in the Dithiolate Complex Na[Ni(Pdt) $_2$]·2H $_2$ O. *Inorg. Chem.* **2011**, *50* (14), 6405–6407. https://doi.org/10.1021/ic2003172.

(46) Dei, A.; Gatteschi, D.; Pardi, L.; Russo, U. Tetraoxolene Radical Stabilization by the Interaction with Transition-Metal Ions. *Inorg. Chem.* **1991**, *30* (12), 2589–2594. https://doi.org/10.1021/ic00012a006.

(47) DeGayner, J. A.; Jeon, I.-R.; Sun, L.; Dincă, M.; Harris, T. D. 2D Conductive Iron-Quinoid Magnets Ordering up to T_c = 105 K via Heterogenous Redox Chemistry. *J. Am. Chem. Soc.* **2017**, *139* (11), 4175–4184. https://doi.org/10.1021/jacs.7b00705.

(48) Jeon, I.-R.; Negru, B.; Van Duyne, R. P.; Harris, T. D. A 2D Semiquinone Radical-Containing Microporous Magnet with Solvent-Induced Switching from T_c = 26 to 80 K. *J. Am. Chem. Soc.* **2015**, *137* (50), 15699–15702. https://doi.org/10.1021/jacs.5b10382.

(49) Ziebel, M. E.; Darago, L. E.; Long, J. R. Control of Electronic Structure and Conductivity in Two-Dimensional Metal–Semiquinoid Frameworks of Titanium, Vanadium, and Chromium. *J. Am. Chem. Soc.* **2018**, *140* (8), 3040–3051. https://doi.org/10.1021/jacs.7b13510.

(50) Murase, R.; Abrahams, B. F.; D'Alessandro, D. M.; Davies, C. G.; Hudson, T. A.; Jameson, G. N. L.; Moubaraki, B.; Murray, K. S.; Robson, R.; Sutton, A. L. Mixed Valency in a 3D Semiconducting Iron–Fluoranilate Coordination Polymer. *Inorg. Chem.* **2017**, *56* (15), 9025–9035. https://doi.org/10.1021/acs.inorgchem.7b01038.

(51) Kingsbury, C. J.; Abrahams, B. F.; D'Alessandro, D. M.; Hudson, T. A.; Murase, R.; Robson, R.; White, K. F. Role of NEt_4^+ in Orienting and Locking Together $[M_2Lig_3]^{2-}$ (6,3) Sheets (H_2Lig = Chloranilic or Fluoranilic Acid) to Generate Spacious Channels Perpendicular to the Sheets. *Crystal Growth & Design* **2017**, *17* (4), 1465–1470. https://doi.org/10.1021/acs.cgd.6b01886.

(52) Abrahams, B. F.; Hudson, T. A.; McCormick, L. J.; Robson, R. Coordination Polymers of 2,5-Dihydroxybenzoquinone and Chloranilic Acid with the (10,3)- *a* Topology. *Crystal Growth & Design* **2011**, *11* (7), 2717–2720. https://doi.org/10.1021/cg2005908.

(53) Nath, A.; Asha, K. S.; Mandal, S. Conductive Metal-Organic Frameworks: Electronic Structure and Electrochemical Applications. *Chemistry – A European Journal* **2021**, *27* (45), 11482–11538. https://doi.org/10.1002/chem.202100610.

(54) *A review on metal-organic frameworks: Synthesis and applications | Elsevier Enhanced Reader*. https://reader.elsevier.com/reader/sd/pii/S0165993619301840?token=77E98D30F7C5147C3294A1125AFFD32D7D875C4A67E2B557EFC80ECDBC58595F0D3C4DF462C7FF2CD33D32853D276C1F&originRegion=us-east-1&originCreation=20220615033158 (accessed 2022-06-15). https://doi.org/10.1016/j.trac.2019.06.007.

(55) Li, C.; Zhang, L.; Chen, J.; Li, X.; Sun, J.; Zhu, J.; Wang, X.; Fu, Y. Recent Development and Applications of Electrical Conductive MOFs. *Nanoscale* **2021**, *13* (2), 485–509. https://doi.org/10.1039/D0NR06396G.

(56) Sun, L.; Miyakai, T.; Seki, S.; Dincă, M. Mn_2 (2,5-Disulfhydrylbenzene-1,4-Dicarboxylate): A Microporous Metal–Organic Framework with Infinite $(-Mn-S-)_\infty$ Chains and High Intrinsic Charge Mobility. *J. Am. Chem. Soc.* **2013**, *135* (22), 8185–8188. https://doi.org/10.1021/ja4037516.

(57) Sun, L.; Hendon, C. H.; Minier, M. A.; Walsh, A.; Dincă, M. Million-Fold Electrical Conductivity Enhancement in Fe_2 (DEBDC) versus Mn_2 (DEBDC) (E = S, O). *J. Am. Chem. Soc.* **2015**, *137* (19), 6164–6167. https://doi.org/10.1021/jacs.5b02897.

(58) Sun, L.; Hendon, C. H.; Park, S. S.; Tulchinsky, Y.; Wan, R.; Wang, F.; Walsh, A.; Dincă, M. Is Iron Unique in Promoting Electrical Conductivity in MOFs? *Chem. Sci.* **2017**, *8* (6), 4450–4457. https://doi.org/10.1039/C7SC00647K.

(59) Park, J. G.; Aubrey, M. L.; Oktawiec, J.; Chakarawet, K.; Darago, L. E.; Grandjean, F.; Long, G. J.; Long, J. R. Charge Delocalization and Bulk Electronic Conductivity in the Mixed-Valence Metal–Organic Framework Fe(1,2,3-Triazolate) $_2$ (BF $_4$) $_x$. *J. Am. Chem. Soc.* **2018**, *140* (27), 8526–8534. https://doi.org/10.1021/jacs.8b03696.

(60) Gándara, F.; Uribe-Romo, F. J.; Britt, D. K.; Furukawa, H.; Lei, L.; Cheng, R.; Duan, X.; O'Keeffe, M.; Yaghi, O. M. Porous, Conductive Metal-Triazolates and Their Structural Elucidation by the Charge-Flipping Method. *Chemistry – A European Journal* **2012**, *18* (34), 10595–10601. https://doi.org/10.1002/chem.201103433.

(61) Campbell, M. G.; Sheberla, D.; Liu, S. F.; Swager, T. M.; Dincă, M. Cu3(Hexaiminotriphenylene)2: An Electrically Conductive 2D Metal–Organic Framework for Chemiresistive Sensing. *Angewandte Chemie International Edition* **2015**, *54* (14), 4349–4352. https://doi.org/10.1002/anie.201411854.

(62) Sheberla, D.; Sun, L.; Blood-Forsythe, M. A.; Er, S.; Wade, C. R.; Brozek, C. K.; Aspuru-Guzik, A.; Dincă, M. High Electrical Conductivity in Ni $_3$ (2,3,6,7,10,11-Hexaiminotriphenylene) $_2$, a Semiconducting Metal–Organic Graphene Analogue. *J. Am. Chem. Soc.* **2014**, *136* (25), 8859–8862. https://doi.org/10.1021/ja502765n.

(63) Shinde, S. S.; Lee, C. H.; Jung, J.-Y.; Wagh, N. K.; Kim, S.-H.; Kim, D.-H.; Lin, C.; Lee, S. U.; Lee, J.-H. Unveiling Dual-Linkage 3D Hexaiminobenzene Metal–Organic Frameworks towards Long-Lasting Advanced Reversible Zn–Air Batteries. *Energy Environ. Sci.* **2019**, *12* (2), 727–738. https://doi.org/10.1039/C8EE02679C.

(64) Zhang, X.; Wang, Z.-X.; Xie, H.; Li, M.-X.; Woods, T. J.; Dunbar, K. R. A Cobalt(II) Spin-Crossover Compound with Partially Charged TCNQ Radicals and an

Anomalous Conducting Behavior. *Chem. Sci.* **2016**, *7* (2), 1569–1574. https://doi.org/10.1039/C5SC03547C.

(65) Heintz, R. A.; Zhao, H.; Ouyang, X.; Grandinetti, G.; Cowen, J.; Dunbar, K. R. New Insight into the Nature of Cu(TCNQ): Solution Routes to Two Distinct Polymorphs and Their Relationship to Crystalline Films That Display Bistable Switching Behavior. *Inorg. Chem.* **1999**, *38* (1), 144–156. https://doi.org/10.1021/ic9812095.

(66) Avendano, C.; Zhang, Z.; Ota, A.; Zhao, H.; Dunbar, K. R. Dramatically Different Conductivity Properties of Metal–Organic Framework Polymorphs of Tl(TCNQ): An Unexpected Room-Temperature Crystal-to-Crystal Phase Transition. *Angewandte Chemie International Edition* **2011**, *50* (29), 6543–6547. https://doi.org/10.1002/anie.201100372.

(67) Park, S. S.; Hontz, E. R.; Sun, L.; Hendon, C. H.; Walsh, A.; Van Voorhis, T.; Dincă, M. Cation-Dependent Intrinsic Electrical Conductivity in Isostructural Tetrathiafulvalene-Based Microporous Metal–Organic Frameworks. *J. Am. Chem. Soc.* **2015**, *137* (5), 1774–1777. https://doi.org/10.1021/ja512437u.

(68) Xie, L. S.; Alexandrov, E. V.; Skorupskii, G.; Proserpio, D. M.; Dincă, M. Diverse π–π Stacking Motifs Modulate Electrical Conductivity in Tetrathiafulvalene-Based Metal–Organic Frameworks. *Chem. Sci.* **2019**, *10* (37), 8558–8565. https://doi.org/10.1039/C9SC03348C.

(69) Castells-Gil, J.; Mañas-Valero, S.; Vitórica-Yrezábal, I. J.; Ananias, D.; Rocha, J.; Santiago, R.; Bromley, S. T.; Baldoví, J. J.; Coronado, E.; Souto, M.; Mínguez Espallargas, G. Electronic, Structural and Functional Versatility in Tetrathiafulvalene-Lanthanide

Metal–Organic Frameworks. *Chemistry – A European Journal* **2019**, *25* (54), 12636–12643. https://doi.org/10.1002/chem.201902855.

(70) Haider, G.; Usman, M.; Chen, T.-P.; Perumal, P.; Lu, K.-L.; Chen, Y.-F. Electrically Driven White Light Emission from Intrinsic Metal–Organic Framework. *ACS Nano* **2016**, *10* (9), 8366–8375. https://doi.org/10.1021/acsnano.6b03030.

(71) Qu, L.; Iguchi, H.; Takaishi, S.; Habib, F.; Leong, C. F.; D'Alessandro, D. M.; Yoshida, T.; Abe, H.; Nishibori, E.; Yamashita, M. Porous Molecular Conductor: Electrochemical Fabrication of Through-Space Conduction Pathways among Linear Coordination Polymers. *J. Am. Chem. Soc.* **2019**, *141* (17), 6802–6806. https://doi.org/10.1021/jacs.9b01717.

(72) Kuang, X.; Chen, S.; Meng, L.; Chen, J.; Wu, X.; Zhang, G.; Zhong, G.; Hu, T.; Li, Y.; Lu, C.-Z. Supramolecular Aggregation of a Redox-Active Copper-Naphthalenediimide Network with Intrinsic Electron Conduction. *Chem. Commun.* **2019**, *55* (11), 1643–1646. https://doi.org/10.1039/C8CC10269D.

(73) Aubrey, M. L.; Kapelewski, M. T.; Melville, J. F.; Oktawiec, J.; Presti, D.; Gagliardi, L.; Long, J. R. Chemiresistive Detection of Gaseous Hydrocarbons and Interrogation of Charge Transport in Cu[Ni(2,3-Pyrazinedithiolate)$_2$] by Gas Adsorption. *J. Am. Chem. Soc.* **2019**, *141* (12), 5005–5013. https://doi.org/10.1021/jacs.9b00654.

(74) Bhattacharya, B.; Layek, A.; Mehboob Alam, Md.; Maity, D. K.; Chakrabarti, S.; Ray, P. P.; Ghoshal, D. Cd(Ii) Based Metal–Organic Framework Behaving as a Schottky Barrier Diode. *Chem. Commun.* **2014**, *50* (58), 7858. https://doi.org/10.1039/c4cc00827h.

(75) Dolgopolova, E. A.; Galitskiy, V. A.; Martin, C. R.; Gregory, H. N.; Yarbrough, B. J.; Rice, A. M.; Berseneva, A. A.; Ejegbavwo, O. A.; Stephenson, K. S.;

Kittikhunnatham, P.; Karakalos, S. G.; Smith, M. D.; Greytak, A. B.; Garashchuk, S.; Shustova, N. B. Connecting Wires: Photoinduced Electronic Structure Modulation in Metal–Organic Frameworks. *J. Am. Chem. Soc.* **2019**, 9.

(76) Park, S. S.; Hontz, E. R.; Sun, L.; Hendon, C. H.; Walsh, A.; Van Voorhis, T.; Dincă, M. Cation-Dependent Intrinsic Electrical Conductivity in Isostructural Tetrathiafulvalene-Based Microporous Metal–Organic Frameworks. *J. Am. Chem. Soc.* **2015**, *137* (5), 1774–1777. https://doi.org/10.1021/ja512437u.

(77) Narayan, T. C.; Miyakai, T.; Seki, S.; Dincă, M. High Charge Mobility in a Tetrathiafulvalene-Based Microporous Metal–Organic Framework. *J. Am. Chem. Soc.* **2012**, *134* (31), 12932–12935. https://doi.org/10.1021/ja3059827.

(78) Pointillart, F.; le Guennic, B.; Cador, O.; Maury, O.; Ouahab, L. Lanthanide Ion and Tetrathiafulvalene-Based Ligand as a "Magic" Couple toward Luminescence, Single Molecule Magnets, and Magnetostructural Correlations. *Acc. Chem. Res.* **2015**, *48* (11), 2834–2842. https://doi.org/10.1021/acs.accounts.5b00296.

(79) Wang, H.-Y.; Ge, J.-Y.; Hua, C.; Jiao, C.-Q.; Wu, Y.; Leong, C. F.; D'Alessandro, D. M.; Liu, T.; Zuo, J.-L. Photo- and Electronically Switchable Spin-Crossover Iron(II) Metal–Organic Frameworks Based on a Tetrathiafulvalene Ligand. *Angewandte Chemie International Edition* **2017**, *56* (20), 5465–5470. https://doi.org/10.1002/anie.201611824.

(80) Usov, P. M.; Fabian, C.; D'Alessandro, D. M. Rapid Determination of the Optical and Redox Properties of a Metal–Organic Framework via in Situ Solid State Spectroelectrochemistry. *Chem. Commun.* **2012**, *48* (33), 3945. https://doi.org/10.1039/c2cc30568b.

(81) Zhang, Z.; Yoshikawa, H.; Awaga, K. Monitoring the Solid-State Electrochemistry of Cu(2,7-AQDC) (AQDC = Anthraquinone Dicarboxylate) in a Lithium Battery: Coexistence of Metal and Ligand Redox Activities in a Metal–Organic Framework. *J. Am. Chem. Soc.* **2014**, *136* (46), 16112–16115. https://doi.org/10.1021/ja508197w.

(82) Talin, A. A.; Centrone, A.; Ford, A. C.; Foster, M. E.; Stavila, V.; Haney, P.; Kinney, R. A.; Szalai, V.; El Gabaly, F.; Yoon, H. P.; Léonard, F.; Allendorf, M. D. Tunable Electrical Conductivity in Metal-Organic Framework Thin-Film Devices. *Science* **2014**, *343* (6166), 66–69. https://doi.org/10.1126/science.1246738.

(83) Yamashita, O. Effect of Metal Electrode on Seebeck Coefficient of *p* - and *n* -Type Si Thermoelectrics. *Journal of Applied Physics* **2004**, *95* (1), 178–183. https://doi.org/10.1063/1.1630361.

(84) Sootsman, J. R.; Chung, D. Y.; Kanatzidis, M. G. New and Old Concepts in Thermoelectric Materials. *Angewandte Chemie International Edition* **2009**, *48* (46), 8616–8639. https://doi.org/10.1002/anie.200900598.

(85) Imai, H.; Shimakawa, Y.; Kubo, Y. Large Thermoelectric Power Factor in TiS2 Crystal with Nearly Stoichiometric Composition. *Phys. Rev. B* **2001**, *64* (24), 241104. https://doi.org/10.1103/PhysRevB.64.241104.

(86) Jonson, M.; Mahan, G. D. Mott's Formula for the Thermopower and the Wiedemann-Franz Law. *Phys. Rev. B* **1980**, *21* (10), 4223–4229. https://doi.org/10.1103/PhysRevB.21.4223.

(87) Yoon, S.; Talin, A. A.; Stavila, V.; Mroz, A. M.; Bennett, T. D.; He, Y.; Keen, D. A.; Hendon, C. H.; Allendorf, M. D.; So, M. C. From N- to p-Type Material: Effect of

Metal Ion on Charge Transport in Metal–Organic Materials. *ACS Appl. Mater. Interfaces* **2021**, acsami.1c09130. https://doi.org/10.1021/acsami.1c09130.

Chapter 2.

Effect of halogen doping on electrical conductivity and Seebeck coefficient of metal-organic framework $Cu^{II}[Cu^{II}(pdt)_2]$(pdt = 2,3-pyrazinedithiol)

2.1 Chapter introduction

MOFs come under a new category of porous materials because of their outstanding properties for a wide range of applications, such as gas storage,[1–6] gas separation,[7–12] sensing and catalysis,[13–18] etc. In recent years, electrically conductive MOFs have been explored extensively due to their potential applications in the field of electronics as active materials for energy storage,[19–24] electrocatalysis,[25–29] and chemiresistive sensing.[30–33] There are many strategies that have been introduced in order to synthesize conductive MOFs. They are roughly classified into four categories: through-bond, through-space, extended conjugation, and guest-promoted strategies.[34] The first three strategies are mainly focused on the formation of the conductive pathway, in other words, the formation of overlap of the frontier orbitals by using π-π stacking or extended π-conjugation. In these compounds, conductive carriers are doped during crystallization by utilizing charge-transfer (CT) interactions or a mixed-valence strategy. Whereas guest-promoted strategies are focused on band-filling control or carrier doping by using post-synthetic encapsulation of guests. Such a post-synthetic modification is a unique characteristic of porous materials. There are hundreds of electrically conductive MOFs that have been reported, most of them have been synthesized by using the three strategies mentioned earlier. As for the post-synthetic doped strategy, iodine[34–38] or polyiodide[40,41] have been used to enhance the electrical conductivities of MOFs. Kobayashi *et al*. have reported $Cu[Ni(pdt)_2]$ (pdt = 2,3-pyrazinedithiolate) and realised the enhancement of electrical conductivity by a factor 10^4 upon doping with I_2 vapor.[35] Although the effects of halogen doping on the electrical conductivities of MOFs have been demonstrated, But detailed study on stoichiometric

halogen doping on structural changes, optical properties, conductive carriers and thermoelectromotive measurements has scarcely been performed.

2.2 Research objective

Guest-induced modification of the electronic states in metal-organic frameworks (MOFs) has brought about a new field of interdisciplinary research which includes host-guest chemistry and solid-state physics. Although there have been plenty of studies on guest-promoted enhancement of electrical conductivity. However, properties like structure-property relationships, stoichiometry and conductive carriers have not been studied in detail. So, we studied the effect of continuous and controlled halogen doping on structural, optical, thermoelectric and semiconducting properties of $Cu[Cu(pdt)_2]$ (pdt = 2,3-pyrazinedithiolate) as a function of halogen stoichiometry. $Cu[Cu(pdt)_2]$ is a prototype of electron conductive MOFs[42] and have permanent porosity (a BET surface area of 280 $m^2\ g^{-1}$).[43] Taking advantage of porosity halogen doping was performed. We doped $Cu[Cu(pdt)_2]$ (Figure 1, pdt = 2,3-pyrazinedithiolate) with Br_2/I_2 vapor by keeping the amount of MOF constant and varying halogen concentration. After doping, annealing of the samples was performed at 60 ^oC for 24hr. Then the samples were used for the structural, optical, semiconductive and thermoelectric properties measurements.

2.3 Synthesis

Synthesis of $Na[Cu(pdt)_2]\cdot 2H_2O$. 2,3-Pyrazinedithiol (H_2pdt) was prepared following a procedure reported earlier.[35] $Na[Cu(pdt)_2]\cdot 2H_2O$ was synthesized as mentioned in scheme 1. In a 1000 ml conical flask, NaOH (0.8 g, 20 mmol) was dissolved in 300 ml of deionized water. H_2pdt (1.44 g, 10 mmol) was added to the NaOH solution. The solution was stirred until the color became pale yellow. After that $Cu(ClO_4)_2\cdot 6H_2O$ (1.84 g, 5 mmol) was added to the flask, followed by 300 ml methanol, while stirring. After which the color of the solution turned dark red. After that NaBr (2 g) was added to the reaction mixture, followed by H_2O_2 (0.6 ml, 30%). Upon adding H_2O_2 , dark green precipitate starts forming. The solid was collected by filtration and washed with H_2O. Compound was characterized with the help of PXRD pattern and CHN analysis.

Synthesis of $Cu[Cu(pdt)_2]$. $Cu[Cu(pdt)_2]$ was synthesized using a procedure reported by our group.[35] Procedure is shown in scheme 2.3 . In a 1000 ml conical flask, $Na[Cu(pdt)_2]\cdot 2H_2O$ (1.0 g, 2.5 mmol) was dissolved in 500 ml of CH_3CN, and the solution was filtered to remove the undissolved impurities. CuI (0.45 g, 2.3 mmol) in 100 ml CH_3CN was added dropwise to the filtrate, while stirring. After stirring for 30 minutes at room temperature, black polycrystalline solid was obtained and was collected by using a membrane filter. The product was dried under vacuum overnight before characterization. Final product characterization was performed with the help of PXRD pattern and CHN analysis.

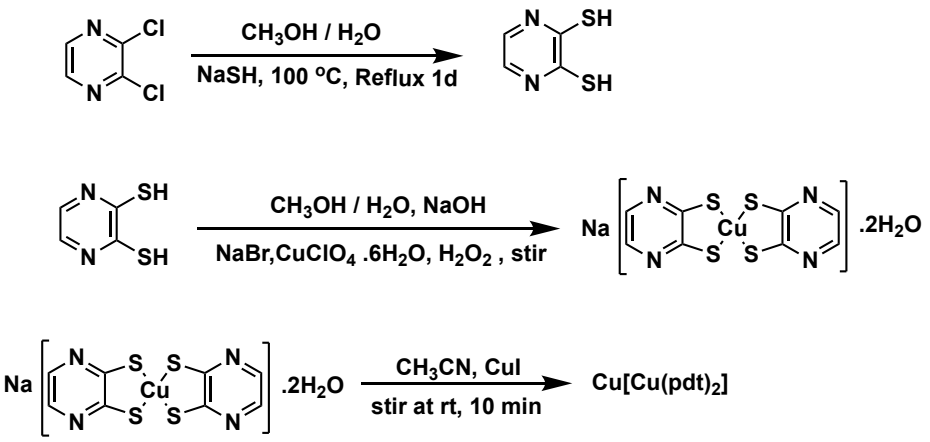

Scheme 2.3 Reactions involve in the synthesis of Cu[Cu(pdt_2)] MOF.

2.4 Characterization of Cu[Cu(pdt_2)]

2.4.1 Crystal description

Crystal structure of Cu[Cu(pdt_2)] was reported our group.[35] It crystalizes in a tetragonal lattice with space $P4_2/mmc$ group. Crystal description show that there are two crystallographically different Copper centers were present in formal oxidation state of +II. One is surrounded by the four S atom from two pyrazine ligands in a square planar manner forming a 2D sheet (**Figure 2.4 b**). On the other hand, another Cu center is coordinated with four N atom from four pyrazine ligand and bridging Cu-bisdithiolate unit leading to a 1-D pore channel along *c* axis with a pore size of diameter 3.4 Å (**Figure 2.4 c**). We utilize the permanent porosity of the MOF and dopped with bromine vapor.

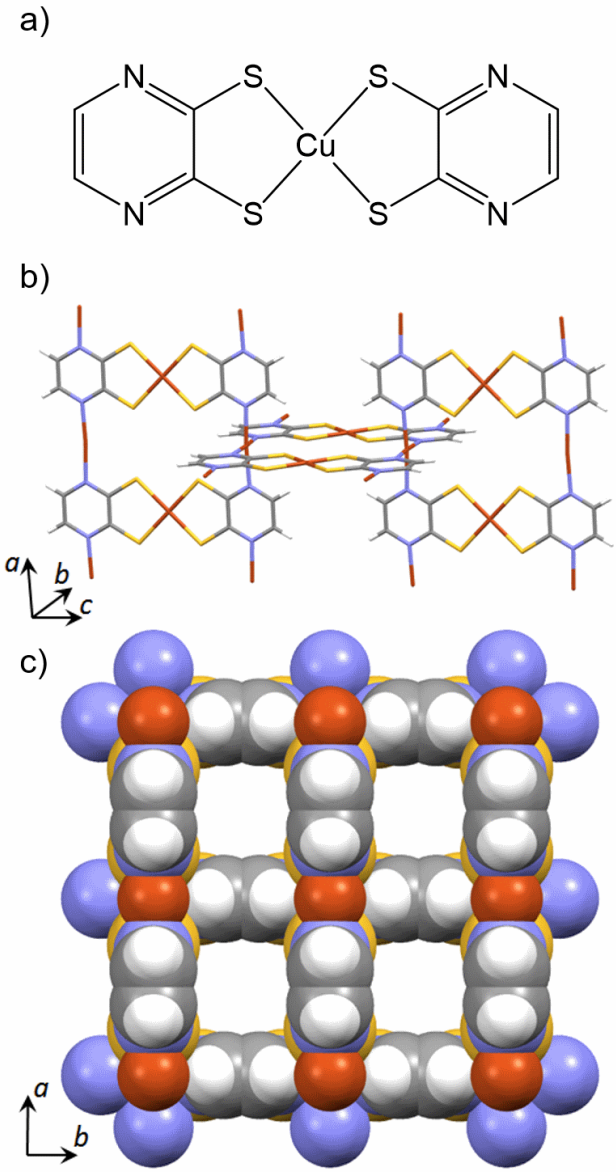

Figure 2.4.1 (a) Molecular structure of $Cu(pdt)_2$. Crystal structure of $Cu[Cu(pdt)_2]$ with **(b)** stick model and **(c)** space filling model. Brown: Cu, Blue: N, Gray: C, Yellow: S

2.4.2 PXRD pattern

Phase purity of the bulk sample was investigated using PXRD pattern as shown is **Figure 2.4.2**

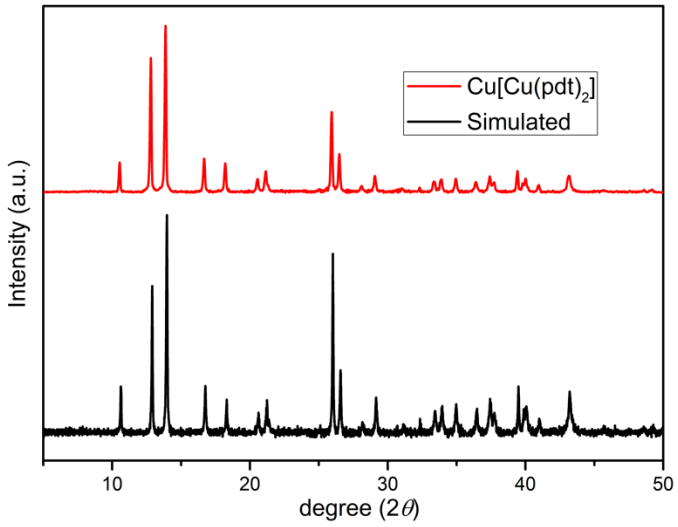

Figure 2.4.2 PXRD pattern of $Cu[Cu(pdt)_2]$. Red line (as synthesized) and black line (simulated).

2.5 Bromine doping

As we noted above, $Cu[Cu(pdt)_2]$ has 1D pores with a relatively small pore diameter of 4Å. Taking the advantage of porosity Br_2 doping was performed using 100 mg of $Cu[Cu(pdt)_2]$ at a time and a different volume of Br_2 vapor. Detailed experimental setup for Br_2 doping is described in **Figure 2.5**. Bromine vapor doping was performed using the following procedure. Polycrystalline $Cu[Cu(pdt)_2]$ (100 mg) was placed into a double necked round bottom flask. One neck was connected to a vacuum line, and the other neck was sealed with a rubber septum. The atmosphere in the flask was replaced with N_2 by

using a pump-purge process three times. Then different volumes of bromine vapor (not liquid) were withdrawn from the bottle with a syringe and injected into the flask. The schematic drawing of the experimental apparatus is shown in **Figure 2.5**. After doping with bromine vapor, all samples were transferred to screw vials and annealed for 24 h at 60 °C.

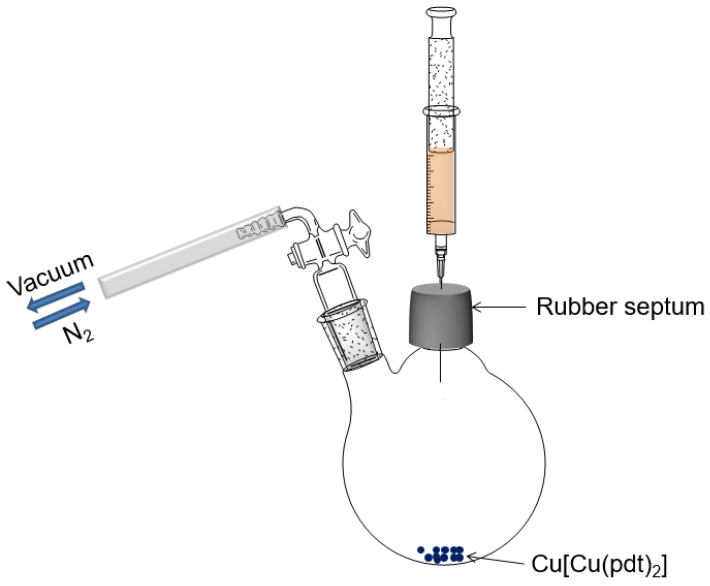

Figure 2.5 Apparatus for the bromine doping into Cu[Cu(pdt)$_2$].

We incorporated different volumes of Br_2 vapor while keeping the amount of MOF constant to afford Br_x@Cu[Cu(pdt)$_2$] ($0 \leq x \leq 1.03$). it was realized that even if we used an excess amount of Br_2 vapor, the Br fraction (x) of Br_x@Cu[Cu(pdt)$_2$] was approximately 1, indicating that $x \approx 1$ is the upper limit of the Br loading. This finding

indicates that Br atoms is not merely physiosorbed but electronically interact with $Cu[Cu(pdt)_2]$.

2.6 Structural investigation of Br_x@$Cu[Cu(pdt)_2]$

Structural analyses were performed using powder X-ray diffraction (PXRD) on a Rigaku Smart Lab diffractometer (plate stage) with Cu Kα radiation source (λ = 1.5456 Å, 40 kW/40 mA, 2θ = 5°−50°, and a speed of 1°/min). PXRD data was further fitted using Le Bail refinement with the rietica software.

X-ray diffraction patterns of Br_x@$Cu[Cu(pdt)_2]$ were plotted with respect to 2θ in **Figure 2.6.1 a**. It reveals that PXRD patterns of Br_x@$Cu[Cu(pdt)_2]$ are isomorphic with pristine $Cu[Cu(pdt)_2]$, and the crystallinities of the doped samples were retained, which further confirms that the Br doping does not change the intrinsic skeleton of the MOFs. However, with the inclusion of bromine, the intensity of the peak for the (100) face of Br_x@$Cu[Cu(pdt)_2]$ continuously decreased with an increase in x. This corresponds to the successive incorporation of bromine molecules into the pores of $Cu[Cu(pdt)_2]$.

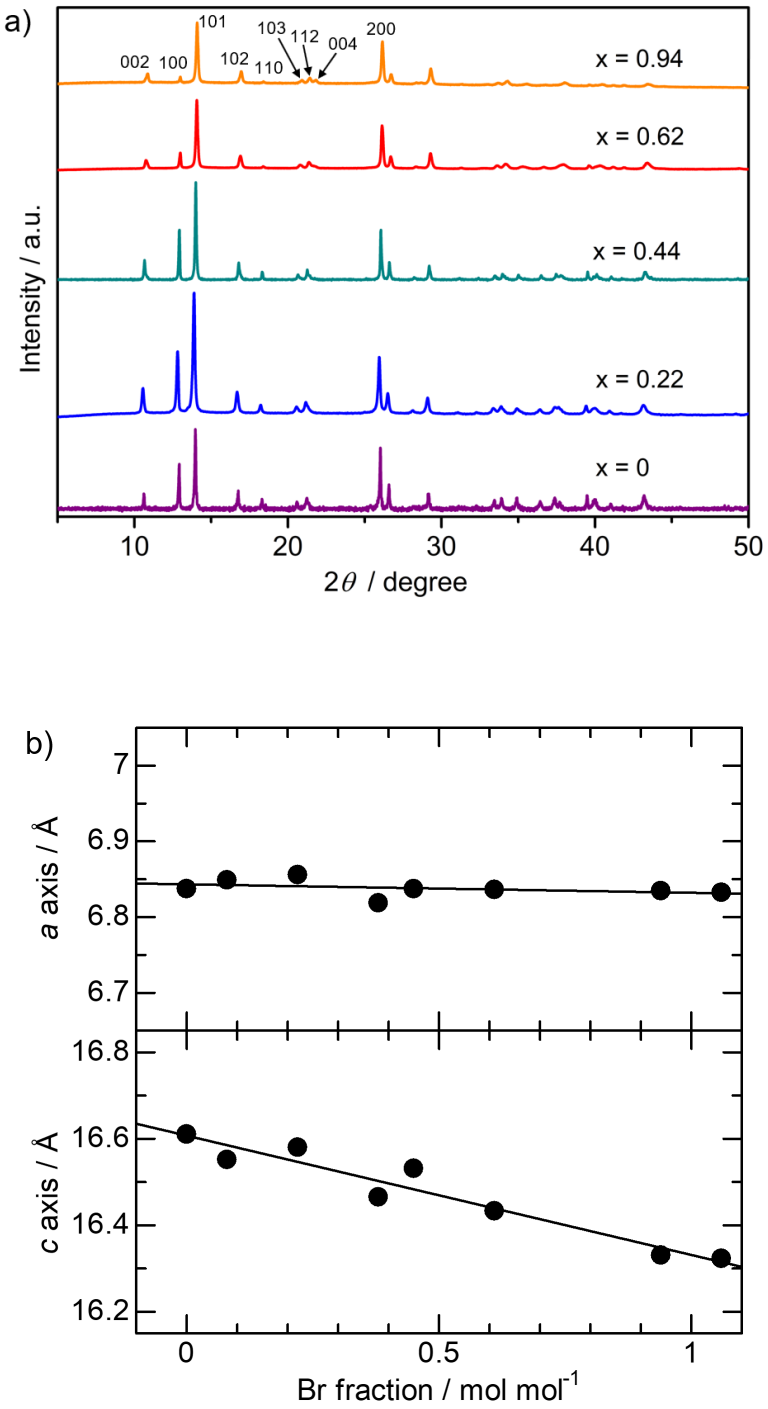

Figure 2.6.1 (a) PXRD patterns of Br_x@Cu[Cu(pdt)$_2$]. **(b)** Lattice parameters of Br_x@Cu[Cu(pdt)$_2$] as a function of the Br fraction/mol.

The PXRD patterns of Br_x@Cu[Cu(pdt)$_2$] were fitted using the Le Bail method to estimate the unit cell parameters (**Figure 2.6.1 b**). It reveals that all of the doped samples retained tetragonal lattice as shown in **Table 1**. Although the lattice parameter *a*-axis has barely changed but the *c*-axis significantly changed and it continuously shortened with an increase in *x*.

2.6.2 Le Bail Plot

a) x = 0

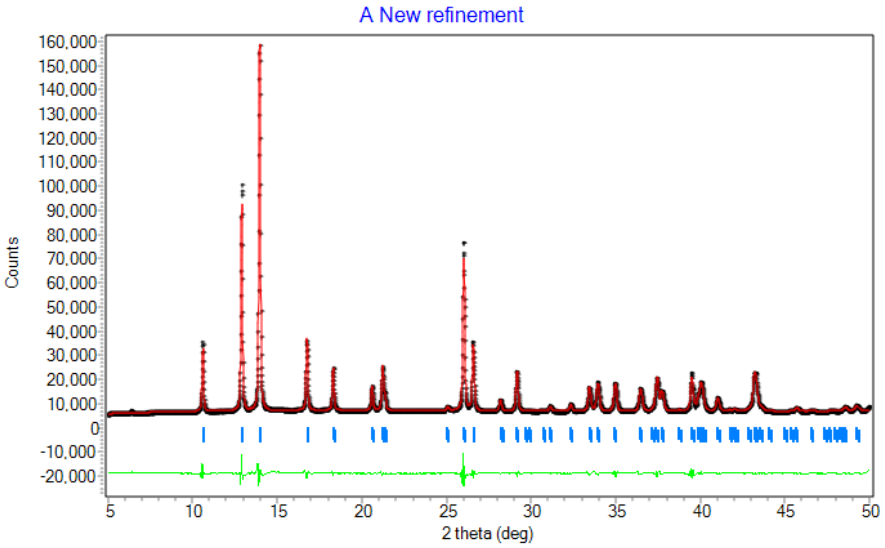

b) x = 0.08

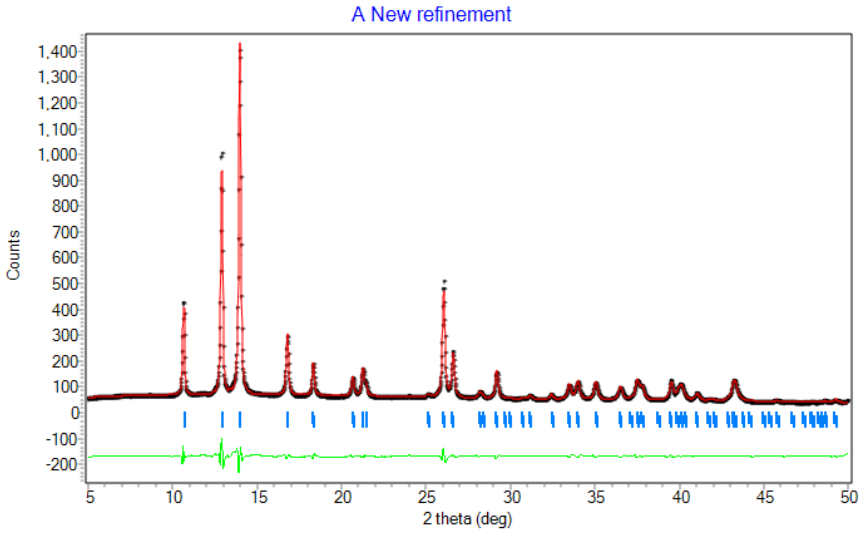

c) x = 0.22

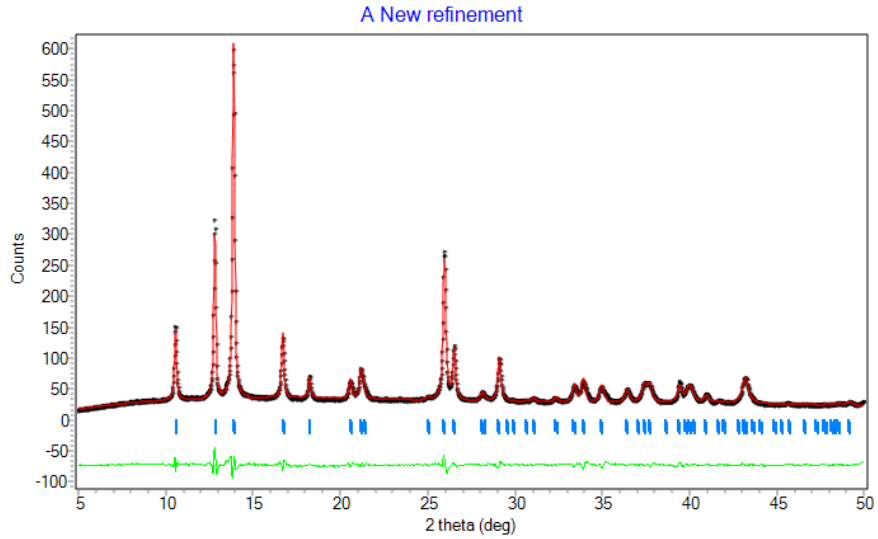
A New refinement
Counts
2 theta (deg)

d) x = 0.44

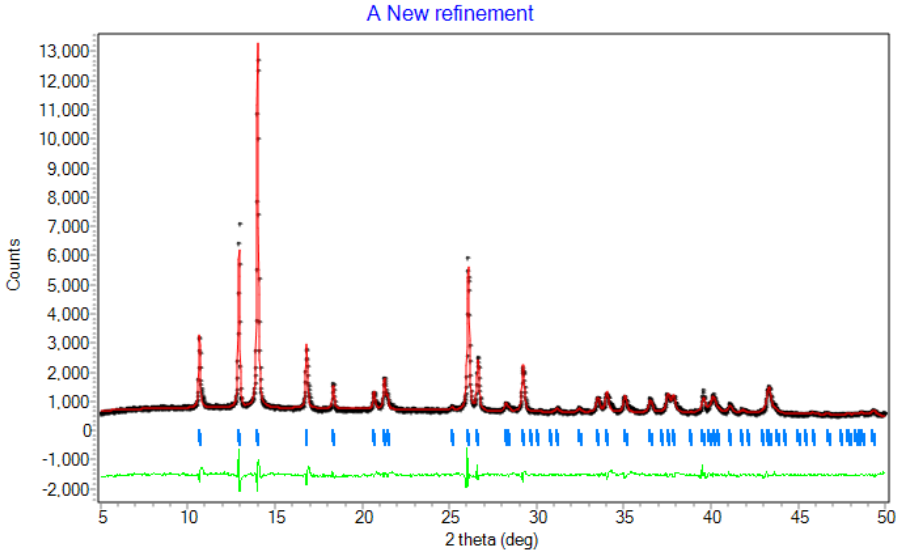
A New refinement
Counts
2 theta (deg)

e) x = 0.62

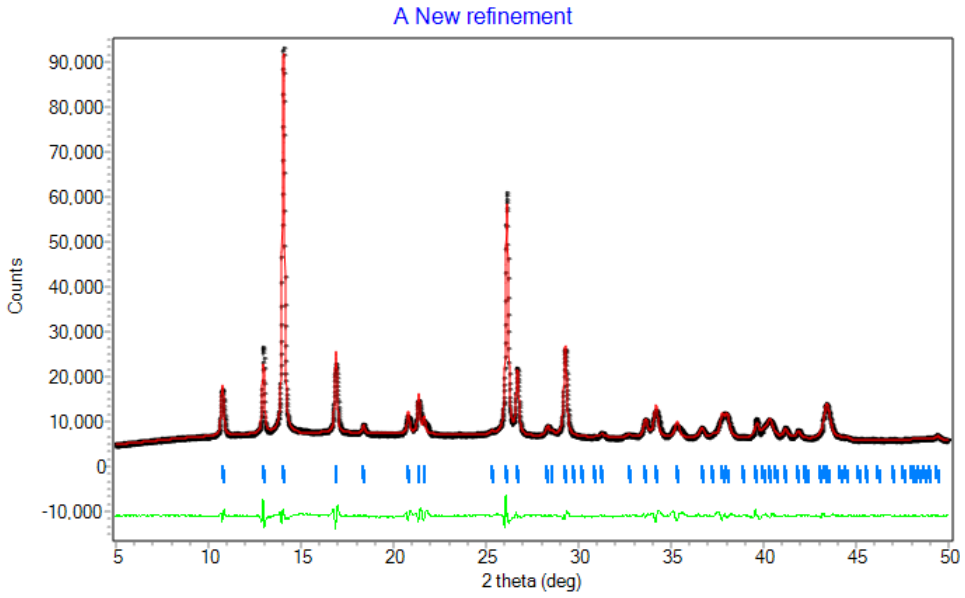

f) x = 0.94

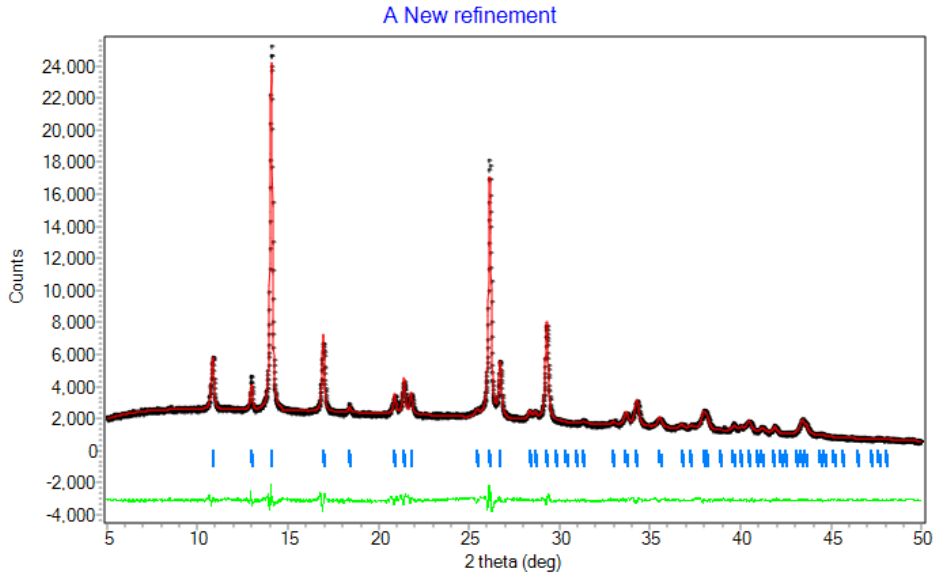

Figure 2.6.2 Le Bail fitting of PXRD patterns of **a)** $Cu[Cu(pdt)_2]$, **b)** $Br_{0.08}@Cu[Cu(pdt)_2]$, **c)** $Br_{0.22}@Cu[Cu(pdt)_2]$, **d)** $Br_{0.44}@Cu[Cu(pdt)_2]$, **e)** $Br_{0.62}@Cu[Cu(pdt)_2]$, and **f)** $Br_{0.94}@Cu[Cu(pdt)_2]$,. Red and green lines represent fitted and differential patterns.

Table 1 Unit cell parameters for Br_x@ $Cu[Cu(pdt)_2]$

Sample	Space Group	Lattice parameters		Rp(%)	wRp(%)	$\chi 2$
		a (Å)	*c* (Å)			
$Cu[Cu(pdt)_2]$	$P4_2/mmc$	6.8372(1)	16.6100(2)	2.252	3.402	10.74
$Br_{0.08}$@$Cu[Cu(pdt)_2]$	$P4_2/mmc$	6.8487(2)	16.5510(8)	2.934	4.109	0.137
$Br_{0.22}$@$Cu[Cu(pdt)_2]$	$P4_2/mmc$	6.8556(3)	16.5790(12)	3.513	4.608	0.089
$Br_{0.38}$@$Cu[Cu(pdt)_2]$	$P4_2/mmc$	6.8184(3)	16.4650(13)	3.223	4.385	0.076
$Br_{0.44}$@$Cu[Cu(pdt)_2]$	$P4_2/mmc$	6.8371(7)	16.5310(18)	4.365	5.990	3.102
$Br_{0.62}$@$Cu[Cu(pdt)_2]$	$P4_2/mmc$	6.8361(5)	16.4330(13)	2.791	4.003	13.188
$Br_{0.94}$@$Cu[Cu(pdt)_2]$	$P4_2/mmc$	6.8322(2)	16.3230(7)	2.186	2.904	6.740

Table 2. Elemental analysis data for Br_x@$Cu[Cu(pdt)_2]$

Sample	Found		Calcd. for $Br_xCu[Cu(pdt)_2]n(CH_3CN)$		
x	Br(%)	S(%)	n	Br(%)	S(%)
0.08	1.43	27.70	1.0	1.39	27.95
0.22	3.71	27.17	1.0	3.74	27.28
0.44	7.06	25.06	1.5	6.92	25.24
0.62	9.92	25.93	0.9	9.95	25.76
0.94	14.39	24.99	0.7	14.57	24.89

*The following equation was used to evaluate *x*.

$$x = \left(\frac{\mathrm{Br}(\%)}{79.904}\right) \div \left(\frac{\mathrm{S}(\%)}{4 \times 32.065}\right)$$

Shrinkage of *c*-axis could be better understood with the help of bond distance analysis. We have examined two $[Cu(pdt)_2]^{1/2}$ unit as shown in **Figure 2.6.3**. One $[Cu^{II}(pdt)_2]^{+II}$ has Cu in +II oxidation state on the other hand another one has $[Cu^{III}(pdt)_2]^{+I}$ Cu in +III

oxidation state. We have shown the bond distance details of the two. The one with Cu^{II} shows a Cu-S bond distance of 2.264 Å and Cu^{III} shows a bond distance of 2.183 Å. Which indicates that as Cu^{II} oxidizes to Cu^{III}, Cu-S bond has shorten as a result S-S bond also get shorten by 0.16 Å. And these results indicates that bromine molecules might have oxidizes Cu^{II} to Cu^{III}.

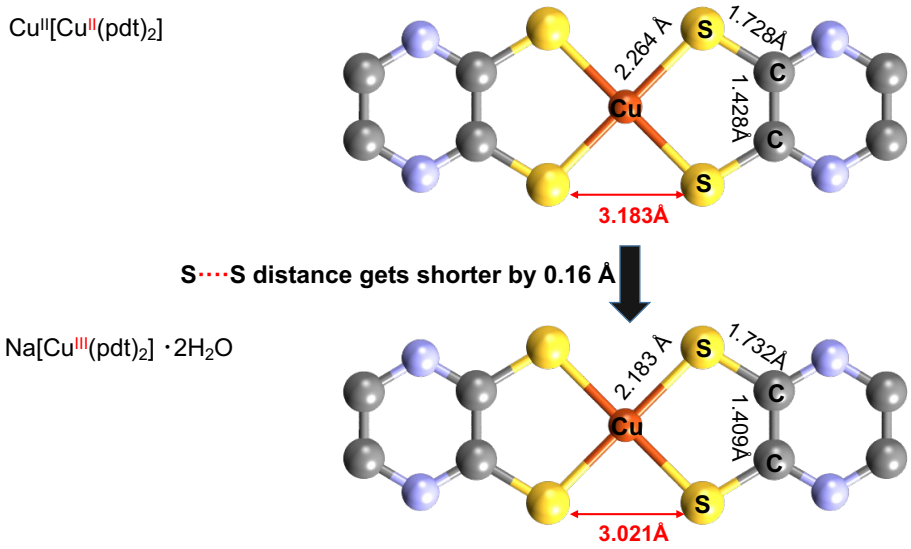

Figure 2.6.3 Bond distance analysis of Cu^{II} and Cu^{III} based pdt^{2-} complexes.

To clarify the reason for the shrinkage of the *c*-axis, the electronic structure investigation was performed using DFT calculations. As shown in **Figure 2.6.4**, the singly occupied molecular orbital (SOMO) of $[Cu^{II}(pdt)_2]^{2-}$ is mostly composed of the antibonding $d_{x^2-y^2}$ orbital of Cu and the S p_σ orbitals. As a result, the Cu–S bond distances of the optimized structures in $[Cu^{III}(pdt)_2]^{-}$ (2.24 Å) are shorter than those in $[Cu^{II}(pdt)_2]^{2-}$ (2.35 Å). In the actual compounds, the Cu–S bond length of $Na[Cu^{III}(pdt)_2]$ (2.18 Å)[44] which is shorter than that of $Cu^{II}[Cu^{II}(pdt)_2]$ (2.26 Å) .[42] Thus, it can be understand that when Cu^{II} is

oxidizing to Cu^{III}, the electron is removed from the antibonding orbital and hence causes the strengthening of bond order which results in the shortening of Cu–S bond length. From the crystal packing **Figure 2.6.5**, the Cu-S bond lies along *c*-axis. Hence, the shortening of the Cu–S bond caused the *c*-axis to shorten, whereas it did not affect the *a*-axis. Thus, the shortening of the *c*-axis could be attributed to the oxidation of $[Cu^{II}(pdt)_2]^{2-}$ to $[Cu^{III}(pdt)_2]^{-}$ by the bromine vapor.

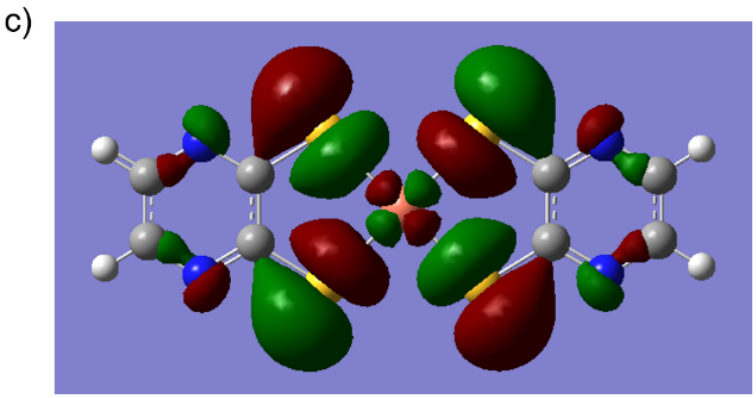

Figure 2.6.4 SOMO of $[Cu^{II}(pdt)_2]^{2-}$

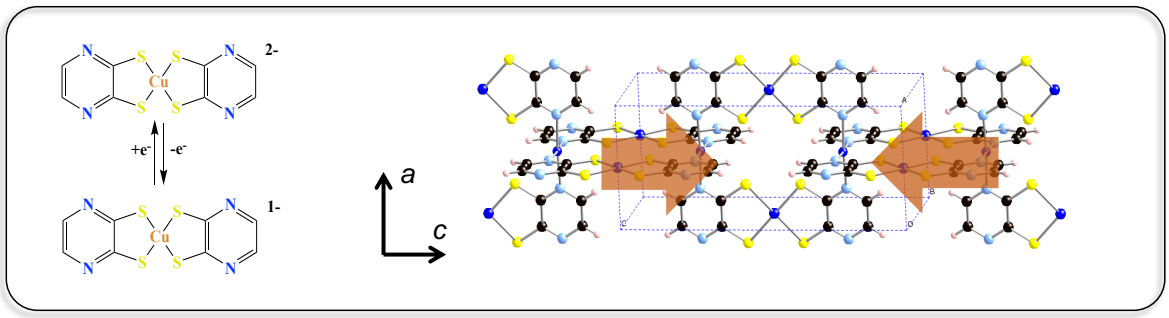

Figure 2.6.5 Alignment of Cu-S bond in a unit cell.

This fact is also supported by the redox potential of the $Cu(pdt)_2$ species and bromine. Robira and co-workers have reported a reversible Cu^{II}/Cu^{III} redox wave in the cyclic voltammogram (CV) of $TBA[Cu^{III}(pdt)_2]$ at $E_{1/2}$ = –0.33 V vs. Ag/AgCl,[44] which corresponds to ca. –0.13 V vs. standard hydrogen electrode (SHE). Kobayashi and co-workers also reported the solid state CV of $Cu[Cu(pdt)_2]$ and showed reversible redox wave at $E_{1/2}$ = –0.65 V vs. Ag/Ag^+ (ca. +0.15 V vs SHE),[35] Since these are much lower than the bromine reduction potential ($E°$ = 1.066 V vs. SHE for $Br_2(l) + 2e^- \rightarrow 2Br^-$),[45] so, it can be estimated that bromine vapor can oxidize $[Cu^{II}(pdt)_2]^{2-}$ to $[Cu^{III}(pdt)_2]^-$.

2.7 Optical Properties

2.7.1 Raman Spectra

In order to visualize the effect of bromine doping on the optical properties of $Cu[Cu(pdt)_2]$, we measured Raman spectra as show in **Figure 2.7.1**. A prominent peak was observed around 160 cm^{-1}. This peak was assigned to the Cu-pdt symmetrical stretching vibrational (A_g) mode. The Raman shift of this peak gradually shifted from 157 cm^{-1} (x = 0) to 163 cm^{-1} (x = 0.95). Using DFT calculations, the vibrational frequency of $[Cu^{II}(pdt)_2]^{2-}$ and $[Cu^{III}(pdt)_2]^-$ were calculated to be 134.3 and 148.3 cm^{-1}, respectively. Although the absolute values of the calculated Raman shifts are different from the experimental values. Which could probably be because, the calculations were done on isolated molecules. Moreover, this shift in the Raman peaks supports that the $Cu(pdt)_2$ moiety has been oxidized by the bromine vapor.

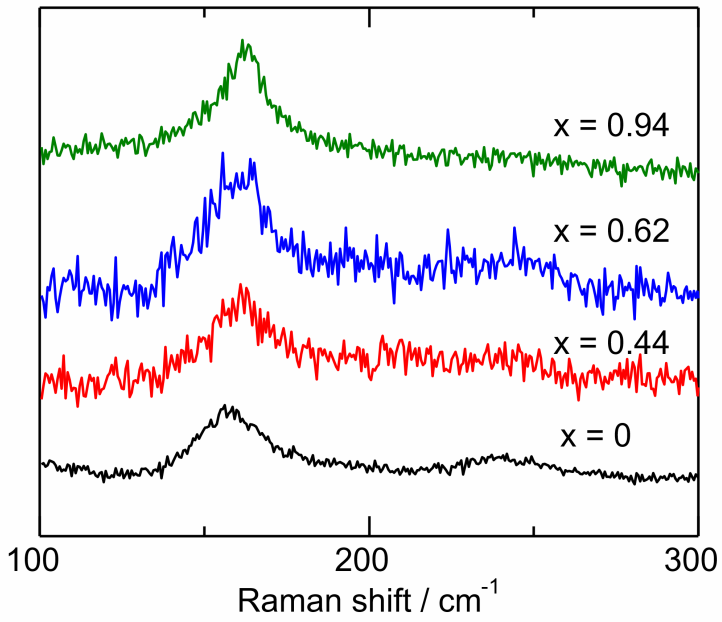

Figure 2.7.1.1 Raman spectra of Br_x@Cu[Cu(pdt)$_2$].

It was quite challenging to assign the electronic state of bromine. Typically, there are three possible forms of bromine, namely molecular bromine (Br_2), bromide (Br^-) and tribromide (Br_3^-). It is well known that Br_2 and Br_3^- species shows Raman signals at around 320 and 160 cm^{-1}, respectively,[46,47] whereas monoatomic Br^- should show no Rama signal. Although it is hard to determine the existence of Br_2 or Br_3^- species since pristine Cu[Cu(pdt)$_2$] originally possesses Raman peak at these areas **Figure 2.7.2a**. Since there is no prominent increase of Raman signal intensity upon bromine doping, hence we suppose that bromine is in the Br^- form. Although a detailed study is required in order to tackle this assignment.

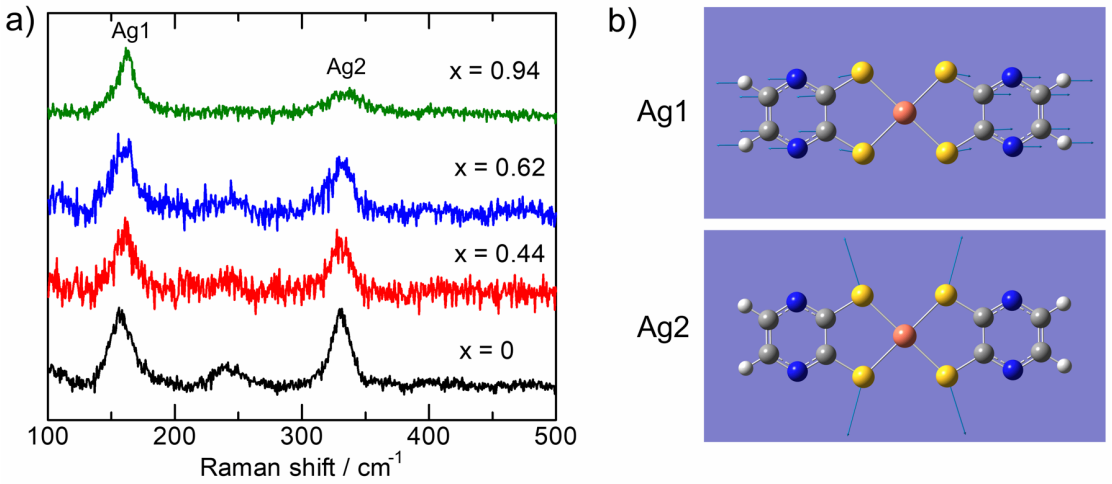

Figure 2.7.1.2 (a) Raman spectra of Br_x@Cu[Cu(pdt)$_2$]. **(b)** Schematic illustration of the displacement vectors of the Ag1 and Ag2 modes of Cu(pdt)$_2$.

Here we consider the chemical formula of the partially oxidized Br_x@Cu[Cu(pdt)$_2$]. If all of the Cu(pdt)$_2$ species are crystallographically equivalent, the compounds should be formulated as Br^{-}_{x}@Cu^{II}[Cu^{2+x}(pdt)$_2$]. On the other hand, given that Cu^{II}(pdt)$_2$ and Cu^{III}(pdt)$_2$ are distributed in the crystal, the compounds should be formulated as Br^{-}_{x}@Cu^{II}[Cu^{II}(pdt)$_2$]$_{1-x}$[Cu^{III}(pdt)$_2$]$_x$. The former one denotes a partially oxidized state and should be categorized as class III of the Robin-Day classification of mixed valency.[49] On the other hand, the latter one should be categorized as class II of the Robin-Day classification of mixed valency.[49] Although it is impossible to distinguish them from the conventional PXRD studies since X-ray diffraction reflects the averaged crystal structure, the former and latter states should give metallic and semiconductive properties, respectively.

2.7.2 UV-vis-NIR Spectra

UV-vis-NIR diffuse reflectivity spectra in the range of 2000–350 nm (0.6–3.5 eV, black line) and FT-IR spectra (0.1–0.5 eV, red lines) of Br_x@Cu[Cu(pdt)$_2$] were measured and are shown in Figure 2.7.2. Samples were diluted with $BaSO_4$ as matrix. Obtained diffuse reflectivity spectra were converted into absorption spectra by Kubelka-Munk function.UV-vis-NIR spectra. The spectra of the pristine compound showed a broad absorption peak appeared around 1.3 eV, indicating a narrow band gap of this compound and is a semiconductor. The narrowere band gap is the origin of the electrical conductivity. On the other hand, in case of bromine doped spectra, the absorption peak shifted to lower energy, and a new band was observed around 0.3 eV. The shift of the absorption band supports that the bromine oxidizes $[Cu^{II}(pdt)_2]^{2-}$ to $[Cu^{III}(pdt)_2]^{-}$, modulating their electronic states. The absorbance below 0.3 eV started to decrease with a decrease in the photon energy at each amount of bromine, indicating that bromine doped compounds still had a finite band gap. Thus, we concluded that the electronic states of Br_x@Cu[Cu(pdt)$_2$] were in a semiconductive ground state due to their segregated valence states (formulated as Br^{-}_x@$Cu^{II}[Cu^{II}(pdt)_2]_{1-x}[Cu^{III}(pdt)_2]_x$). We also measured the temperature dependent electrical conductivity of Br_x@Cu[Cu(pdt)$_2$] which further confirms semiconductive nature of the doped sample. Although we assume that this absorption band is assigned to the intervalence charge-transfer (IVCT) band from Cu^{II} to Cu^{III} species, further study has to be done to confirm this assignment.

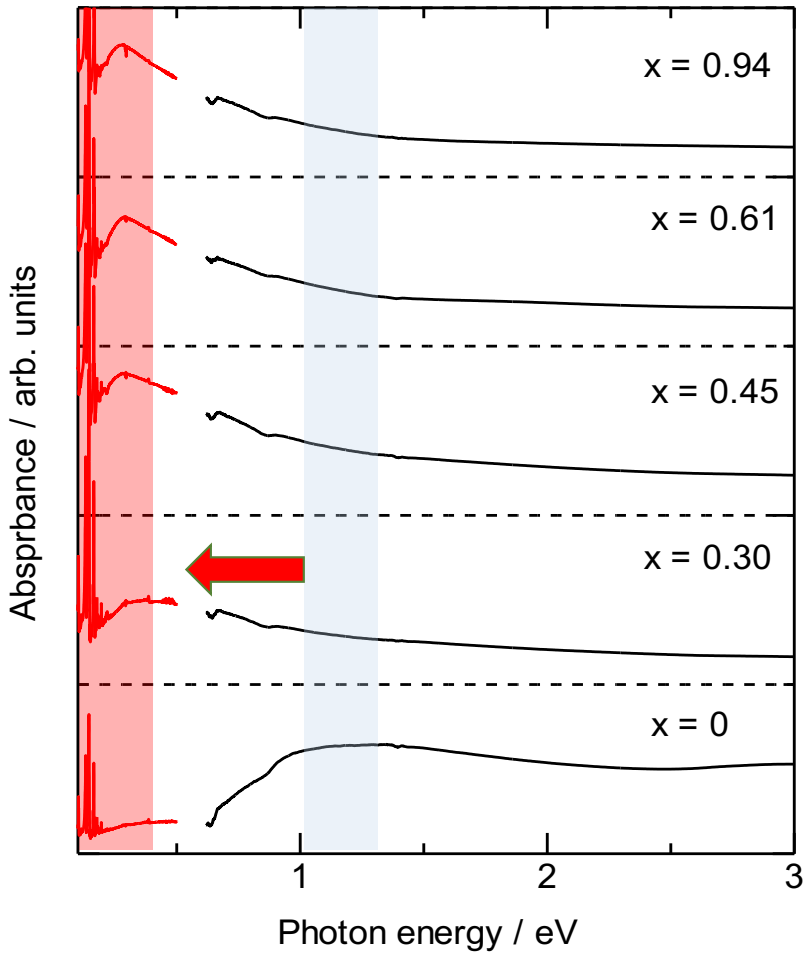

Figure 2.7.2 UV-vis-NIR (black lines) and FT-IR spectra (red lines) of Br_x@Cu[Cu(pdt)$_2$].

Semiconductive Properties

2.8 Electrical Conductivity

The electrical conductivities were measured with the help of current (*I*)-voltage (*V*) characteristics of compressed pellet (3 mmϕ) samples using two-electrode configurations at 293 K. The current (*I*)-voltage (*V*) plots were converted to current density (*J*) and electric field (*E*) using a value of 0.07 cm^2 as surface area and a thickness of typically 0.05 cm. **Figure 2.8.1 a** shows *J*-*E* characteristics of Br_x@Cu[Cu(pdt)$_2$]. Slope of *J*-*E* curve at *E* = 0 gives the value of the electrical conductivity of each sample. The conductivity of

$Cu[Cu(pdt)_2]$ was 1.4×10^{-4} S cm^{-1}. In the case of $Br_x@Cu[Cu(pdt)_2]$, the conductivity was increased by an order of magnitude higher than those of the pristine compounds. **Figure 2.8.1 b** This is probably because the band filling changed due to the partial oxidation of $[Cu^{II}(pdt)_2]^{2-}$ to form mixed valence $Br^{-}_x@Cu^{II}[Cu^{II}(pdt)_2]_{1-x}[Cu^{III}(pdt)_2]_x$. while looking at **Figure 2.8.1 a**, it can be seen that the *J-E* curves of the bromine doped compounds around $x = 0.5$ were highly nonlinear. Such a nonlinear curve is often observed for organic semiconductors and is explained by melting of the charge order[50] or sliding of the charge-density wave.[51] Although we do not have any data on the arrangement of the $Cu^{II}(pdt)_2$ and $Cu^{III}(pdt)_2$ species in the crystal, there may be some ordering which would give a similar mechanism.

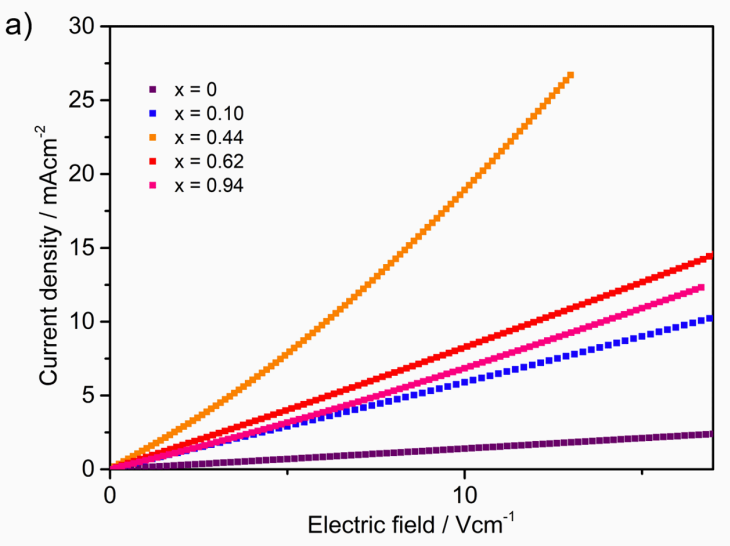

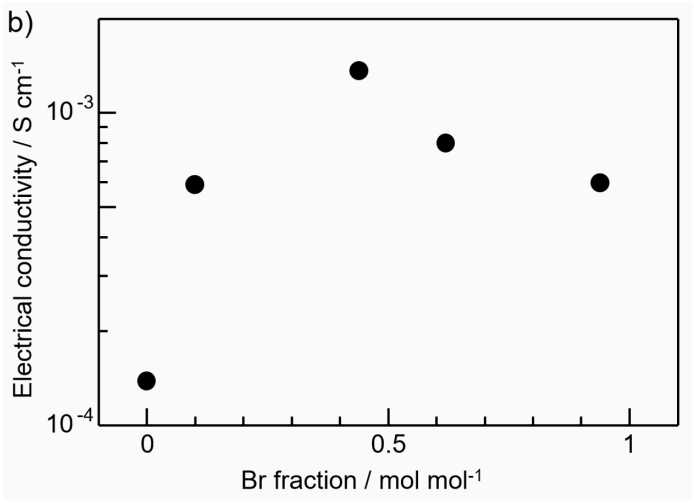

Figure 2.8.1 (a) J-E characteristics and **(b)** electrical conductivity at 293 K as function of Br fraction.

Further in order to confirm semiconductive nature of bromine doped samples, we measured temperature dependence of the electrical conductivity of one of the Br_x@Cu[Cu(pdt)$_2$] samples. We decided to choose $Br_{0.44}$@Cu[Cu(pdt)$_2$] x = 0.44. In **Figure 2.8.2 a**, the electrical conductivity increases with temperature which showed semiconductive temperature dependency. Upon fitting the conductivity data using Arrhenius plot, It showed an activation energy of 220 meV. This finding indicates that the bromine doped compounds possesses a finite band gap, which is consistent with the optical data.

a)

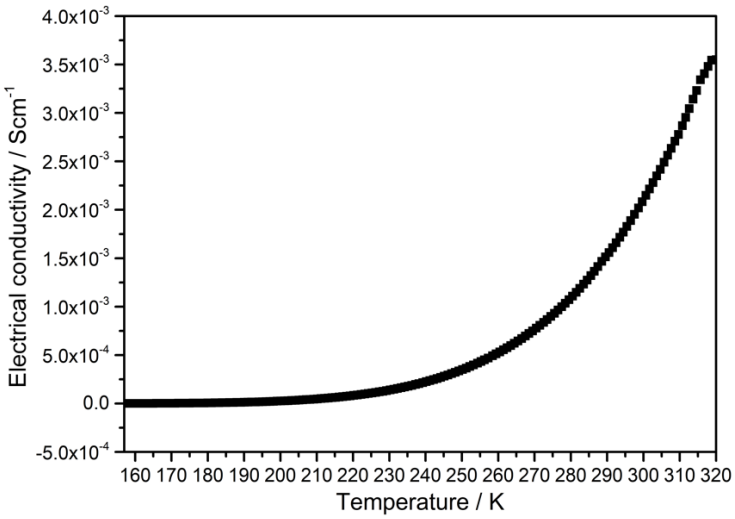

b)

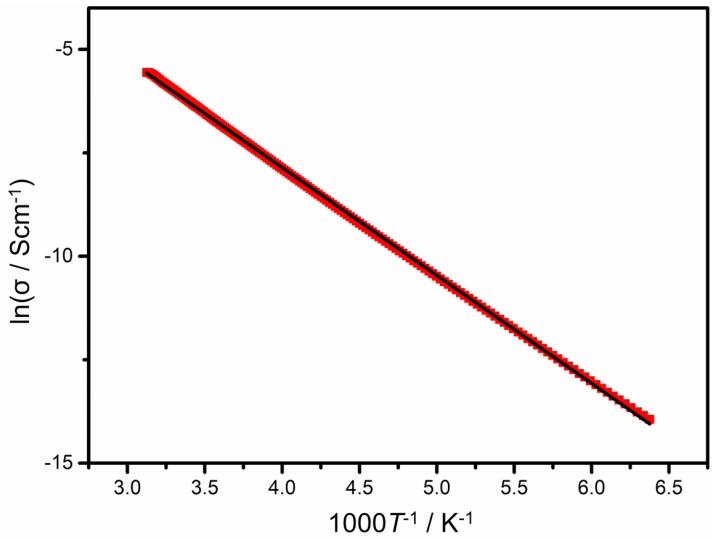

Figure 2.8.2 (a) Temperature dependent of the electrical conductivity of $Br_{0.44}$@Cu[Cu(pdt)$_2$]. **(b)** Arrhenius plot of the electrical conductivity in $Br_{0.44}$@Cu[Cu(pdt)$_2$].

Since the conductivity enhancement was an order higher that the pristine one. Sometimes it might be because of crystal- terminal contact issues. Usually, conductivity measurements on pellet samples are not very accurate because of the interference of the

grain boundary effect. So, in order to clarify that the conductivity enhancement is a result of the bromine doping (not due to the crystal-terminal contact issue), we performed a time-course measurement of the single crystal electrical resistance of the $Cu[Cu(pdt)_2]$ *in-situ* bromine doping. **(Figure 2.8.3)** Electrical resistance promptly decreased after exposure to Br_2 vapor and became 1/40 after a spam of 2000 sec. This result clearly indicates that the decrease of the resistance is result of the bromine doping.

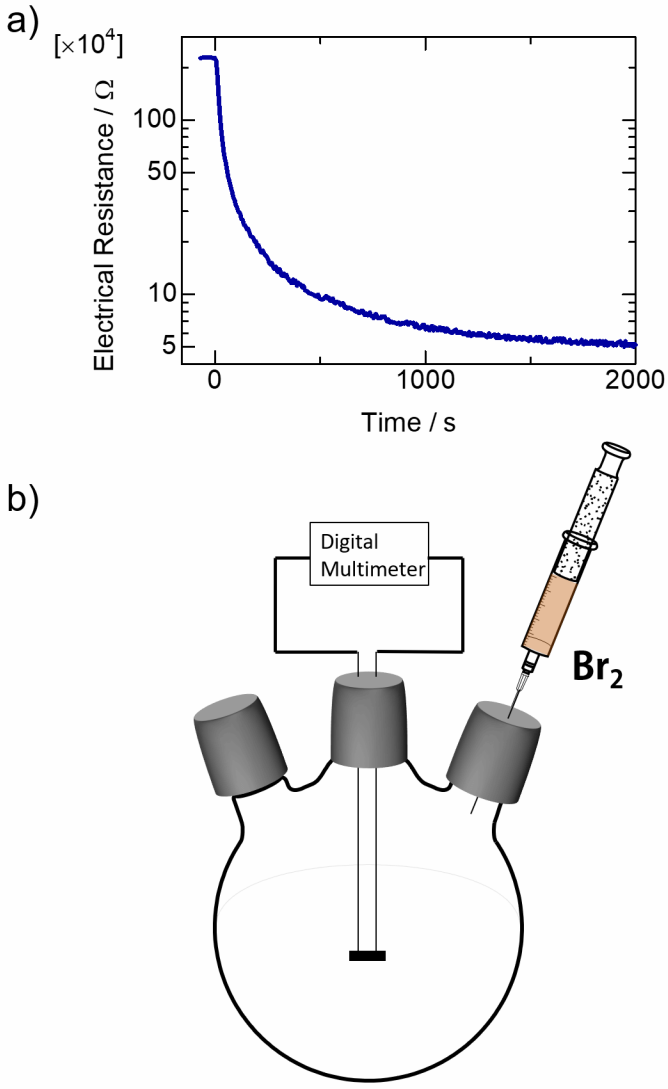

Figure 2.8.3 (a) Time course of the electrical resistance of a $Cu[Cu(pdt)_2]$ single crystal upon Br_2 doping. Br_2 vapor was injected at $T = 0$ sec. **(b)** Apparatus for the meausrement.

2.9 Thermoelectric properties

The thermoelectric properties are powerful tools for clarifying the electronic states of the materials. Positive and negative sign of Seebeck coefficients indicate that the conduction carriers are holes and electrons, respectively. Recently, So and co-workers have reported the effects of metal substitution from Ni to Pt on the thermoelectric properties of M-HITP (M = Ni or Pt and HITP = 2,3,6,7,10,11-hexaiminotriphenylene) and demonstrate that M-HITP, in contrast to pristine MOF, starts behaving like p-type semiconductor as the Ni center are replaced by Pt.[52] In addition, Bao and co-workers have investigated the effects of the atmospheric environment on a series of M-HAB (M = Co, Ni and Cu; HAB = hexaaminobenzene) and reported that the type of majority of charge carrier has changed from electrons to holes upon changing the environment from ambient to N_2 atmospheres.[53]

Charge carrier type investigation was performed with the help of the thermoelectromotive forces (ΔV) measurement. Thermoelectric properties were measured using a home-built apparatus as shown in **Figure 2.9.1** The details are described in the section.

Measurement was performed on pressed pellets of a series of pristine and doped samples at an ambient temperature and normal atmospheric condition (details of measurement setup are shown in **Figure 2.9.1**. **Figure 2.9 a** shows ΔV as a function of ΔT. Seebeck coefficients were determined from the slope of the plot ($S = -\Delta V/\Delta T$). The pristine $Cu[Cu(pdt)_2]$ MOF exhibits a Seebeck coefficient of +337 $\mu V\ K^{-1}$, indicating that it is a p-type semiconductor.

a)

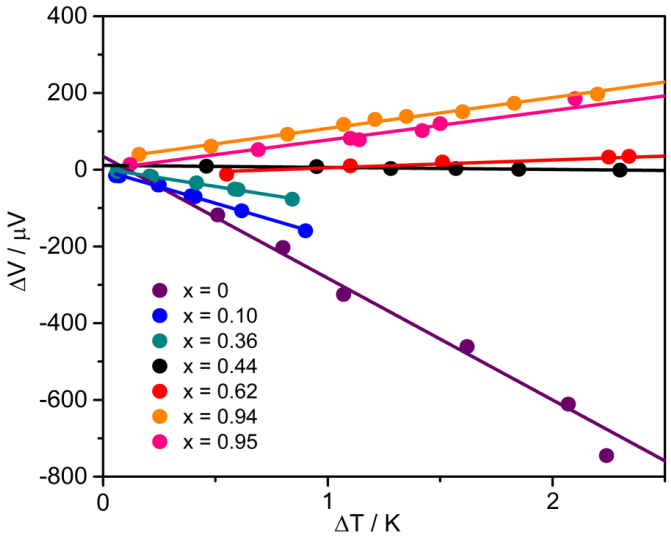
400
200
0
-200
-400
-600
-800
ΔV / μV
0
1
2
ΔT / K
x = 0
x = 0.10
x = 0.36
x = 0.44
x = 0.62
x = 0.94
x = 0.95

b)

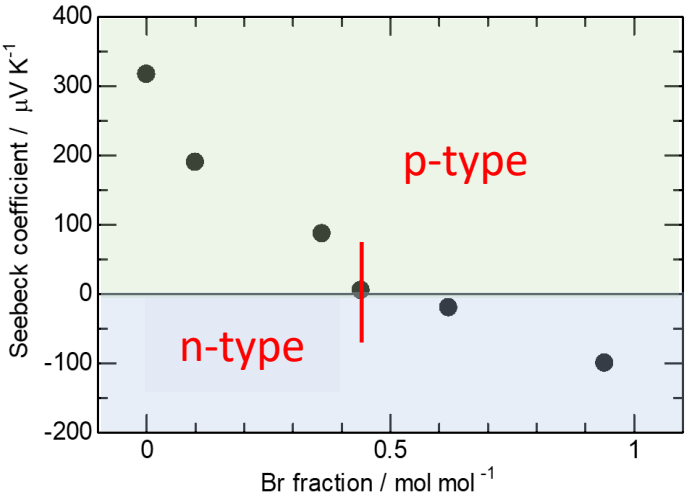
400
300
200
100
0
-100
-200
Seebeck coefficient / μV K-1
p-type
n-type
0
0.5
1
Br fraction / mol mol -1

c)

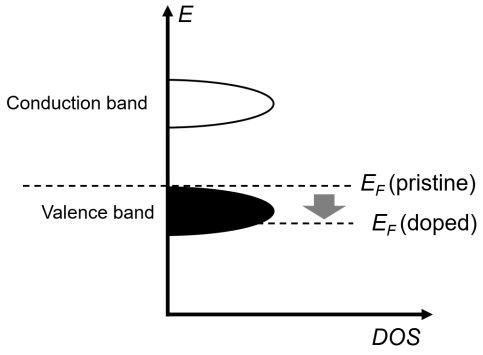
E
Conduction band
Valence band
EF (pristine)
EF (doped)
DOS

Figure 2.9 (a) Thermoelectromotive force of Br_x@Cu[Cu(pdt)$_2$], **(b)** Seebeck coefficients and **(c)** Schematic illustration of plausive band structure of Cu[Cu(pdt)$_2$].

Figure 2.9 b shows the change of Seebeck coefficient as function of Bromine doping. And it shows that the pristine MOF has a positive Seebeck coefficient with a value of +337 μV K^{-1} and it started decreasing as the bromine fraction increases and after a certain level of doping the sign of Seebeck coefficient has changed to negative. Which implies that the charge carrier type has changed from holes in the pristine MOF to electrons in the doped one.

Recently, Syrotyuk and co-workers have reported the results of band calculations on Cu[M(pdt)$_2$] (M = Ni and Cu), assuming that Cu[Cu(pdt)$_2$] is a p-type semiconductor, which is consistent with the positive Seebeck coefficient.[54] The Seebeck coefficient gradually decreased with an increase in the amount of bromine doping, and it became negative when $x > 0.5$. Figure 6b shows the x dependence of the Seebeck coefficient, and it was clarified that the sign of the Seebeck coefficient changed at the boundary of $x = 0.5$. Here we discuss the origin of this phenomenon. The oxidation state of Cu ions of the pristine compound is $Cu^{II}[Cu^{II}(pdt)_2]$. Meanwhile, as we stated above, $[Cu^{II}(pdt)_2]^{2-}$ can easily be oxidized to $[Cu^{III}(pdt)_2]^{-}$, while is hardly reduced to $[Cu^{I}(pdt)_2]^{3-}$, indicating that the charge carriers of hole are thermally generated, in other words, the Fermi energy (E_F) is closer to top of the valence band than bottom of the conduction band as shown in **Figure 2.9 c** which is in the p-type semiconductor. On the other hand, the bromine-doped compound is in the $[Cu^{III}(pdt)_2]^{-}$ state, which can easily be reduced to $[Cu^{II}(pdt)_2]^{2-}$

whereas hardly oxidized to $[Cu^{IV}(pdt)_2]^0$ (**Figure 2.9 d)**, indicating that the charge carriers of electron are thermally generated (n-type semiconductor).

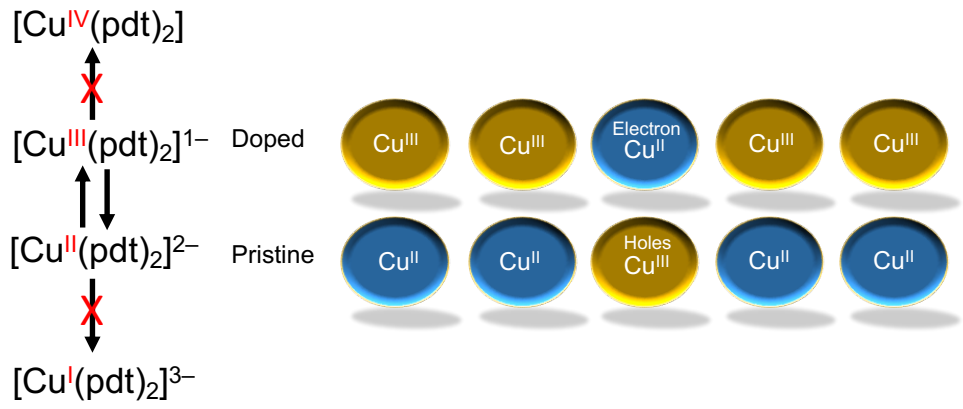

Figure 2.9 (d) Schematic representation of conversion of conducting carriers.

Seebeck coefficient is determined using the following equation:

$$S = -\frac{\pi^2 k_B^2 T}{3e}\left(\frac{d\ln N(E)}{dE}\right)_{E = E_F}$$

where k_B is the Boltzmann constant, N is the density of state.[55] This equation is known as the Mott's formula. According to this equation, the Seebeck coefficient is related to the derivative of logarithmic density of states (DOS) at the fermi level (E_F). In other words, the Seebeck coefficient is closely related to the slope of DOS at E_F. which is basically the variation of σ (E) above and below the fermi level. Or in other words S signifies the asymmetry of electronic structure near fermi level. Although a quantitative discussion cannot be done at present, the change in the sign of the Seebeck coefficient is a result of the oxidation, i.e., hole doping. This phenomenon is schematically illustrated in **Figure**

2.9 c. To the best of our knowledge, this is the first example of a change in the type of conduction carrier via postsynthetic carrier doping.

Iodine doping effect on electrical conductivity and Seebeck coefficient.

2.10 Iodine doping

After Br doping, we also investigated effect of I doping. Taking the advantage of porosity I_2 doping was performed using 100 mg of $Cu[Cu(pdt)_2]$ at a time and varying the amount of I_2. Detailed experimental setup for I_2 doping is described in **Figure 2.10**. Iodine doping was performed using the following procedure. Polycrystalline $Cu[Cu(pdt)_2]$ (100 mg) was placed into a screwed vial along with iodine in a small vial. Different amount of Iodine (solid) was placed in a small vial. The schematic drawing of the experimental apparatus is shown in **Figure 2.10**. After doping with Iodine, all samples were annealed for 24 h at 60 °C.

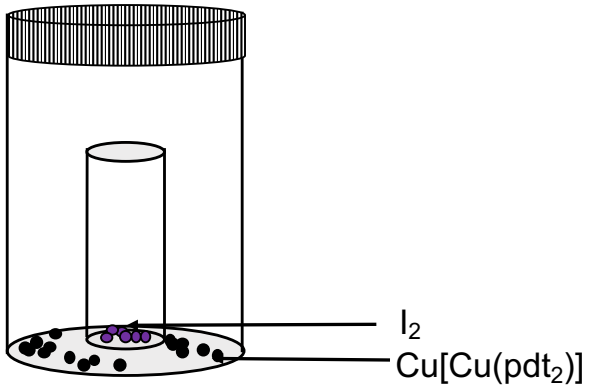

Figure 2.10. Apparatus for the Iodine doping into $Cu[Cu(pdt)_2]$.

We incorporated different amount of I_2 while keeping the amount of MOF constant to afford I_x@Cu[Cu(pdt)$_2$] ($0 \leq x \leq 0.9$). it was realized that even if we used an excess amount of I_2, the I fraction (x) of I_x@Cu[Cu(pdt)$_2$] was approximately 1, indicating that $x \approx 1$ is the upper limit of the I loading. This finding indicates that I atoms is not merely physiosorbed but electronically interact with Cu[Cu(pdt)$_2$]. The amount of iodine inside the MOF was investigated using halogen and Sulfur analysis as shown in **Table 3.**

RatioCu[Cu(pdt$_2$)]:I$_2$)	Expected formula	Expected S:I	Found S:I
100:5	Cu[Cu(pdt)$_2$].I$_{0.22}$.ACN$_{1.5}$	25.60:5.57	25.88:5.66
100:10	Cu[Cu(pdt)$_2$].I$_{0.38}$.ACN$_{1.4}$	24.80:9.32	25.13:9.19
100:15	Cu[Cu(pdt)$_2$].I$_{0.64}$.ACN$_{1.5}$	23.14:14.65	23.30:14.29
100:20	Cu[Cu(pdt)$_2$].I$_{0.89}$. ACN$_{1.5}$	22.08:18.57	22.65:18.84

Table 3. Elemental analysis data for Br$_x$@Cu[Cu(pdt)$_2$]

2.11 Structural investigation of I_x@Cu[Cu(pdt)$_2$]

X-ray diffraction patterns of I_x@Cu[Cu(pdt)$_2$] were plotted with respect to 2θ in **Figure 2.11 a**. It reveals that PXRD patterns of I_x@Cu[Cu(pdt)$_2$] are isomorphic with pristine Cu[Cu(pdt)$_2$], and the crystallinities of the doped samples were retained, which further confirms that the I doping does not change the intrinsic skeleton of the MOFs. However, with the inclusion of Iodine, the intensity of the peak for the (100) face of I_x@Cu[Cu(pdt)$_2$] continuously decreased with an increase in x. This corresponds to the successive incorporation of iodine molecules into the pores of Cu[Cu(pdt)$_2$].

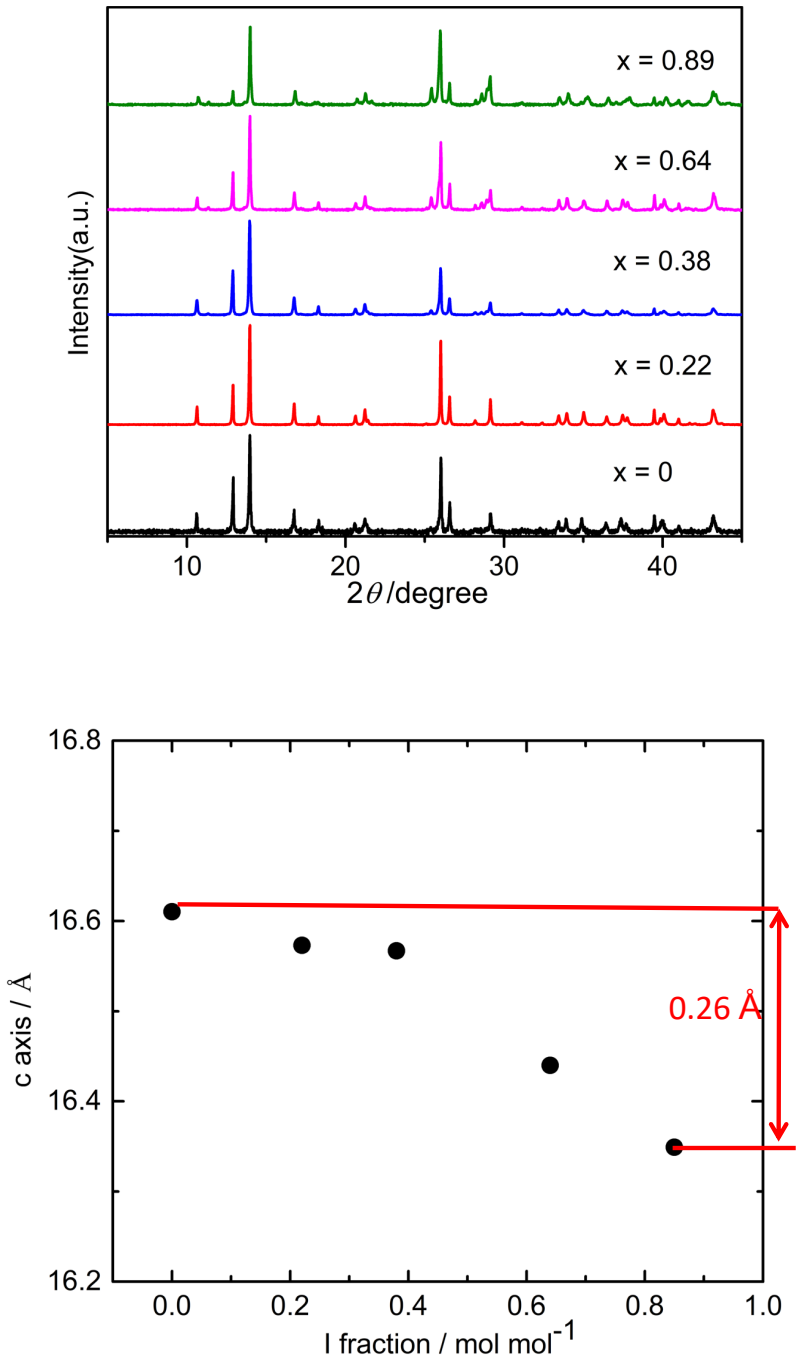

Figure 2.11 (a) PXRD patterns of I_x@Cu[Cu(pdt)$_2$]. **(b)** Lattice parameters of I_x@Cu[Cu(pdt)$_2$] as a function of the I fraction/mol.

The PXRD patterns of I_x@Cu[Cu(pdt)$_2$] were fitted using the Le Bail method to estimate the unit cell parameters (**Figure 2.11 b**). Although the lattice parameter *a*-axis has barely

changed but the *c*-axis significantly changed and it continuously shortened with an increase in *x*.

2.12 Electrical conductivity

The electrical conductivities were measured with the help of current (*I*)-voltage (*V*) characteristics of compressed pellet (3 mmϕ) samples using two-electrode configurations at 293 K. The current (*I*)-voltage (*V*) plots were converted to current density (*J*) and electric field (*E*) using a value of 0.07 cm^2 as surface area and a thickness of typically 0.05 cm. The conductivity of $Cu[Cu(pdt)_2]$ was 1.4×10^{-4} S cm^{-1}. **Figure 2.12** shows, in the case of $I_x@Cu[Cu(pdt)_2]$, the conductivity was increased by 30 times of higher magnitude than those of the pristine compounds. This is probably because the band filling changed due to the partial oxidation of $[Cu^{II}(pdt)_2]^{2-}$ to form mixed valence $I^-_x@Cu^{II}[Cu^{II}(pdt)_2]_{1-x}[Cu^{III}(pdt)_2]_x$.

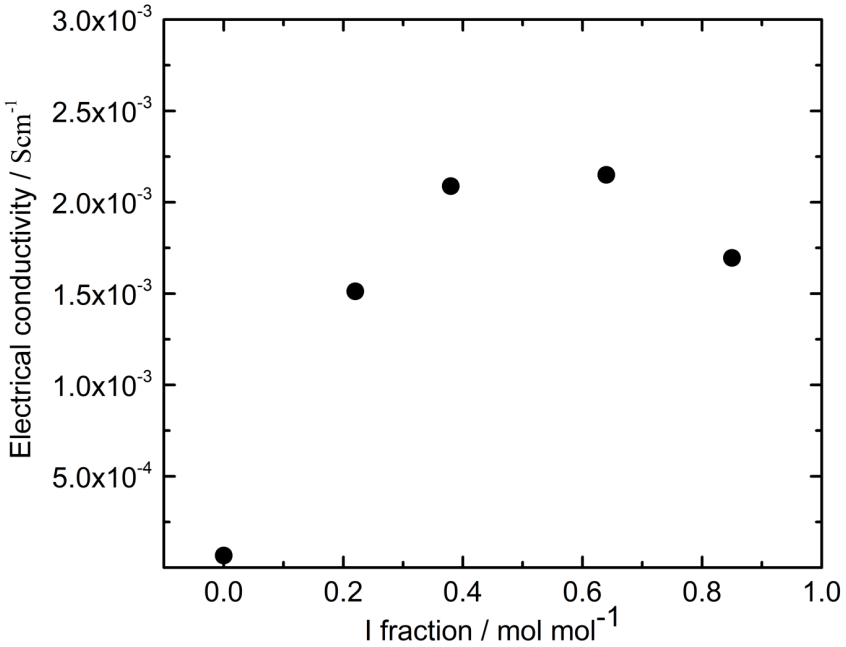

Figure 2.12 Electrical conductivity at 293 K as function of I fraction.

2.13 Thermoelectromotive Force Measurement

Conducting carrier type investigation was performed with the help of the thermoelectromotive forces (ΔV) measurement. Measurement was performed on pressed pellets of a series of pristine and doped samples at an ambient temperature and normal atmospheric condition (details of measurement setup are shown in **Figure 2.14.** Seebeck coefficients were determined from the slope of the plot ($S = -\Delta V/\Delta T$). The pristine Cu[Cu(pdt)$_2$] MOF exhibits a Seebeck coefficient of +225 μV K^{-1}, indicating that it is a p-type semiconductor. Upon Iodine doping change in conducting carrier was observed and charge carrier type has changed from holes in the pristine MOF to electrons in the iodine doped one.

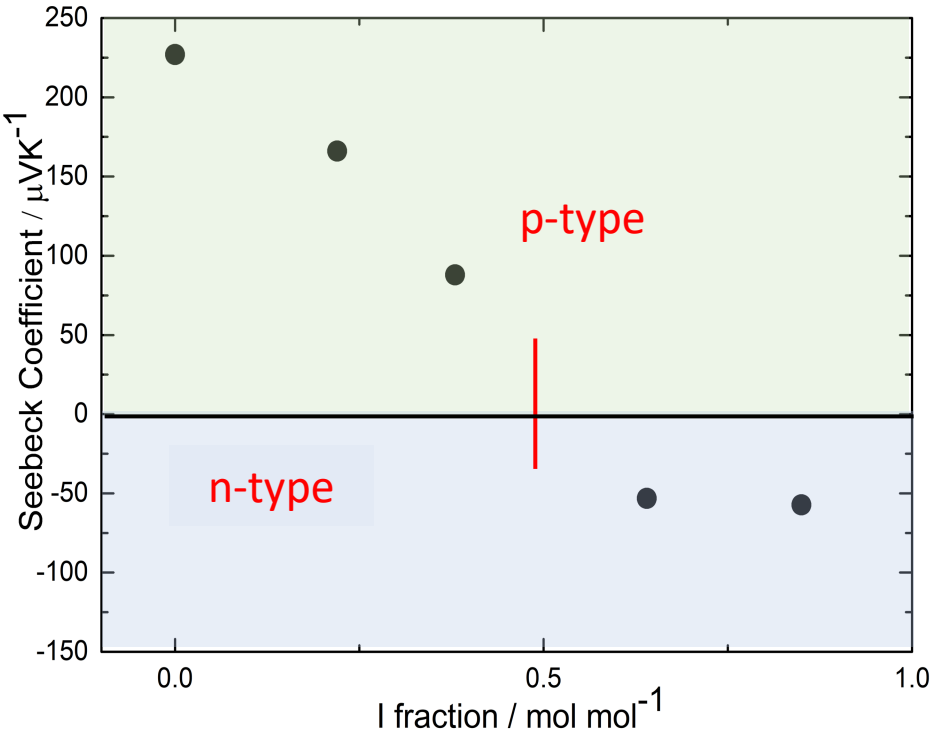

Figure 2.13 Thermoelectromotive force of I$_x$@Cu[Cu(pdt)$_2$].

2.14 Experimental Details of the thermoelectromotive force measurement

Apartus for the thermoelectromotive force measurement is shown in **Figure 2.14.1**. Heating and cooling were realized using peltier module attached on the aluminium blocks. An aluminium block was placed on the each peltier module with heat conducting double-sided tape. The pellet sample was mounted on the alminium blocks so as that the pellet bridges the two alminum block. A little amount of Apiezon N grease was used to fix the pellet. Copper-constantan (T-type) thermocouples with 100 μmϕ was put with the carbon paste (Fujikura XC-12) at the both side of the pellet. The DC current was added to the both peltier module using Kikusui 7316 regulated DC current source as illustrated in **Figure 2.14.1** (a) so as that one side is cooled and another side is heated. The V_1 and V_2 were measured using Agilent 34420A Nanovolt / Microohm meter. The thermoelectromotive force was measured from V_1. The contribution of the copper wire was ignored because the thermoelectromotive force of copper (+1.94 μV/K at 300 K)[S1] is much smaller than that of Br_x@Cu[Cu(pdt)$_2$] sample. The temperature defference (ΔT) was evaluated using the following equation.

$$\Delta T = \frac{V_2 - V_1}{\alpha_{\mathrm{T}}}$$

where, α_{T} represents the thermopower of T-type (Copper-Constantan) thermocouple. α_{T} = 40 μV/K at 20 °C was used.

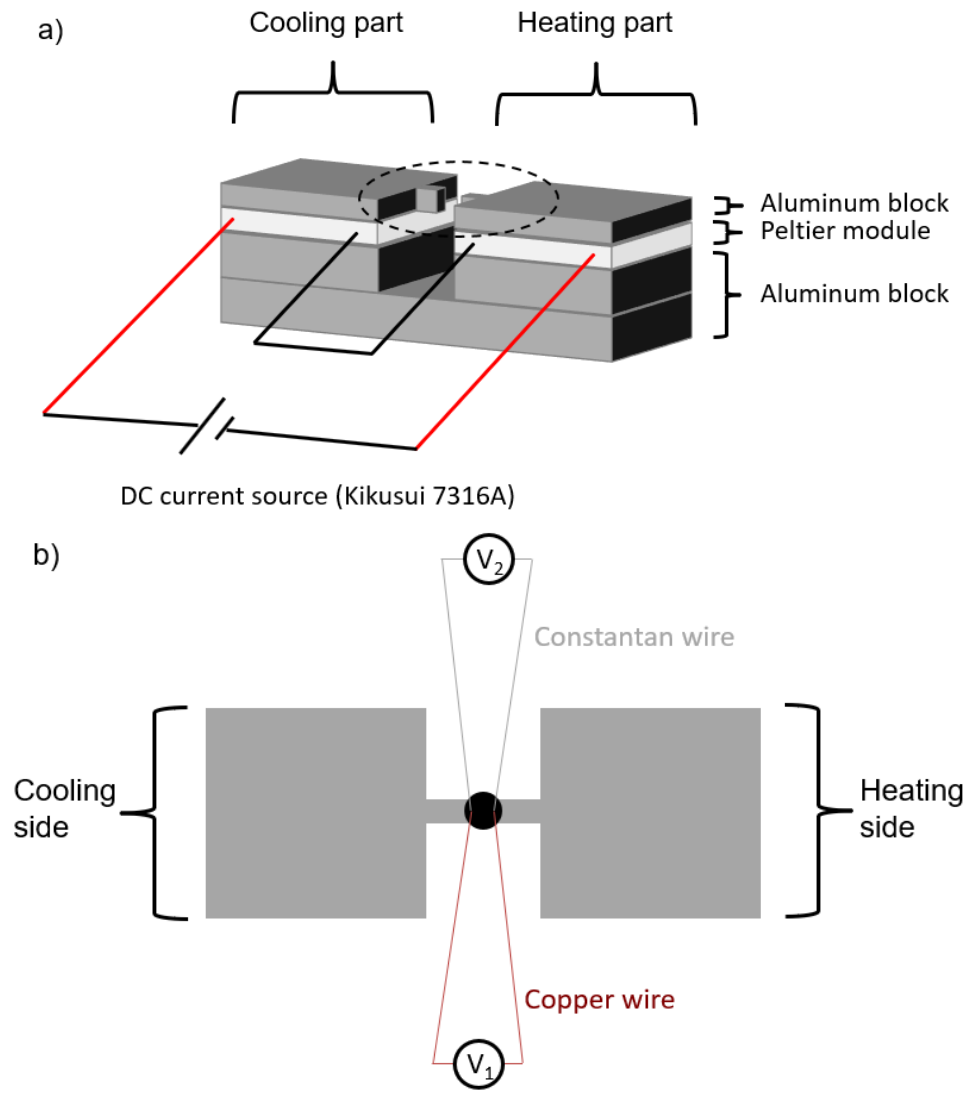

Figure 2.14.1 a) Apparatus for the measurments of thermoelectromotive force. **b)** magnification of the sample part (broken circle in a)).

2.15 Conclusions

We presented the extended application range of the $Cu[Cu(pdt)_2]$ MOF in the field of electronics. To the best of our knowledge, for the first time, we have investigated the detailed study of halogen doping and its effects on structural, optical, semiconductive and thermoelectric properties of the $Cu[Cu(pdt)_2]$ MOF. We studied continuous changes upon controlled doping of halogen. Taking advantage of porosity, encapsulation of halogen was performed. Halogen molecules act as an oxidizing agent, and it causes the oxidation of the framework. as a result, enhancement in electrical conductivity was realized by an order one. And the reason for that is redox hopping between the partially oxidized copper centre. All the experimental results, such as Raman spectra, UV-vis near IR spectra and single crystal resistivity measurement, supports the fact. Later, we reported a detailed study on charge carrier type. And type of charge carrier investigation was performed with the help of thermoelectromotive force measurement. It was shown that the pristine MOF has a positive Seebeck coefficient with a value of +337 $\mu V\ K^{-1}$ and, it started decreasing as the halogen fraction increased, and after a certain level of doping the sign of Seebeck coefficient has changed to a negative. This implies that the charge carrier type changed from holes in the pristine MOF to electrons in the doped one. Moreover, with selective doping, the type of conductivity carriers could be modulated while maintaining the original structure. The halogen doping resulted in a 30-fold increase in the electrical conductivity. The improved conductivity and device engineering will make this material a versatile candidate for the field of MOF-based electronic devices.

Reference:

(1) Rosi, N. L. Hydrogen Storage in Microporous Metal-Organic Frameworks. *Science* **2003**, *300* (5622), 1127–1129. https://doi.org/10.1126/science.1083440.

(2) Farha, O. K.; Özgür Yazaydın, A.; Eryazici, I.; Malliakas, C. D.; Hauser, B. G.; Kanatzidis, M. G.; Nguyen, S. T.; Snurr, R. Q.; Hupp, J. T. De Novo Synthesis of a Metal–Organic Framework Material Featuring Ultrahigh Surface Area and Gas Storage Capacities. *Nat. Chem.* **2010**, *2* (11), 944–948. https://doi.org/10.1038/nchem.834.

(3) Farha, O. K.; Eryazici, I.; Jeong, N. C.; Hauser, B. G.; Wilmer, C. E.; Sarjeant, A. A.; Snurr, R. Q.; Nguyen, S. T.; Yazaydın, A. Ö.; Hupp, J. T. Metal–Organic Framework Materials with Ultrahigh Surface Areas: Is the Sky the Limit? *J. Am. Chem. Soc.* **2012**, *134* (36), 15016–15021. https://doi.org/10.1021/ja3055639.

(4) Suh, M. P.; Park, H. J.; Prasad, T. K.; Lim, D.-W. Hydrogen Storage in Metal–Organic Frameworks. *Chem. Rev.* **2012**, *112* (2), 782–835. https://doi.org/10.1021/cr200274s.

(5) Hu, Y.; Liu, Z.; Xu, J.; Huang, Y.; Song, Y. Evidence of Pressure Enhanced CO_2 Storage in ZIF-8 Probed by FTIR Spectroscopy. *J. Am. Chem. Soc.* **2013**, *135* (25), 9287–9290. https://doi.org/10.1021/ja403635b.

(6) Alezi, D.; Belmabkhout, Y.; Suyetin, M.; Bhatt, P. M.; Weseliński, Ł. J.; Solovyeva, V.; Adil, K.; Spanopoulos, I.; Trikalitis, P. N.; Emwas, A.-H.; Eddaoudi, M. MOF Crystal Chemistry Paving the Way to Gas Storage Needs: Aluminum-Based **Soc** -MOF for CH_4 , O_2 , and CO_2 Storage. *J. Am. Chem. Soc.* **2015**, *137* (41), 13308–13318. https://doi.org/10.1021/jacs.5b07053.

(7) Li, J.-R.; Kuppler, R. J.; Zhou, H.-C. Selective Gas Adsorption and Separation in Metal–Organic Frameworks. *Chem. Soc. Rev.* **2009**, *38* (5), 1477. https://doi.org/10.1039/b802426j.

(8) Chang, N.; Gu, Z.-Y.; Wang, H.-F.; Yan, X.-P. Metal–Organic-Framework-Based Tandem Molecular Sieves as a Dual Platform for Selective Microextraction and High-Resolution Gas Chromatographic Separation of *n* -Alkanes in Complex Matrixes. *Anal. Chem.* **2011**, *83* (18), 7094–7101. https://doi.org/10.1021/ac2014004.

(9) Li, J.-R.; Sculley, J.; Zhou, H.-C. Metal–Organic Frameworks for Separations. *Chem. Rev.* **2012**, *112* (2), 869–932. https://doi.org/10.1021/cr200190s.

(10) Herm, Z. R.; Bloch, E. D.; Long, J. R. Hydrocarbon Separations in Metal–Organic Frameworks. *Chem. Mater.* **2014**, *26* (1), 323–338. https://doi.org/10.1021/cm402897c.

(11) Liu, K.; Li, B.; Li, Y.; Li, X.; Yang, F.; Zeng, G.; Peng, Y.; Zhang, Z.; Li, G.; Shi, Z.; Feng, S.; Song, D. An N-Rich Metal–Organic Framework with an Rht Topology: High CO2 and C2 Hydrocarbons Uptake and Selective Capture from CH4. *Chem. Commun.* **2014**, *50* (39), 5031. https://doi.org/10.1039/c4cc00375f.

(12) Cadiau, A.; Adil, K.; Bhatt, P. M.; Belmabkhout, Y.; Eddaoudi, M. A Metal-Organic Framework-Based Splitter for Separating Propylene from Propane. *Science* **2016**, *353* (6295), 137–140. https://doi.org/10.1126/science.aaf6323.

(13) Fu, Y.; Sun, D.; Qin, M.; Huang, R.; Li, Z. Cu(Ii)-and Co(Ii)-Containing Metal–Organic Frameworks (MOFs) as Catalysts for Cyclohexene Oxidation with Oxygen under Solvent-Free Conditions. *RSC Adv.* **2012**, *2* (8), 3309. https://doi.org/10.1039/c2ra01038k.

(14) Sun, Z.; Li, G.; Liu, H.; Liu, L. Salen-Co(II) Complex Incorporated into Amino-Functionalized MIL-101(Cr) through Postsynthetic Modification as a Cooperative

Catalyst for Cyclohexane Selective Oxidation. *Appl. Catal. Gen.* **2013**, *466*, 98–104. https://doi.org/10.1016/j.apcata.2013.06.032.

(15) Fei, H.; Shin, J.; Meng, Y. S.; Adelhardt, M.; Sutter, J.; Meyer, K.; Cohen, S. M. Reusable Oxidation Catalysis Using Metal-Monocatecholato Species in a Robust Metal–Organic Framework. *J. Am. Chem. Soc.* **2014**, *136* (13), 4965–4973. https://doi.org/10.1021/ja411627z.

(16) Liu, F.; Xu, Y.; Zhao, L.; Zhang, L.; Guo, W.; Wang, R.; Sun, D. Porous Barium–Organic Frameworks with Highly Efficient Catalytic Capacity and Fluorescence Sensing Ability. *J. Mater. Chem. A* **2015**, *3* (43), 21545–21552. https://doi.org/10.1039/C5TA03680A.

(17) Cohen, S. M.; Zhang, Z.; Boissonnault, J. A. Toward "MetalloMOFzymes": Metal–Organic Frameworks with Single-Site Metal Catalysts for Small-Molecule Transformations. *Inorg. Chem.* **2016**, *55* (15), 7281–7290. https://doi.org/10.1021/acs.inorgchem.6b00828.

(18) Pascanu, V.; González Miera, G.; Inge, A. K.; Martín-Matute, B. Metal–Organic Frameworks as Catalysts for Organic Synthesis: A Critical Perspective. *J. Am. Chem. Soc.* **2019**, *141* (18), 7223–7234. https://doi.org/10.1021/jacs.9b00733.

(19) Sheberla, D.; Bachman, J. C.; Elias, J. S.; Sun, C.-J.; Shao-Horn, Y.; Dincă, M. Conductive MOF Electrodes for Stable Supercapacitors with High Areal Capacitance. *Nat. Mater.* **2017**, *16* (2), 220–224. https://doi.org/10.1038/nmat4766.

(20) Feng, D.; Lei, T.; Lukatskaya, M. R.; Park, J.; Huang, Z.; Lee, M.; Shaw, L.; Chen, S.; Yakovenko, A. A.; Kulkarni, A.; Xiao, J.; Fredrickson, K.; Tok, J. B.; Zou, X.; Cui, Y.; Bao, Z. Robust and Conductive Two-Dimensional Metal−organic Frameworks with

Exceptionally High Volumetric and Areal Capacitance. *Nat. Energy* **2018**, *3* (1), 30–36. https://doi.org/10.1038/s41560-017-0044-5.

(21) Park, J.; Lee, M.; Feng, D.; Huang, Z.; Hinckley, A. C.; Yakovenko, A.; Zou, X.; Cui, Y.; Bao, Z. Stabilization of Hexaaminobenzene in a 2D Conductive Metal–Organic Framework for High Power Sodium Storage. *J. Am. Chem. Soc.* **2018**, *140* (32), 10315–10323. https://doi.org/10.1021/jacs.8b06020.

(22) Zhu, J. P.; Wang, X. H.; Zuo, X. X. The Application of Metal-Organic Frameworks in Electrode Materials for Lithium–Ion and Lithium–Sulfur Batteries. *R. Soc. Open Sci.* **2019**, *6* (7), 190634. https://doi.org/10.1098/rsos.190634.

(23) Shinde, S. S.; Lee, C. H.; Jung, J.-Y.; Wagh, N. K.; Kim, S.-H.; Kim, D.-H.; Lin, C.; Lee, S. U.; Lee, J.-H. Unveiling Dual-Linkage 3D Hexaiminobenzene Metal–Organic Frameworks towards Long-Lasting Advanced Reversible Zn–Air Batteries. *Energy Environ. Sci.* **2019**, *12* (2), 727–738. https://doi.org/10.1039/C8EE02679C.

(24) Jiang, Q.; Xiong, P.; Liu, J.; Xie, Z.; Wang, Q.; Yang, X.-Q.; Hu, E.; Cao, Y.; Sun, J.; Xu, Y.; Chen, L. A Redox-Active 2D Metal–Organic Framework for Efficient Lithium Storage with Extraordinary High Capacity. *Angew. Chem. Int. Ed.* **2020**, *59* (13), 5273–5277. https://doi.org/10.1002/anie.201914395.

(25) Zhang, L.; Cui, P.; Yang, H.; Chen, J.; Xiao, F.; Guo, Y.; Liu, Y.; Zhang, W.; Huo, F.; Liu, B. Metal–Organic Frameworks as Promising Photosensitizers for Photoelectrochemical Water Splitting. *Adv. Sci.* **2016**, *3* (1), 1500243. https://doi.org/10.1002/advs.201500243.

(26) Dong, R.; Zheng, Z.; Tranca, D. C.; Zhang, J.; Chandrasekhar, N.; Liu, S.; Zhuang, X.; Seifert, G.; Feng, X. Immobilizing Molecular Metal Dithiolene–Diamine Complexes

on 2D Metal–Organic Frameworks for Electrocatalytic H2 Production. *Chem. – Eur. J.* **2017**, *23* (10), 2255–2260. https://doi.org/10.1002/chem.201605337.

(27) Liu, M.; Zheng, W.; Ran, S.; Boles, S. T.; Lee, L. Y. S. Overall Water-Splitting Electrocatalysts Based on 2D CoNi-Metal-Organic Frameworks and Its Derivative. *Adv. Mater. Interfaces* **2018**, *5* (21), 1800849. https://doi.org/10.1002/admi.201800849.

(28) Downes, C. A.; Clough, A. J.; Chen, K.; Yoo, J. W.; Marinescu, S. C. Evaluation of the H_2 Evolving Activity of Benzenehexathiolate Coordination Frameworks and the Effect of Film Thickness on H_2 Production. *ACS Appl. Mater. Interfaces* **2018**, *10* (2), 1719–1727. https://doi.org/10.1021/acsami.7b15969.

(29) Ali, M.; Pervaiz, E.; Noor, T.; Rabi, O.; Zahra, R.; Yang, M. Recent Advancements in MOF-Based Catalysts for Applications in Electrochemical and Photoelectrochemical Water Splitting: A Review. *Int. J. Energy Res.* **2021**, *45* (2), 1190–1226. https://doi.org/10.1002/er.5807.

(30) Smith, M. K.; Mirica, K. A. Self-Organized Frameworks on Textiles (SOFT): Conductive Fabrics for Simultaneous Sensing, Capture, and Filtration of Gases. *J. Am. Chem. Soc.* **2017**, *139* (46), 16759–16767. https://doi.org/10.1021/jacs.7b08840.

(31) Rubio-Giménez, V.; Almora-Barrios, N.; Escorcia-Ariza, G.; Galbiati, M.; Sessolo, M.; Tatay, S.; Martí-Gastaldo, C. Origin of the Chemiresistive Response of Ultrathin Films of Conductive Metal–Organic Frameworks. *Angew. Chem. Int. Ed.* **2018**, *57* (46), 15086–15090. https://doi.org/10.1002/anie.201808242.

(32) Aubrey, M. L.; Kapelewski, M. T.; Melville, J. F.; Oktawiec, J.; Presti, D.; Gagliardi, L.; Long, J. R. Chemiresistive Detection of Gaseous Hydrocarbons and

Interrogation of Charge Transport in Cu[Ni(2,3-Pyrazinedithiolate) $_2$] by Gas Adsorption. *J. Am. Chem. Soc.* **2019**, *141* (12), 5005–5013. https://doi.org/10.1021/jacs.9b00654.

(33) Leelasree, T.; Selamneni, V.; Akshaya, T.; Sahatiya, P.; Aggarwal, H. MOF Based Flexible, Low-Cost Chemiresistive Device as a Respiration Sensor for Sleep Apnea Diagnosis. *J. Mater. Chem. B* **2020**, *8* (44), 10182–10189. https://doi.org/10.1039/D0TB01748E.

(34) Xie, L.; Skorupskii, G.; Dinca, M. Electrically Conductive Metal-Organic Frameworks. *Chemical Reviews* **2020,** 120 (16), 8536-8580 DOI: 10.1021/acs.chemrev.9b00766.

(35) Kobayashi, Y.; Jacobs, B.; Allendorf, M. D.; Long, J. R. Conductivity, Doping, and Redox Chemistry of a Microporous Dithiolene-Based Metal−Organic Framework. *Chem. Mater.* **2010**, *22* (14), 4120–4122. https://doi.org/10.1021/cm101238m.

(36) Hao, Z.; Yang, G.; Song, X.; Zhu, M.; Meng, X.; Zhao, S.; Song, S.; Zhang, H. A Europium(III) Based Metal–Organic Framework: Bifunctional Properties Related to Sensing and Electronic Conductivity. *J Mater Chem A* **2014**, *2* (1), 237–244. https://doi.org/10.1039/C3TA13179C.

(37) Marshall, R. J.; Griffin, S. L.; Wilson, C.; Forgan, R. S. Single-Crystal to Single-Crystal Mechanical Contraction of Metal–Organic Frameworks through Stereoselective Postsynthetic Bromination. *J. Am. Chem. Soc.* **2015**, *137* (30), 9527–9530. https://doi.org/10.1021/jacs.5b05434.

(38) Li, G.-P.; Zhang, K.; Zhao, H.-Y.; Hou, L.; Wang, Y.-Y. Increased Electric Conductivity upon I2 Uptake and Gas Sorption in a Pillar-Layered Metal–Organic

Framework. *ChemPlusChem* **2017**, *82* (5), 716–720. https://doi.org/10.1002/cplu.201700063.

(39) Zhang, X.; da Silva, I.; Fazzi, R.; Sheveleva, A. M.; Han, X.; Spencer, B. F.; Sapchenko, S. A.; Tuna, F.; McInnes, E. J. L.; Li, M.; Yang, S.; Schröder, M. Iodine Adsorption in a Redox-Active Metal–Organic Framework: Electrical Conductivity Induced by Host−Guest Charge-Transfer. *Inorg. Chem.* **2019**, *58* (20), 14145–14150. https://doi.org/10.1021/acs.inorgchem.9b02176.

(40) Yin, Z.; Wang, Q.-X.; Zeng, M.-H. Iodine Release and Recovery, Influence of Polyiodide Anions on Electrical Conductivity and Nonlinear Optical Activity in an Interdigitated and Interpenetrated Bipillared-Bilayer Metal–Organic Framework. *J. Am. Chem. Soc.* **2012**, *134* (10), 4857–4863. https://doi.org/10.1021/ja211381e.

(41) Hu, Y.-Q.; Li, M.-Q.; Wang, Y.; Zhang, T.; Liao, P.-Q.; Zheng, Z.; Chen, X.-M.; Zheng, Y.-Z. Direct Observation of Confined I−···I2···I− Interactions in a Metal–Organic Framework: Iodine Capture and Sensing. *Chem. – Eur. J.* **2017**, *23* (35), 8409–8413. https://doi.org/10.1002/chem.201702087.

(42) Takaishi, S.; Hosoda, M.; Kajiwara, T.; Miyasaka, H.; Yamashita, M.; Nakanishi, Y.; Kitagawa, Y.; Yamaguchi, K.; Kobayashi, A.; Kitagawa, H. Electroconductive Porous Coordination Polymer $Cu[Cu(pdt)_2]$ Composed of Donor and Acceptor Building Units. *Inorganic Chemistry* **2009,** 48 (19), 9048-9050 DOI: 10.1021/ic802117q.

(43) Peng, Y.; Pham, T.; Li, P.; Wang, T.; Chen, Y.; Chen, K.; Forrest, K.; Space, B.; Cheng, P.; Zaworotko, M.; et al. Robust Ultramicroporous Metal-Organic Frameworks with Benchmark Affinity for Acetylene. *Angew. Chem. Int. Ed*. **2018**, 57, 10971-10975, DOI: 10.1002/anie.201806732.

(44) Le Bail, A. ; Duroy, H. ; Fourquet, J. L. Ab Initio Structure Determination of LiSbWO6 by X ray Powder Diffraction, *Mater. Res. Bull.* **1998**, *23*, 447-452.

(45) Ribas, X.; Dias, J.; Morgado, J.; Wurst, K.; Molins, E.; Ruiz, E.; Almeida, M.; Veciana, J.; Rovira, C. Novel Cu-III bis-1,2-dichalcogenene complexes with tunable 3D framework through alkaline cation coordination: A structural and theoretical study. *Chemistry-a European Journal* **2004,** 10 (7), 1691-1704 DOI: 10.1002/chem.200305422.

(46) Vanýsek, Petr (2020). "Electrochemical Series". CRC handbook of chemistry and physics : a ready-reference book of chemical and physical data 101st edition, Rumble, J. R. Jr.; Bruno, T. J; Doa M. J. ed. CRC Press. pp. 5–100.

(47) Burns, G.; Renner, R. A Raman and resonance Raman-study of polybromide anions and a study of the temperature-dependence of the Raman-active phonons of tetrabutylammonium tribromide. *Spectrochimica Acta Part a-Molecular and Biomolecular Spectroscopy* **1991**, *47* (8), 991-999, Article. DOI: 10.1016/0584-8539(91)80030-M.

(48) Branigan, E.; Halberstadt, N.; Apkarian, V. Solvation dynamics through Raman spectroscopy: Hydration of Br-2 and Br-3(-), and solvation of Br-2 in liquid bromine. *Journal of Chemical Physics* **2011**, *134*, 174503, Article. DOI: 10.1063/1.3583477.

(49) Robin, M. B.; Day, P. Mixed Valence Chemistry: A Survey and Classification, *Adv. Inorg. Radiochem*. **1967**, *10*, 247-422.

(50) Ito, T.; Watanabe, M.; Yamamoto, K.; Ikeda, N.; Nogami, Y.; Noda, Y.; Mori, H.; Mori, T.; Terasaki, I. Temperature and electric-current dependence of charge-ordered domains in theta-$(BEDT\text{-}TTF)_2CsZn(SCN)_4$. *Europhysics Letters,* **2008,** 84, 26002.

(51) Littlewood, P. BISTABILITY OF NON-LINEAR CONDUCTIVITY IN INSULATORS WITH SLIDING CHARGE-DENSITY WAVES. *Solid State Communications* **1988,** 65 (11), 1347-1350 DOI: 10.1016/0038-1098(88)90090-7.

(52) Yoon, S.; Talin, A. A.; Stavila, V.; Mroz, A. M.; Bennett, T. D.; He, Y.; Keen, D. A.; Hendon, C. H.; Allendorf, M. D.; So, M. C. From N- to p-Type Material: Effect of Metal Ion on Charge Transport in Metal–Organic Materials. *ACS Appl. Mater. Interfaces* **2021**, 13, 52055-52062.

(53) Hinckley, A. C.; Park, J.; Gomes, J.; Carlson, E.; Bao, Z. Air-Stability and Carrier Type in Conductive M $_3$ (Hexaaminobenzene) $_2$, (M = Co, Ni, Cu). *J. Am. Chem. Soc.* **2020**, *142* (25), 11123–11130. https://doi.org/10.1021/jacs.0c03500.

(54) Syrotyuk, S. V.; Klysko, Yu. V. Hybrid functional analysis of porous coordination polymers Cu[Cu(pdt)$_2$] and Cu[Ni(pdt)$_2$], Cond. Mat. Phys., 2020, 23, 33703. DOI:10.5488/CMP.23.33703.

(55) Watanabe, S.; Ohno, M.; Yamashita, Y.; Terashige, T.; Okamoto, H.; Takeya, J. Validity of the Mott formula and the origin of thermopower in pi-conjugated semicrystalline polymers. *Physical Review B* **2019,** 100 (24), 241201. DOI: 10.1103/PhysRevB.100.241201.

Chapter-3

Quinoid-Based Three-Dimensional Metal-Organic Framework, $Fe_2(dhbq)_3$: Porosity, Electrical Conductivity and Solid-State Redox Property

3.1 Chapter Introduction

Coordination polymers of 2,5- dihydroxy-1,4- benzoquinone and its derivative has been immense out as a new interesting material because of its appealing feature to acquire variable oxidation state[1] and having the same energy level to that of the binding atom especially early transition metals. In recent years, redox active MOFs seems very helpful in order to enhance the electronic conductivity. Incorporation of redox active centers can cause a presence of mixed valence state by means of doping with some electroactive material which can enhance the conductivity. Moreover, effective frontier orbital overlapping and similar energy level of binding atoms can cause long range d-π conjugation. And hence current focus of research is exploring materials whose conductivity can be modulated upon tuning its redox state. $(NBu_4)_2Fe^{III}_2(dhbq)_3$ MOF reported by Long and co-workers, consist of Fe^{III} and $dhbq^{2-/3-}$ was one of the most conductive MOFs.[2] The intrinsic conductivity (0.16 S cm^{-1}) of MOF was a result of ligand based intervalence charge transfer due to the presence of mixed valence $dhbq^{2-/3-}$. Another $[(Me_2NH_2)_2Fe^{III}_2(Cl_2dhbq)_3]\cdot 2H_2O\cdot 6DMF$ two-dimensional MOF investigated by Harris and co-workers reported that upon chemical reduction using Cp_2Co results in a 10^2 fold decrement of the conductivity[3]. The significant reduction in conductivity is due to the absence of mixed valency upon reduction, since the reduction was based on ligand which was supported by spectral analysis. Owing to the manipulation of electronic state of ligand, long range magnetic interaction stems to magnetic ordering below 105 K upon complete reduction of ligand.

Redox activity of $dhbq^{n-}$ based ligands further provide the opportunity to explore the material as a low-density energy storage material. $[(Me_2NH_2)_2Fe^{III}_2(Cl_2\ dhbq)_3]$ was

further explored by Long and co-workers as a promising material for cathode performances in a Li-ion battery[4]. It was demonstrated that upon fabricating aforementioned material as a cathode, energy density up to 533 Wh / Kg was realized. Moreover, it also showed retention of capacity over 50 cycles, which is the highest among the MOF based cathode materials reported till now. Combined metal and ligand based redox activity, electrical conductivity and porosity came out to be the probable reasons for the extra ordinary performance of this MOF.

Considering the impact of lower molecular weight on the specific capacity, our group recently came out with 2,5-dihydroxy-1,4-benzoquinone based one dimensional [Fe(dhbq)] MOF having a molecular weight of 193.9.[5] Interestingly, it showed microporous structure upon desolvating and a 10^4 fold dramatic decrement of resistivity. Upon fabricating the MOF as a cathode material, exhibited specific capacity of 264 mAh / g during its first discharge process with an energy density of 556 Wh / Kg, which was even higher than $[(Me_2NH_2)_2Fe^{III}_2(Cl_2dhbq)_3]$. [Fe(dhbq)] exhibited a theoretical capacity of 276 mAh / g based on 2 e^- reversible redox behavior based on ligand. Metal based redox activity could have caused even more enhanced specific capacity. It is cleared from the aforementioned results that in order to enhance the specific capacity of a material two important factors needs to be consider, 1. Low density molecules which can be obtained by removing the possibility of cations. Larger cations usually occupy the pore of the MOF which also limits the further application of MOFs for further doping purpose. 2. Both the metal and ligands should possess redox activity.

3.2 Research objective and strategies

Plenty of reports are there based on MOF originated cathode materials which utilizes the redox active metal and ligand in order to achieve the better performance for lithium-ion storage. However, Lower electrical conductivity and lack of porosity limits the use of a MOF to be incorporated. [4,5] There have been several reports published based on $X_2dhbq^{2-/3-}$ ligands including 1D [5], 2D [3,6,7] coordination polymers. However, only few conducting 3D coordination polymers were reported and that too upon incorporating larger cations as a template.[2,8,9,10] Larger cations usually occupy the pore of the MOF and results in a non-porous polymer which limits its application towards lithium storage. Herein, we report synthesis, characterization and physical properties of three-dimensional neutral conducting MOF based on 2,5-dihydroxy-1,4-benzoquinone ligand without using any cation, formulated as $[Fe_2(dhbq)_3]$, having a molecular weight of 525.92. The MOF buildup of Fe(III) and $dhbq^{2-}$ ligand exhibit redox activity based on both metal and ligand with a theoretical capacity of 408 mAh / g. It showed relatively high electrical conductivity of 1.6×10^{-2} S cm^{-1} as a consequence of strong d-π conjugation which corresponds to the strong covalency between metal and ligand. Nitrogen adsorption illustrates that unlike the other reported benzoquinone derivatized three dimensional MOFs, it shows permanent porosity with a pore diameter of 0.46 nm. We further explore the redox activity and electrochemical behavior of $[Fe_2(dhbq)_3]$ and reported that it shows redox activity based on metal as well as ligand with a first discharge capacity of 322 mAh / g. Redox behavior of the Fe was evidenced by ex-situ XANES spectral analysis. Magnetic properties showed that the MOF showed antiferromagnetic coupling at lower temperature range.

3.3 Synthesis

3.3.1 Synthesis of H_4thb

Tetrahydroxy benzene (H_4thb) was prepared from dihydroxy benzoquinone (H_2dhbq). H_2dhbq (2.8 g, 20 mmol) was reduced using (4.0 g, 20 mmol) of $SnCl_2$ in 50ml conc HCl, taking small fraction at a time. Refluxed the solution at 80 ^oC for 3hr, color of the solution become off white. Filtered the colorless needle like crystals after cooling down the reaction mixture and washed with cold acetonitrile. Yield: 64 %.

3.3.2 Synthesis of $[Fe_2(dhbq)_3]\cdot nH_2O$ slow diffusion

In a 100 ml vial, a solution of $FeSO_4.7H_2O$ (140 mg, 0.5 mmol) in 20 ml of deionized water was sparged with N_2 for 15 min. 80 ml of Methanol was added to the solution and again sparged N_2 for 15min. At last, H_4thb (120mg, 0.85 mmol) was added to the above solution and sealed with paraffin paper with some holes on it. The reaction mixture was kept at room temperature for several days. The resulting black shiny solid was filtered off and washed with MeOH. Black crystals suitable for Single-crystal structural analysis were obtained. Yield : 43 %.

3.3.3 Synthesis of $[Fe_2(dhbq)_3]\cdot nH_2O$ rt

In a round bottom flask, a solution of $Fe_2(SO_4)_3\cdot nH_2O$ (908mg, 2 mmol) in 30ml of deionized water was taken. On the other hand, H_2dhbq (420 mg, 3 mmol) was dissolved in 30 ml of deionized water separately. Both the solutions were mixed and stirred overnight at rt. Black solid with a little reddish tint was filtered off and washed with water. Characterization and phase purity was performed using PXRD and CHN analysis. Yield:

87%. Elemental analysis: Found C: 37.886, H: 1.810 (Calc. C: 37.63, H: 2.00 for $[Fe_2(dhbq)_3]\cdot 2.7H_2O$).

3.4 Characterization

3.4.1 Crystal description of $[Fe_2(dhbq)_3]\cdot nH_2O$

Single crystal X-ray analysis reveals, unlike previously reported $[(NBu_4)_2Fe^{III}_2(dhbq)_3]$ and $[(NBu_4)_2Fe^{III}_2(fan)_3]$ (fan = floranilate) MOFs which utilizes tetra butylammonium cation as a template to build a 3-D network[43,47], it's a neutral $[Fe_2(dhbq)_3]$ 3D MOF with no cation associated with it. Most of the transition metals upon associating with $dhbq^{2-}$ derivative ligand acquires one- or two-dimensional coordination polymer. Using $dhbq^{-2}$ derivative ligands few 3-D MOFs were reported but they are not purely metal and ligand based but also incorporate some cations. $[Fe_2(dhbq)_3]$ crystalizes in *Fddd* space group. Each Fe center octahedrally coordinated with 6 O atom from three different deprotonated $dhbq^{2-}$ligands. With a total of 1.5 $dhbq^{-2}$ per Fe atom leading to a three-dimensional network (**Figure 3.4.1).** The Fe-O and C-O bond lengths were determined to be in the range of 1.995-2.026 and 1.267-1.288 Å respectively. Which are even shorter than Fe-O (2.008, 2.031) and C-O (1.281, 1.308) observed in $[(NBu_4)_2Fe^{III}_2(dhbq)_3]$.[43] which was an early indication of the presence of Fe^{III} (high spin) and $dhbq^{2-}$. The magnetic susceptibility of Fe_2dhbq_3 was consistent with Fe^{III} high spin state. **Figure 3.4.3** shows one dimensional pore channel along a- axis.

Detailed crystal analysis reveals that there are three interpenetrated structures were present. All the three structures are similar to each other. Slight difference in bond lengths were

observed. We concluded that three different iron centers were present which belongs to each interpenetrated structure. However, four kinds of ligands were identified depending on the bond length they shared with iron. Other than that, we also tried to find the Topology and network of the crystal using Topospro software. Upon simplifying the structure as shown in **Figure 3.4.2**, it was concluded three nodes were present in which the node with 3-c coordination mode is a representation of metal centers and one node with 2-c coordination mode is a representation of ligands.

No any solvent molecules were detected crystallographically inside the pores. However, this MOF have the capacity to adsorb water molecules, which was confirmed from the TGA and elemental analysis. Two adsorption isotherms, 77K N_2 and 77K H_2, were investigated after activating the sample to 150^{o}C under vacuum for overnight both the measurements further confirm the presence of microporous structure.

a)

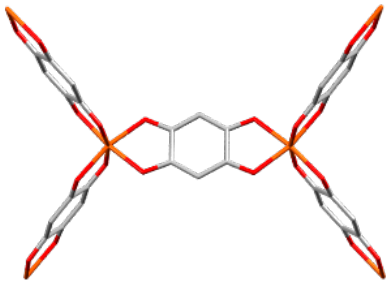

b)

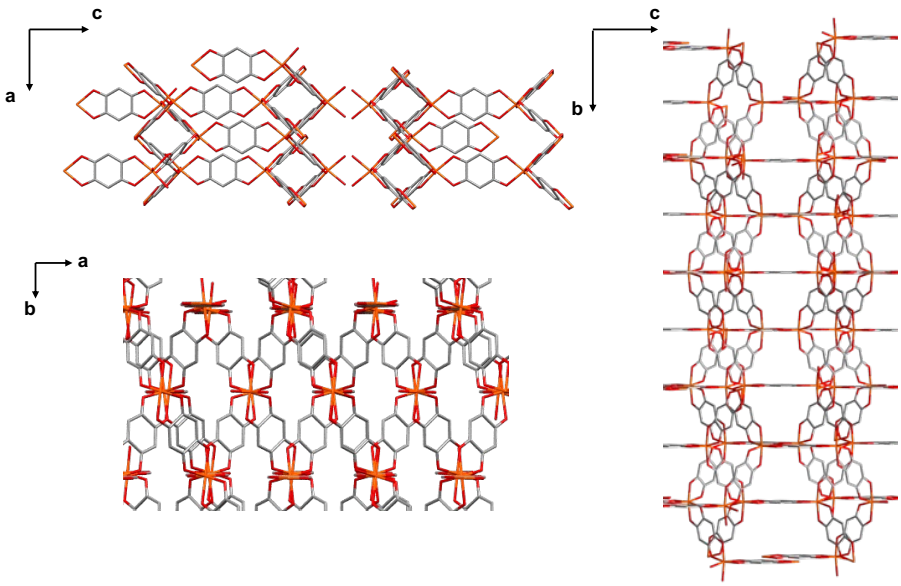

c)

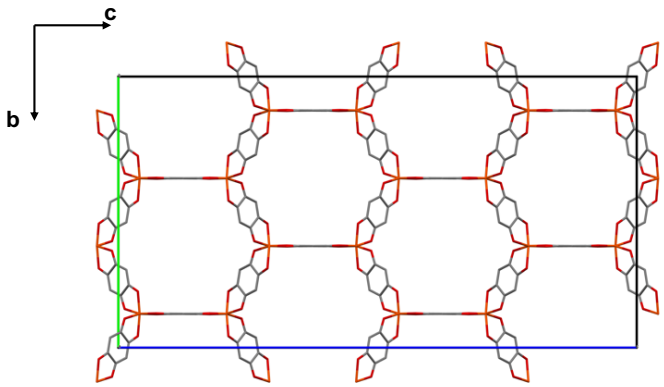

Figure 3.4.1 Crystal structure of $[Fe_2(dhbq)_3]$. **(a)** Coordination environment of iron **(b)** View from different crystallographic axis **(c)** one of the three interpenetrated structures.

a)

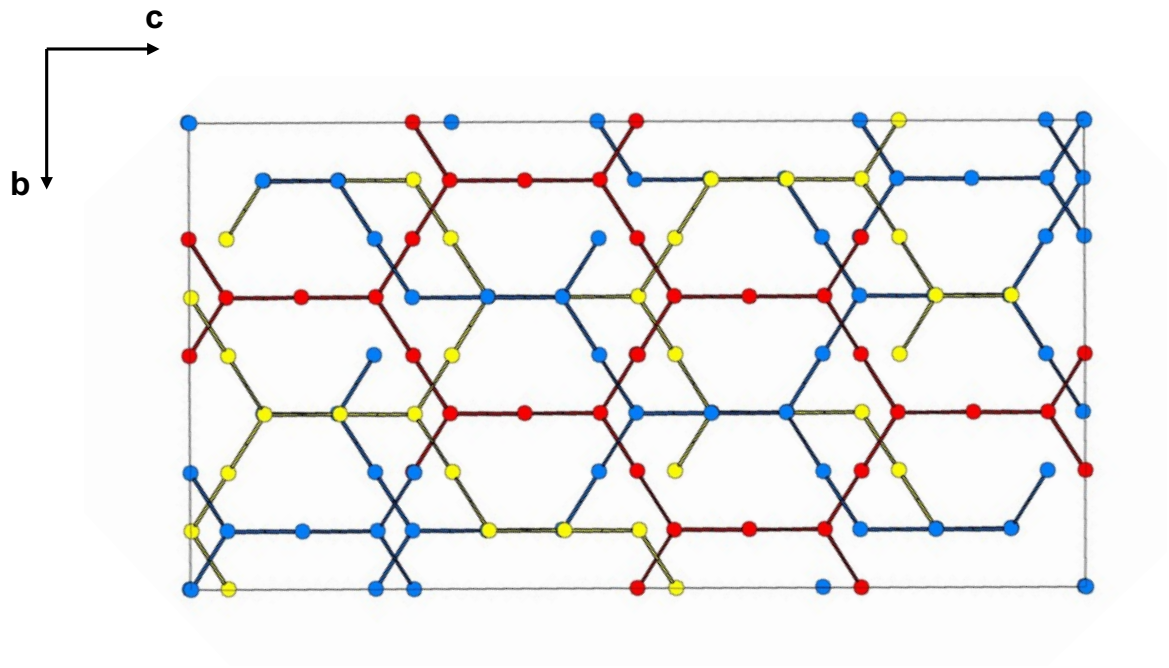

b)

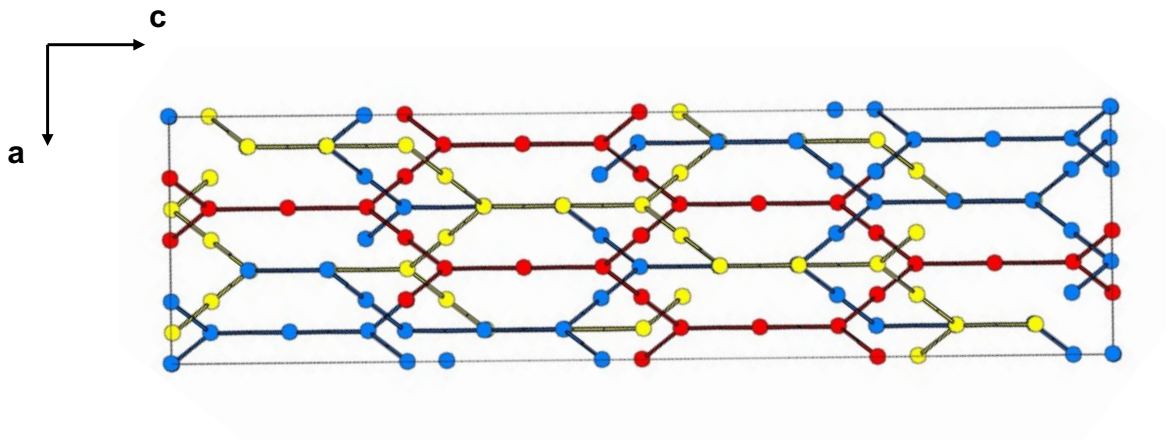

Figure 3.4.2 Network representation of $[Fe_2(dhbq)_3]$.

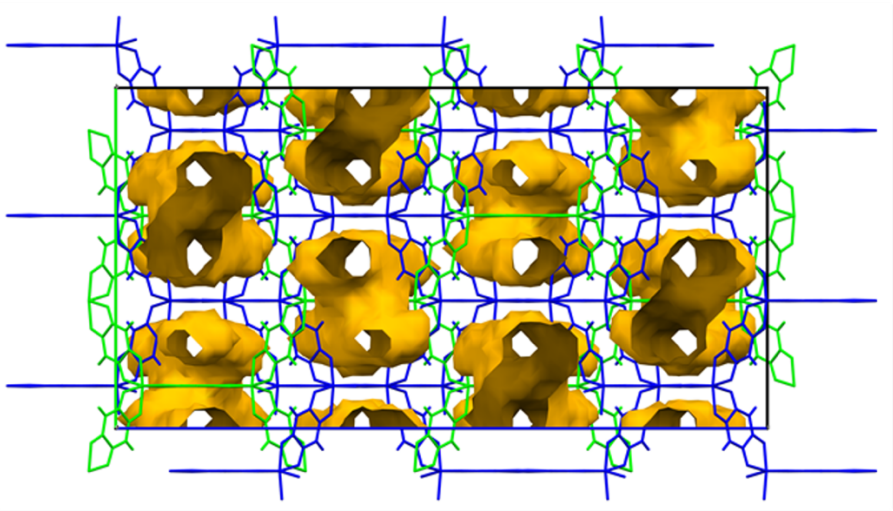

Figure 3.4.3 Network representation of [$Fe_2(dhbq)_3$].

3.4.4 PXRD data

Fe_2dhbq_3 rt was characterized by PXRD. **Figure 3.4.4** shows that Fe_2dhbq_3 rt has same PXRD pattern to that of the simulated data.

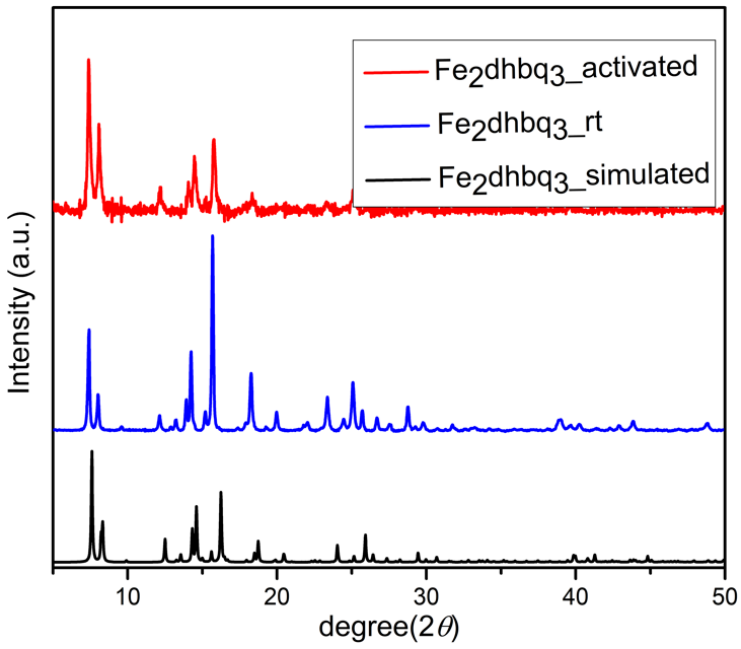

Figure 3.4.4 Simulated X-ray powder diffraction pattern for Fe_2dhbq_3 and X-ray powder diffraction pattern for Fe_2dhbq_3rt before (blue line) and after activation (red line).

3.5 Thermal stability

To investigate the thermal stability and water content inside the MOFs, thermogravimetric measurements was performed upon activating the samples to 140 ^{o}C for 24 hr under reduced pressure. While looking at **Figure 3.5.1**, no well-developed plateau but a continuous weight loss near 400 ^{o}C can be seen which might corresponds to decomposition of MOF. However, the crystallinity of the sample was maintained up to 200 ^{o}C activation with slight broadening of peaks as shown in **Figure 3.5.2**. On the other hand, result of CHN analysis confirms the presence of 2.7 H_2O molecules after activating sample to 140 ^{o}C. Which implies that subsequent activation was not sufficient for complete desolvation.

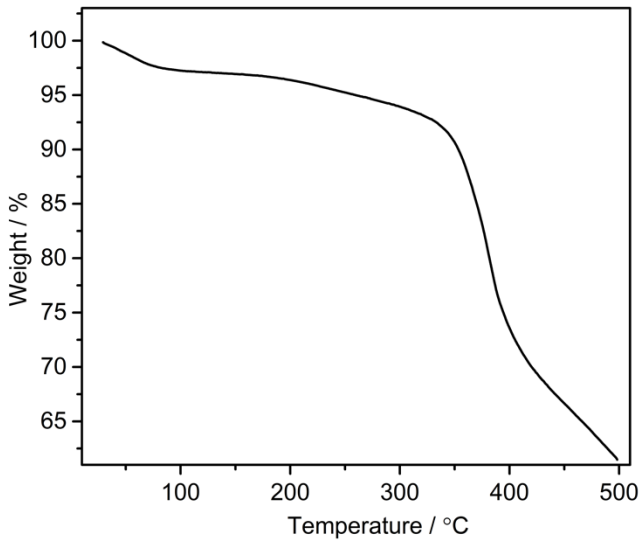

Figure 3.5.1 Thermogravimetric analysis of $[Fe_2(dhbq)_3]$.

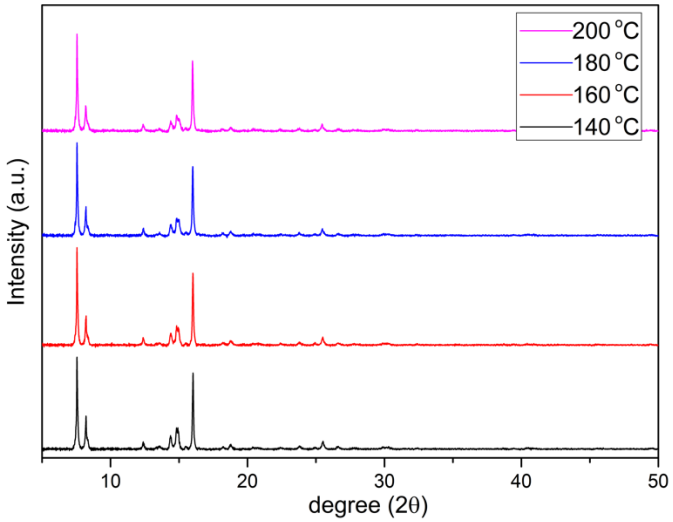

Figure 3.5.2 Variable temperature X-ray powder diffraction pattern for Fe_2dhbq_3.

3.6 BET surface

Surface area of the MOF was investigated using N_2 adsorption isotherm. The measurement was performed at 77K in liquid N_2. In **Figure 3.6.1a** it shows type-I adsorption isotherm having a Langmuir surface area of 556 $m^2 g^{-1}$, which clearly confirms that it possesses permanent micropores structure. This value is highest reported for any 3-D MOF based on $dhbq^{2-}$derivatized ligand. Although it has relatively small pore size of 0.46 nm calculated using Horvath - Kawazoe model (**Figure 3.6.1b**). Both surface area and pore size were almost compared to [Fe(dhbq)] MOF reported by our group.[5] We also perform hydrogen sorption measurement as shown in **Figure 3.6.2**. Hydrogen sorption measurement also showed type- I adsorption. And the amount of adsorbed hydrogen was nearly same to that of the nitrogen amount of hydrogen.

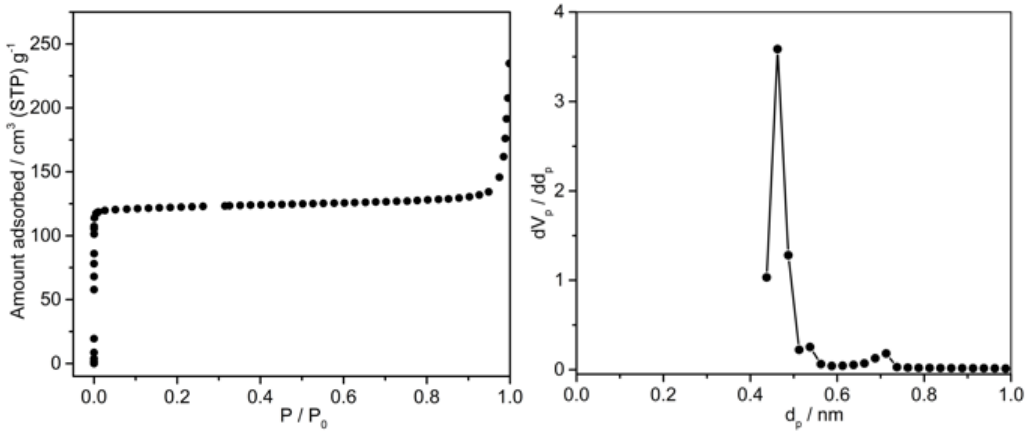

Figure 3.6.1 (a) N_2 isotherm **(b)** pore size distribution (Horvaťh− Kawazoe plot) for $[Fe_2(dhbq)_3]$ at 77 K.

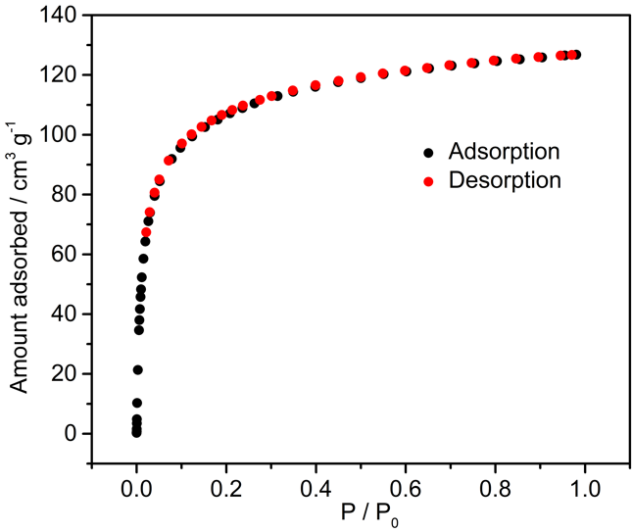

Figure 3.6.2 77-K H_2 adsorption isotherm of Fe_2dhbq_3rt confirming microporosity. Adsorption isotherm was measured after activating sample under vacuum at 140 °C overnight.

3.7 Optical properties

3.7.1 Infrared Spectroscopy

FTIR spectra was also obtained using KBr pellet to probe if there is any charge transfer band was observed (**Figure 3.7.1)**. In case of $dhbq^{2-}$ based MOF, FTIR spectra proofs helpful to understand if the ligand possesses localized electronic structure or delocalized. Consistent with the previously reported $dhbq^{2-}$ based MOFs the symmetrical vibration stretching frequency was observed at 1489 cm^{-1} as shown in **Figure 3.7.1** which can be assigned to $\nu_{C=O}$ ($dhbq^{2-}$) because complexes containing $dhbq^{3-}$radical anion crucially show C=O stretching frequency in the range of 1460-14300.[1,11,12] Multiple sharp and intense peaks is consistent with the fact that both localized and delocalized quinoid bridge were present in the compound.[13] We assigned peaks at 1489 and 1342cm^{-1} were corresponding to the localized and partially delocalized C=O stretching respectively. Ex situ IR **Figure 3.13.1** spectra unveil the disappearance of aforementioned peaks upon electrochemical reduction which verifies the assignments. Also, a flat band in NIR region indicates absence of intervalence charge transfer (IVCT) which further support the fact that no mixed valence was found in the compound.

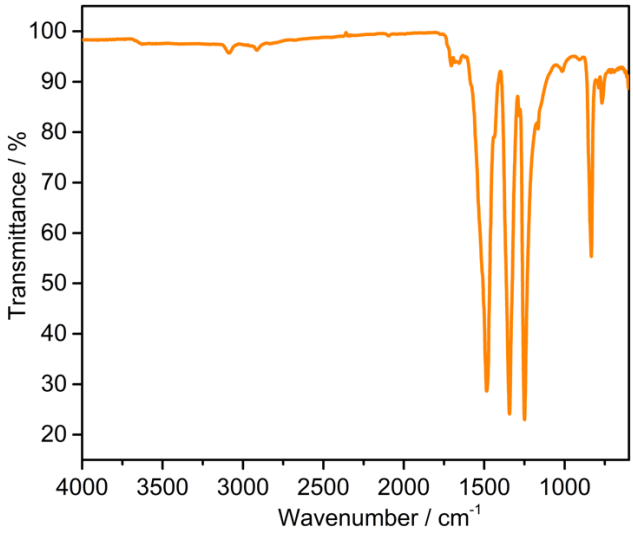

Figure 3.7.1 FTIR spectra of $[Fe_2(dhbq)_3]$ using KBr pellet.

3.7.2 UV-Vis -NIR Spectroscopy

UV-vis-NIR diffuse reflectivity spectra were collected on Shimadzu UV-3100PC spectrometer attached with Shimadzu ISR-3100 integrating sphere. $BaSO_4$ was used as a non-absorbing matrix to dilute the sample. Obtained diffuse reflectivity spectra were converted into absorption spectra by applying Kubelka-Munk function $F(R) = (1-R)^2/2R$. The solid-state UV-vis-NIR spectrum illustrate a narrow and not so intense band in NIR region as shown in **Figure 3.7.2**, another strong feature was observed at 17000 cm^{-1} which was assigned to be a ligand-based π to π* transitions. Since an intense and broad absorbance band in the NIR region has been the fingerprint for the intervalence charge transfer in the mixed valence materials.[14] Although a band was observed in the NIR region but the intensity was not so high. The absence of intense absorption band in NIR further support the claim that no mixed valency exists and the electronic state of $dhbq^{2-}$.

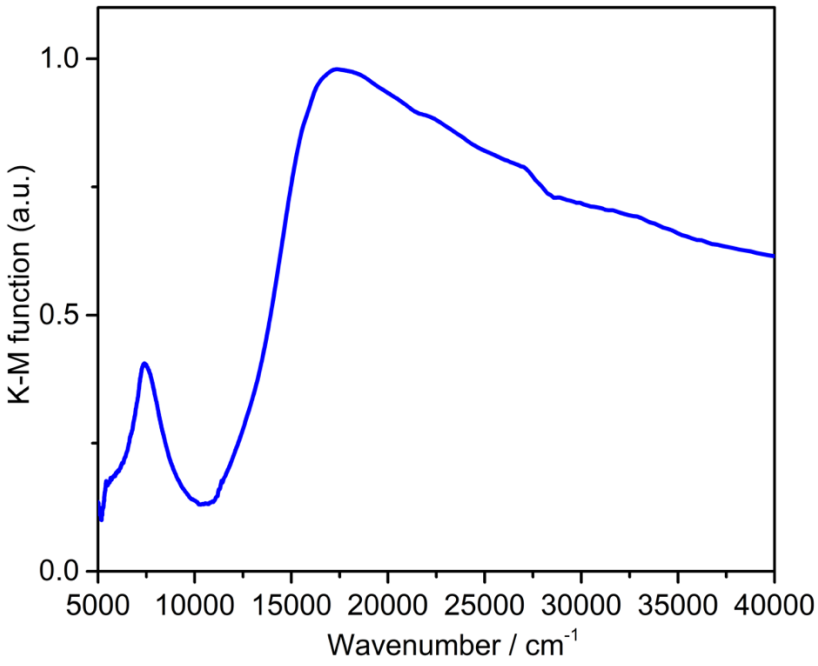

Figure 3.7.2 Diffuse reflectance spectra of $[Fe_2(dhbq)_3]$ using KBr pellet.

3.8 XANES spectra

Further confirmation of Fe(III) high spin was probed by X-ray absorption near-edge structure (XANES) at the Fe K edge of $[Fe_2(dhbq)_3]$. XANE spectra of $[Fe^{II}(dhbq)]\cdot 2H_2O$, a 1D coordination polymer reported by our group, along with $Fe^{III}(acac)_3$ were used as a reference.[5] $[Fe^{II}(dhbq)]\cdot 2H_2O$ have Fe centers in purely +2 oxidation state. As shown in the **Figure 3.8** it can clearly be seen that the absorption edge of $[Fe_2(dhbq)_3]$ corresponds to an energy value higher than that of $[Fe^{II}(dhbq)]\cdot 2H_2O$. Moreover, absorption edge energy of $Fe^{III}(acac)_3$ was found to be very close to $[Fe_2(dhbq)_3]$ Which is a clear indication that the oxidation state of iron center is +3. Furthermore, low intensity of 1s to 3d pre-edge peak verifies the octahedral geometry around the Fe center. Low intensity is a consequence of forbidden transition in the complexes having inversion symmetry.[15]

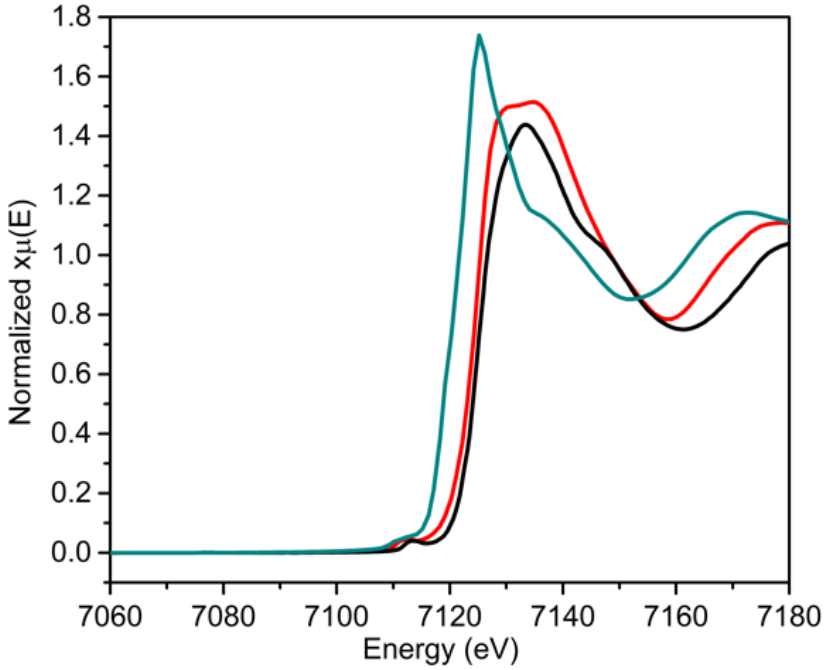

Figure 3.8 Normalized XANES spectra of $[Fe_2(dhbq)_3]$ (black line). Cyan and red lines in the graph indicates XANES of $[Fe^{II}(dhbq)]\cdot 2H_2O$ and $Fe^{III}(acac)_3$ as a reference.

3.9 Electrical conductivity

Temperature dependent behavior of electrical conductivity was measured on a quantum design using a two-probe method using pressed pellet at an applied temperature ranging from 160 to 300 K. **Figure 3.9.1 a** show the dependency of electrical conductivity on temperature which confirms the semiconductive behavior of MOF with an electrical conductivity of 1.2×10^{-2} S cm^{-1} at 300 K. **Figure 3.9.1 b** shows the Arrhenius plot of the conductivity data and calculated activation energy is found to be 212 meV. Unlike the redox hoping between radical organic ligands, responsible for the electrical conductivity found in the other $dhbq^{n-}$ derivative Fe based MOFs, This MOF showed conductivity entirely depend on long range d-π conjugation as a result of strong covalency between metal and ligand.

a)

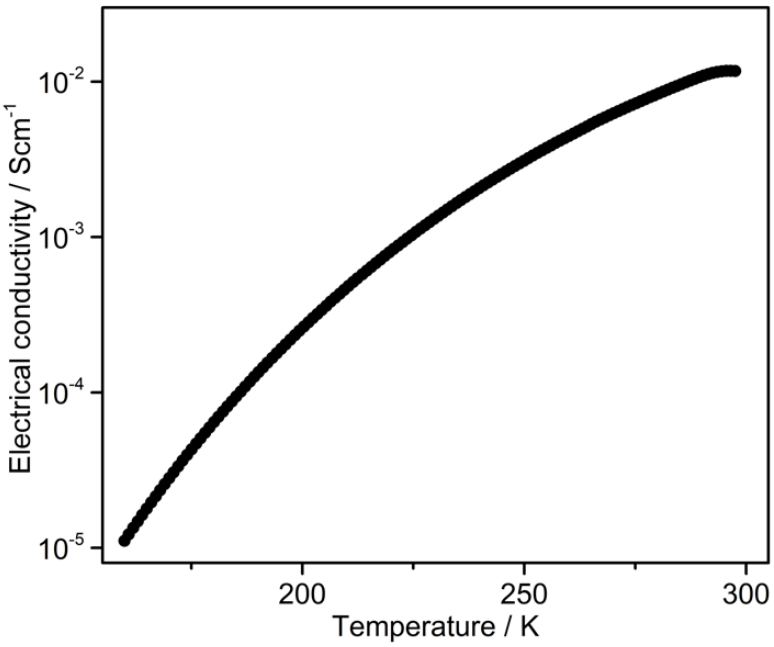

b)

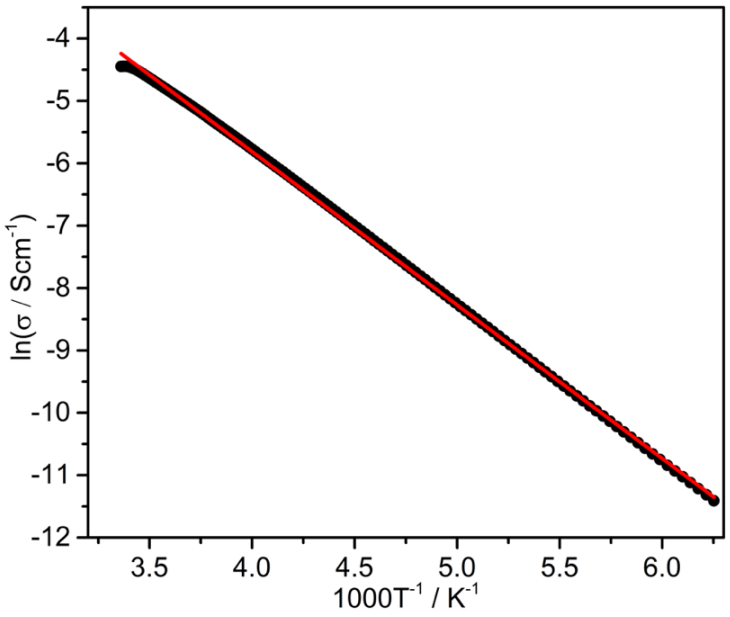

Figure 3.9.1 (a) Variable temperature conductivity data in the range of 160 to 300K **(b)** Arrhenius plot of the electrical conductivity of [Fe_2dhbq_3]. The red line represents the fitted line by the Arrhenius model.

3.9.2 Current (*I*)/ Voltage (*V*) characteristics

The room temperature electrical conductivity was investigated with the help of current(*I*) - voltage (*V*) characteristic using a pressed pellet of surface area 0.07 cm^2 and length 0.06cm **(Figure 3.9.2 a)**. The slope of this plot gives the resistance of the sample. The I-V plot was then converted to current density(J) vs electric field(E) as shown in **Figure 3.9.2 b**. The slope of the J-E characteristic gives the electrical conductivity at room temperature. The conductivity was estimated to 1.6×10^{-3} S cm^{-1} from J-E plot. One order lower conductivity in the case of I-V measurement could probably be due to the grain boundary effect.

a)

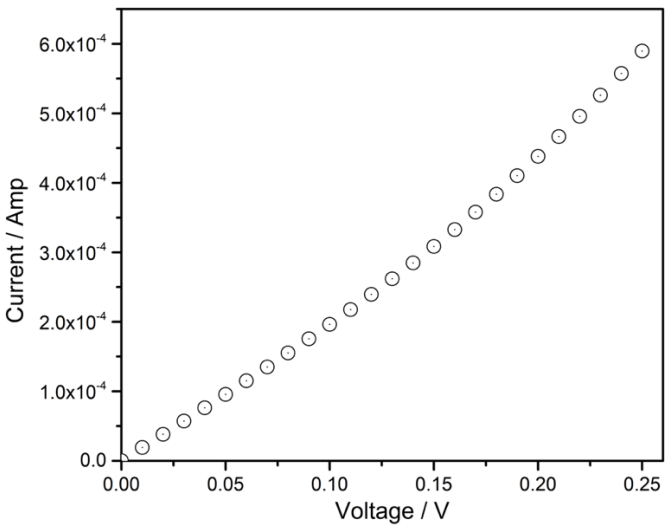

b)

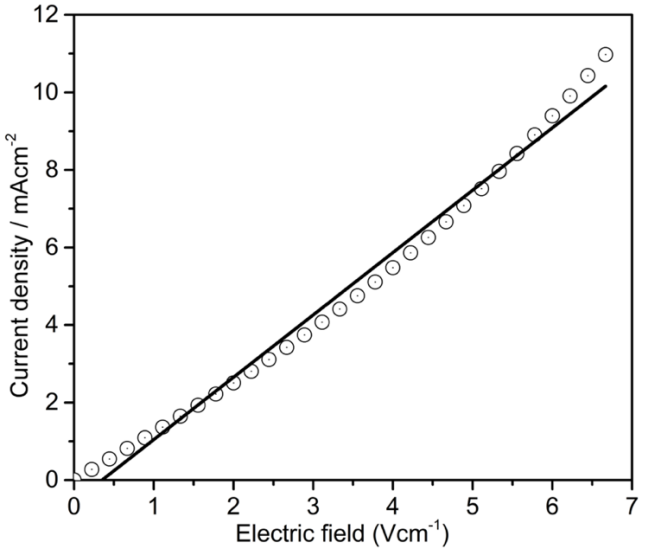

Figure 3.9.2 (a) *I-V* characterstic collected on Fe_2dhbq_3 rt at 300K showing Ohmic response between 0 to 25 mV. **(b)** *J-E* Characteristic.

3.10 Thermoelectromotive Force

We investigated the charge carrier type using thermoelectromotive force measurement. **(Figure 3.10)**. shows a plot ΔV vs ΔT of Fe_2dhbq_3. Negative of the slope of the plot gives the value of Seebeck coefficient. Fe_2dhbq_3 exhibited a Seebeck coefficient of -370 μVK^{-1} , negative sign of the Seebeck coefficient implies that it's a n-type semiconductor with electrons as a majority of charge carriers.

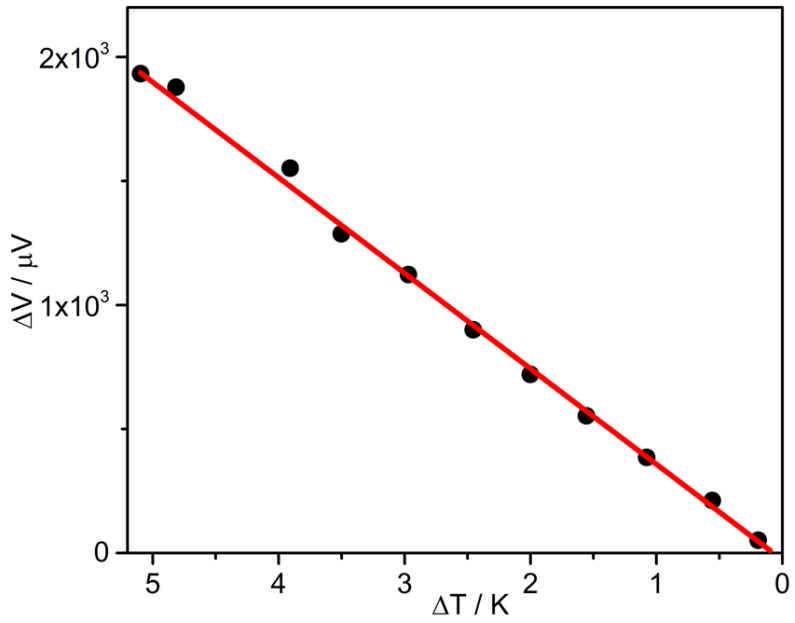

Figure 3.10 Thermoelectromotive force of Fe_2dhbq_3 rt.

3.11 Magnetic data

To investigate the magnetic behavior of $[Fe_2(dhbq)_3]$, variable- temperature dc magnetic susceptibility data were collected, and the resulting plots of $\chi_M T$ and χ_M vs T are shown in **Figure 3.11.1**. $\chi_M T$ value at room temperature was found to be 8.45 cm^3 K/ mol per formula unit, which were in agreement with the theoretically calculated value expected

for two magnetically isolated Fe^{III}centers. For $[Fe_2(dhbq)_3]$, considering both the Fe center in +3 high spin oxidation state the expected magnetic moment corresponds to two S = 5/2 is 8.75 cm^3 K/ mol. The observed $\chi_M T$ value is a bit lower than the expected value which could probably be because of some magnetic impurity present. $\chi_M T$ vs T plot showed similar shape that observed for [Fe(dhbq)] with Fe(II) coordinated with $dhbq^{2-}$, what correspond to spin-only value of Fe^{III}; 4.375 cm^3 K / mol. Moreover, abrupt increment of magnetic susceptibility below 50 K reveals the existence of antiferromagnetic coupling between high spin Fe^{III} center which was further evidenced by low temperature reduced MH plot **(Figure 3.11.2)**, as no saturation in magnetization could be seen even after applying a magnetic field of 7 T.

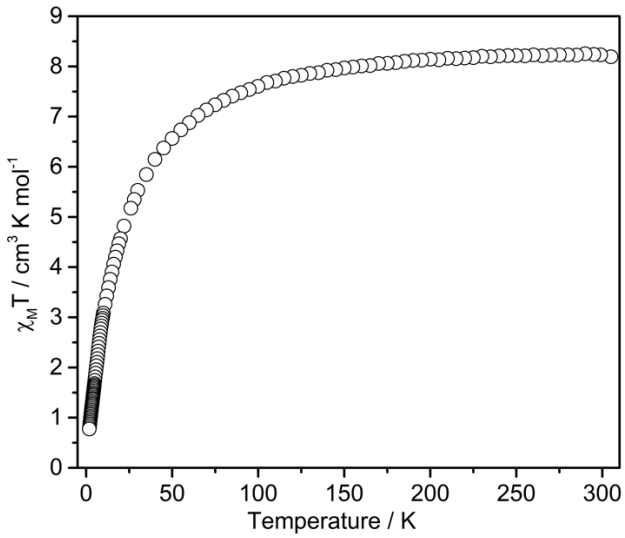

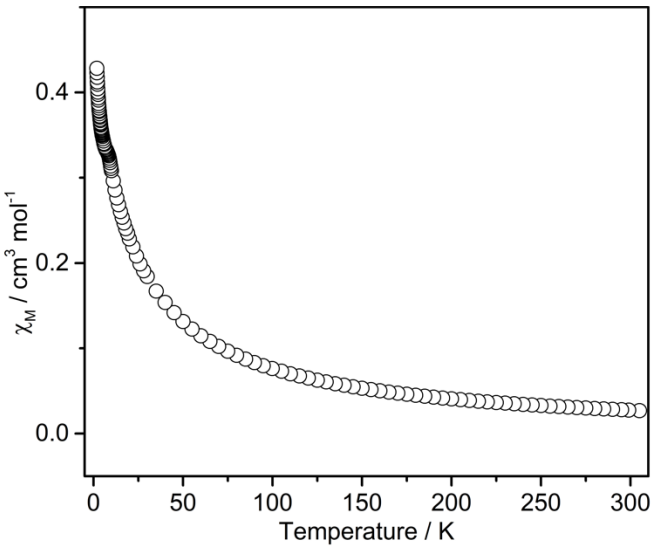

Figure 3.11.1 (a) Plot of $\chi_M T$ vs temperature and **(b)** Plot of χ_M vs temperature.

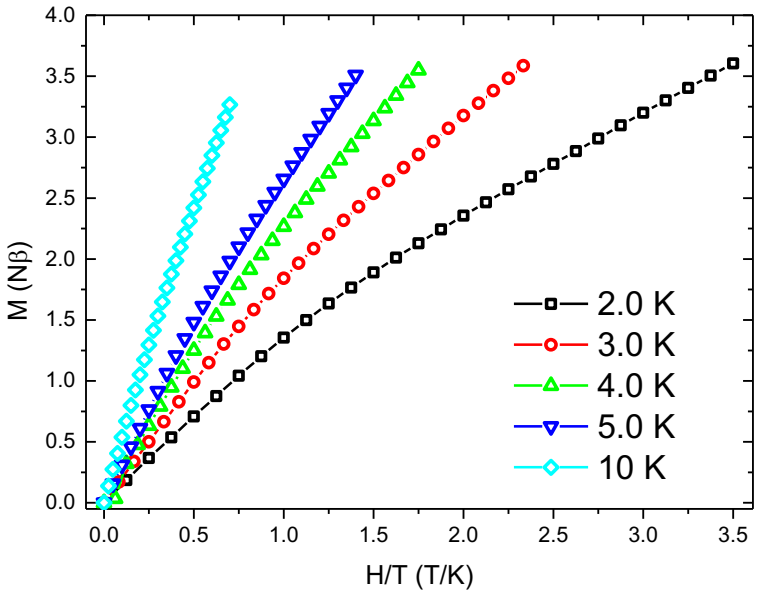

Figure 3.11.2 Magnetization *(M)* versus applied dc magnetic field (*H*) at variable temperature.

3.12 Solid state electrochemical study

3.12.1 Cyclic voltammetry

Plenty of reports are there based on MOF originated cathode materials which utilizes the redox active metal and ligand in order to achieve the better performance for lithium-ion storage however, Lower electrical conductivity and lack of porosity limits the use of a MOF to be used. [4,5]

The intrinsic conductive behavior, redox activity of well recognized $dhbq^{2-}$ ligands and microporosity of $[Fe_2(dhbq)_3]$ encouraged us to explore this as a cathode material. To probe the electrochemical behavior of $[Fe_2(dhbq)_3]$, we performed slow scan cyclic voltammetry. All samples preparation were performed inside the Ar glovebox. A glassy carbon electrode was used as working electrode, and a Ni wire coated with Li ribbon was used as reference and counter electrodes. The supporting electrolyte was 1M $LiClO_4$ in EC/DEC= 50/50 (V/V). Working electrode was prepared from a composite of activated metal organic framework (80 wt %), PVDF (Polyvinylidene Difluoride) (10 wt %) and acetylene black (10 wt %) after soft grinding dispersed in few drop of NMP. Drop cast on carbon electrode and let it dry in the glovebox. All the electrode were soaked in electrolyte filled a working cell. **Figure 3.12.1** shows a voltammogram of $[Fe_2(dhbq)_3]$ measured at a scan rate of 0.1 mV/S. Slow scan will help to investigate the redox activity inside the pores rather than the crystallite surface. It shows a broad reduction peak with a shoulder peak at 2.2 and 2.6 V versus Li^0/Li^+ respectively. The main reduction peak exclusively corresponds to $6e^-$ reduction based on $3dhbq^{-2}$ ligands and the shoulder peak could be assigned as partially Fe^{III}/Fe^{II} reduction centered, which was also confirmed by XANES spectra.

.

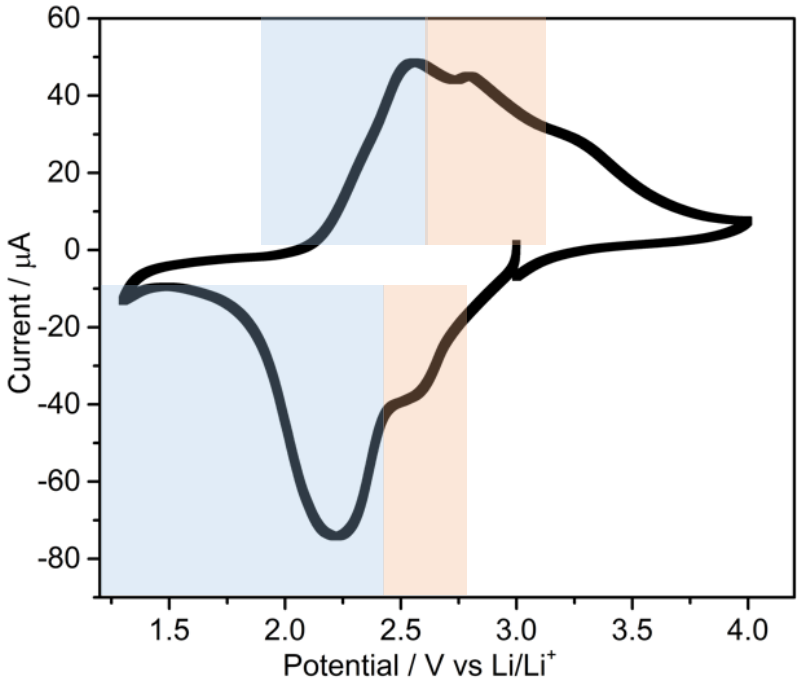

Figure 3.12.1 Solid-state cyclic voltammogram with a scan rate of 0.1 mV S^{-1}.

3.12.2 Galvanostatic measurements

For Galvanostatic measurements, coin cell was prepared using lithium foil as anode celgard separator and 50/40/10 wt % (MOF/ PVDF/ acetylene black) as cathode composite filled with electrolyte and sealed. Galvanostatic characteristic was performed with a charge rate of 41 mA g^{-1} in a potential window of 1.3 - 4.0 V and estimated the capacity of the cathode (**Figure 3.12.2**). $[Fe_2(dhbq)_3]$ achieved a first discharged capacity value of 322 mA h / g, which was more than the theoretically calculated value of 306 mA h / g considering $6e^-$ reduction upon complete reduction. The increased capacity of the material could be derived from the reduction of Fe (III). Although in the next cycles the capacity has decreased to 170 mA h / g which could be because of the irreversible redox

behavior of Fe (III) or once iron is reduced to Fe (II) it may have combined THB^{-4} and an irreversible loss of crystal happened. Taking the aforementioned statement into consideration, we performed ex-situ XANES spectral measurement upon complete 1st reduction and 1st oxidation. Over the course of electrochemical cycling, subsequent decrement in the capacity can be seen. Foremost reason could be the irreversibility of the redox activity of Fe which further leads to decomposition of MOF.

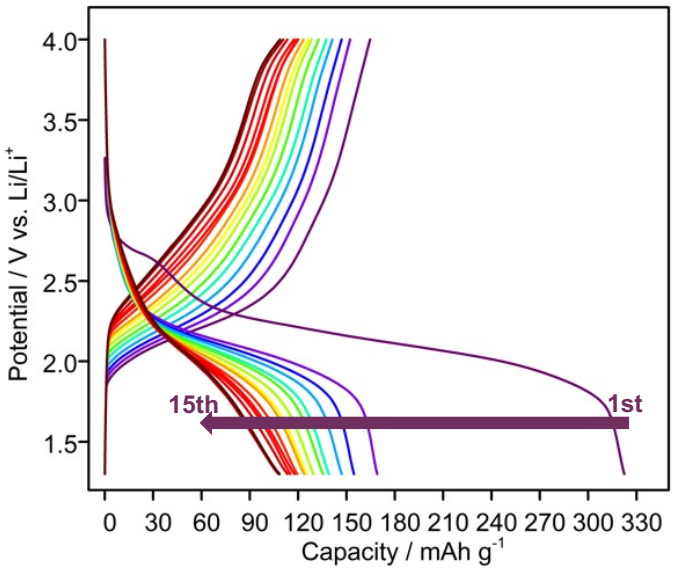

Figure 3.12.2 Charge−discharge characteristics of $[Fe_2(dhbq)_3]$ at a rate of 0.1 C (41 mA g^{-1}).

3.13 Ex-Situ investigation

Upon comparing with the edge absorption spectra of as synthesized $[Fe_2(dhbq)_3]$, shift towards lower energy was observed somewhere in between the energy of Fe (III) and Fe (II) (**Figure 3.13.1)**. However, the absorption energy does not correspond to the [Fe(dhbq)]. As indicative of the fact that the energy of absorption edge decreases upon lowering the oxidation state, we concluded that a fraction of Fe(III) center gets also

reduced. The reason for relatively lower capacity value of 164 mA h / g upon complete oxidation could probably be because of irreversible redox behavior of Fe center, which was further evidenced by XANES spectra **Figure 3.13.1**. Since the pore diameter is comparatively small Which clearly indicates the identical absorption edge spectra in the complete reduced and oxidized state of the MOF.

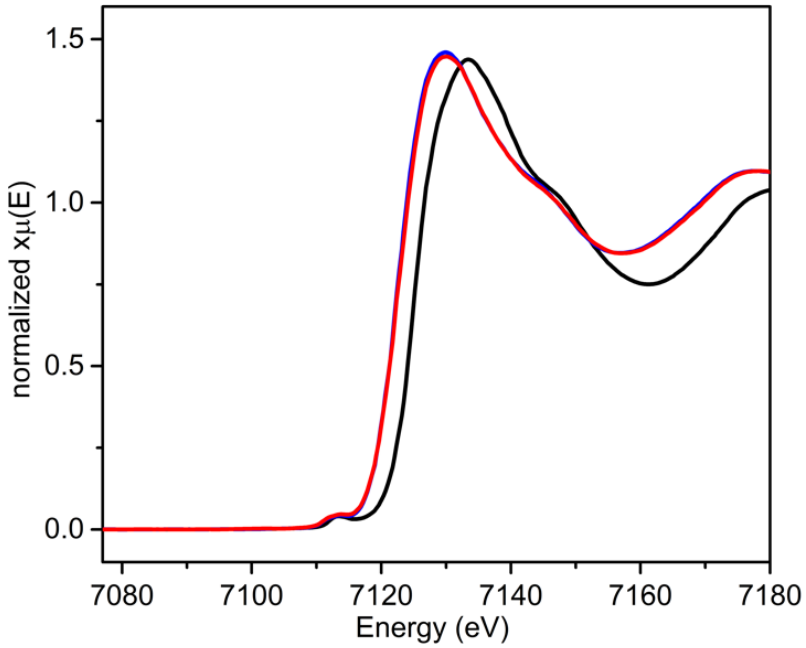

Figure 3.13.1 Ex-situ XANE spectra of Fe_2dhbq_3rt (black line), After 1st reduction (red line), after 1st oxidation (blue line).

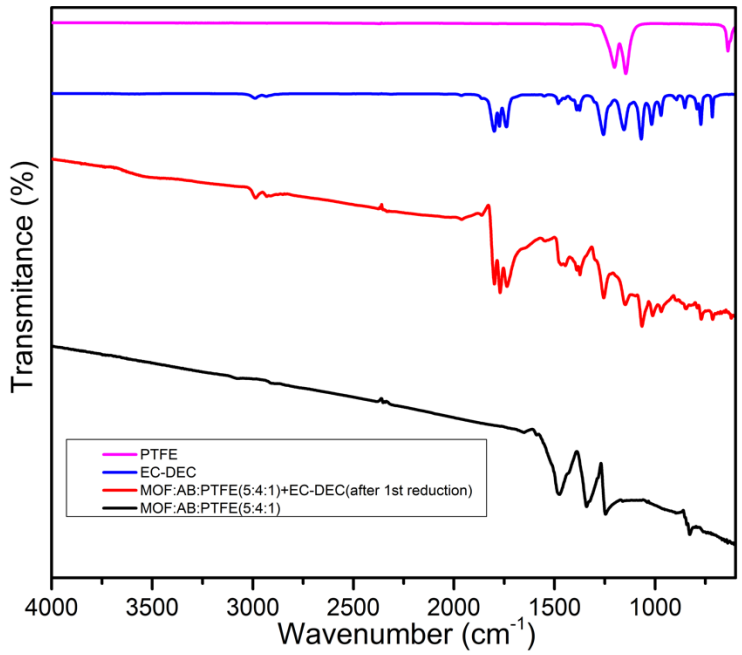

Figure 3.13.2 Ex-situ FT-IR spectra of Fe_2dhbq_3rt before and after 1st reduction.

3.14 Conclusion

In this chapter, we have reported the first ever obtained neutral dhbq based neutral 3-D micropores $[Fe_2(dhbq)_3]$ MOF. There have been several reports published based on $X_2dhbq^{2-/3-}$ ligands, including 1D and 2D coordination polymers. However, only a few conducting 3D coordination polymers were reported and that too upon incorporating larger cations as a template. Larger cations usually occupy the pore of the MOF and result in a non-porous polymer. The compound was synthesized using slow aerial oxidation of the starting material i.e., THB^{4-} and Fe^{2+} in order slow down the nucleation and crystallization process and to grow single crystal. $[Fe_2(dhbq)_3]$ solely derived from $dhbq^{2-}$, no metal and ligand-based mixed valency was observed which was supported by diffuse reflectance spectra and FTIR spectra. The MOF exhibited significantly high electrical conductivity of 1.2×10^{-2} S cm^{-1}at 300 K which is because of the strong covalency

between metal and ligand. The majority of charge carrier was found to be electron investigated by thermoelectromotive force measurements. Solid state redox activity of the MOF was explored using cyclic voltammetry and it was reported that two redox peaks were observed which belongs to the redox activity of metal as well as ligand. The redox activity based of metal ligand and such a high electrical conductivity inspired us to be investigate the MOF as a cathode material for LIB. Upon fabricating the MOF as a cathode for a LIB, it showed a significantly high specific capacity (322 mA h / g) while undergoing first discharge. Such a high value of discharge capacity is result of the many electron uptakes which was consistent with the result obtained by solid CV. The capacity loss was encountered in the second discharge cycle which is because of the irreversible redox behavior of metal. Once iron is reduced to Fe (II) it may have combined THB^{-4} and an irreversible loss of crystal could be possible. Which was also supported by Ex situ XANES spectral analysis.

Reference:

(1) Dei, A.; Gatteschi, D.; Pardi, L.; Russo, U. Tetraoxolene Radical Stabilization by the Interaction with Transition-Metal Ions. *Inorg. Chem.* **1991**, *30* (12), 2589–2594. https://doi.org/10.1021/ic00012a006.

(2) Darago, L. E.; Aubrey, M. L.; Yu, C. J.; Gonzalez, M. I.; Long, J. R. Electronic Conductivity, Ferrimagnetic Ordering, and Reductive Insertion Mediated by Organic Mixed-Valence in a Ferric Semiquinoid Metal–Organic Framework. *J. Am. Chem. Soc.* **2015**, *137* (50), 15703–15711. https://doi.org/10.1021/jacs.5b10385.

(3) DeGayner, J. A.; Jeon, I.-R.; Sun, L.; Dincă, M.; Harris, T. D. 2D Conductive Iron-Quinoid Magnets Ordering up to T_c = 105 K via Heterogenous Redox Chemistry. *J. Am. Chem. Soc.* **2017**, *139* (11), 4175–4184. https://doi.org/10.1021/jacs.7b00705.

(4) Ziebel, M. E.; Gaggioli, C. A.; Turkiewicz, A. B.; Ryu, W.; Gagliardi, L.; Long, J. R. Effects of Covalency on Anionic Redox Chemistry in Semiquinoid-Based Metal–Organic Frameworks. *J. Am. Chem. Soc.* **2020**, *142* (5), 2653–2664. https://doi.org/10.1021/jacs.9b13050.

(5) Kon, K.; Uchida, K.; Fuku, K.; Yamanaka, S.; Wu, B.; Yamazui, D.; Iguchi, H.; Kobayashi, H.; Gambe, Y.; Honma, I.; Takaishi, S. Electron-Conductive Metal–Organic Framework, Fe(Dhbq)(Dhbq = 2,5-Dihydroxy-1,4-Benzoquinone): Coexistence of Microporosity and Solid-State Redox Activity. *ACS Appl. Mater. Interfaces* **2021**, *13* (32), 38188–38193. https://doi.org/10.1021/acsami.1c06571.

(6) Jeon, I.-R.; Negru, B.; Van Duyne, R. P.; Harris, T. D. A 2D Semiquinone Radical-Containing Microporous Magnet with Solvent-Induced Switching from T_c = 26 to

80 K. *J. Am. Chem. Soc.* **2015**, *137* (50), 15699–15702. https://doi.org/10.1021/jacs.5b10382.

(7) Ziebel, M. E.; Darago, L. E.; Long, J. R. Control of Electronic Structure and Conductivity in Two-Dimensional Metal–Semiquinoid Frameworks of Titanium, Vanadium, and Chromium. *J. Am. Chem. Soc.* **2018**, *140* (8), 3040–3051. https://doi.org/10.1021/jacs.7b13510.

(8) Murase, R.; Abrahams, B. F.; D'Alessandro, D. M.; Davies, C. G.; Hudson, T. A.; Jameson, G. N. L.; Moubaraki, B.; Murray, K. S.; Robson, R.; Sutton, A. L. Mixed Valency in a 3D Semiconducting Iron–Fluoranilate Coordination Polymer. *Inorg. Chem.* **2017**, *56* (15), 9025–9035. https://doi.org/10.1021/acs.inorgchem.7b01038.

(9) Abrahams, B. F.; Hudson, T. A.; McCormick, L. J.; Robson, R. Coordination Polymers of 2,5-Dihydroxybenzoquinone and Chloranilic Acid with the (10,3)- *a* Topology. *Cryst. Growth Des.* **2011**, *11* (7), 2717–2720. https://doi.org/10.1021/cg2005908.

(10) Kingsbury, C. J.; Abrahams, B. F.; D'Alessandro, D. M.; Hudson, T. A.; Murase, R.; Robson, R.; White, K. F. Role of NEt_4^+ in Orienting and Locking Together $[M_2Lig_3]^{2-}$ (6,3) Sheets (H_2Lig = Chloranilic or Fluoranilic Acid) to Generate Spacious Channels Perpendicular to the Sheets. *Cryst. Growth Des.* **2017**, *17* (4), 1465–1470. https://doi.org/10.1021/acs.cgd.6b01886.

(11) Min, K. S.; Rheingold, A. L.; DiPasquale, A.; Miller, J. S. Characterization of the Chloranilate(•3−) π Radical as a Strong Spin-Coupling Bridging Ligand. *Inorg. Chem.* **2006**, *45* (16), 6135–6137. https://doi.org/10.1021/ic061076k.

(12) Guo, D.; McCusker, J. K. Spin Exchange Effects on the Physicochemical Properties of Tetraoxolene-Bridged Bimetallic Complexes. *Inorg. Chem.* **2007**, *46* (8), 3257–3274. https://doi.org/10.1021/ic070005y.

(13) Kitagawa, S.; Kawata, S. Coordination Compounds of 1,4-Dihydroxybenzoquinone and Its Homologues. Structures and Properties. *Coord. Chem. Rev.* **2002**, *224* (1), 11–34. https://doi.org/10.1016/S0010-8545(01)00369-1.

(14) Torrance, J. B.; Scott, B. A.; Welber, B.; Kaufman, F. B.; Seiden, P. E. Optical Properties of the Radical Cation Tetrathiafulvalenium (TTF+) in Its Mixed-Valence and Monovalence Halide Salts. *Phys. Rev. B* **1979**, *19* (2), 730–741. https://doi.org/10.1103/PhysRevB.19.730.

(15) Westre, T. E.; Kennepohl, P.; DeWitt, J. G.; Hedman, B.; Hodgson, K. O.; Solomon, E. I. A Multiplet Analysis of Fe K-Edge 1s f 3d Pre-Edge Features of Iron Complexes.

Chapter 4.

Development of $Na[Pt^{III}(pdt)_2].2H_2O$ based 1-D conductor and Investigating Electrical, Thermoelectric Properties.

4.1 Chapter introduction

Dithiolene based metal complexes[1–3] have gained considerable attraction over the last few decades due to its curious electronic structure and very interesting solid-state properties like molecular conductors and superconductors.[4,5] Dozens of studies on metal dithiolene based complexes have been reported which reveals single molecular metals and super conductors likes behavior have been realized.

In the case of molecular conductors, designing strategy is very important. In order to achieve the stacks of the square planar dithiolene based metal complexes is one of the prelim requirements for the SCMM.[6] Which provides a delocalized band structure upon establishing effective orbital overlapping between the two stacks. Another requirement is the partially occupied delocalized band structure.[6] In the case of 1-D organic metals it can undergo Peierls instability as a result of lattice distortion which in turn convert the metallic behavior to semiconductors. Peierls instability can be suppress upon incorporating the increased inter stacked structure which will help in maintaining the metallic state even at low temperatures.

Square planar dithiolene based metal complexes can exists in the form of dianions, monoanions or the neutral form.[7] In the case of monoanions, HOMO is having one electron. When the delocalized band will form upon overlapping the HOMO of the adjacent molecules, it will result in the half full delocalized band. Such kind of systems are prone to Peierls instability. And undergo dimerization which in turn causes a formation of filled bands and hence a semiconducting property. Whereas, in the case of dianions and neutral complexes, a pair of electrons is there in the HOMO and upon overlapping of the

HOMO from adjacent molecules, it will result in the completely full delocalized band and hence a semiconducting property.

There are many organic compounds reported, that showed low temperature superconductivity, either at ambient pressure or under pressure. Most of them are based of TTF molecules and its derivatives.[8,9] Where metallic characteristics arise from the effective overlapping of wavefunction of two stacked layers.

π- π interactions in the case MOFs can also lead to a formation of 1-D charge transport pathway. MOFs with organic components having π- π interactions can lead to the charge transportation through-space pathways. Small separation between the stacked layer causes the overlapping of the wave function in the stacked direction and hence creating charge transport pathways. In contrast to metal-ligand bonding, it focuses on intermolecular interaction of ligands only. Common example of organic components that possess π- π stacking are planar conjugated ligands such as tetracyanoquinodimethane (TCNQ), tetrathiafulvalene (TTF), anthracene, naphthalene naphthalenediimide.

4.2 Research objective and strategy

In order to achieve through space conduction, stacks of the square planar dithiolene based metal complexes is one of the prelim requirements. Complete face to face stacking ensures the proper overlapping of the wavefunctions of two π stacked organic core, which creates the pathways for the charge delocalization in the direction of stacking. Drawback of 1-D organic metals is lattice distortion, which causes Peierls instability and is responsible for conversion of metallic to insulators. Peierls instability can be suppress upon incorporating the increased inter stacked structure.

Another requirement is the partially occupied delocalized band structure. In the case of monoanions, the HOMO is having one electron. When the delocalized band will form upon overlapping the HOMO of the adjacent molecules, it will result in the half full delocalized band. So, considering the above two requirements in order to realize molecular conductor so we decided to choose dithiolene based ligand i.e., 2,3-Pyrazinedithiol as an organic core. The extended orbital of Sulfur will help in achieving the stacked structure and short-range intermolecular interactions such as S-S, S-H and S-N contributes to increase the dimensionality. In order to attain the partially delocalized HOMO, monoanion structural unit is design upon incorporating Platinum in +III oxidation state. Detailed study of conductivity, charge carrier and magnetic data will be discussed in the nest section.

4.3 Synthesis of $Na[Pt(pdt)_2].2H_2O$

2,3-Pyrazinedithiol ligand was prepared according to protocols mentioned in the literature. $Na[Pt(pdt)_2].2H_2O$ was synthesized as follows. In a conical flask, NaOH (80 mg, 2eq, 2 mmol) was dissolved in 44 ml of deionized water. H_2pdt_2 (144 mg, 1eq, 1mmol) was added to the NaOH solution. Stir the mixture until color of the solution became pale yellow. $PtCl_2$ (133 mg, 0.5eq, 0.5mmol) was added to the flask while stirring, followed by 6 ml MeOH. After mixing everything sonication was performed for 20 minutes. The color of the solution turned dark red. The reaction mixture was heated at 60 ^oC overnight.

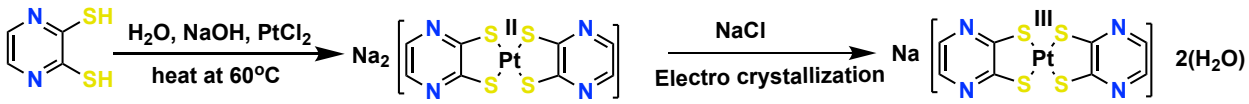

Scheme 4.3.1 Synthetic scheme of $Na[Pt(pdt)_2].2H_2O$

After cooling down to room temperature, supporting electrolyte NaCl (75mg, 50mmol) was added to the reaction mixture. (**Scheme 3.3.1**). Small fraction of the solution was kept for electro-crystallization at a constant current of 10 μA for a week. Detailed setup for the electro-crystallization method in demonstrated in **Figure 3.3.1**. Black color needle like crystals was obtained at anode. Crystals were carefully collected and washed with water. Single crystals obtained were of very small size, not suitable for SXRD measurement. However relatively larger crystals were grown using slow evaporation of acetone solution. Obtained crystals were suitable for SXRD measurement. Elemental analysis, Calcd for $NaPtC_8H_8S_4N_4O_4$: C, 17.84 % ; H, 1.5 % ; N, 10.4 %. Found: C, 17.77 % ; H, 1.52 % ; N, 10.24 %.

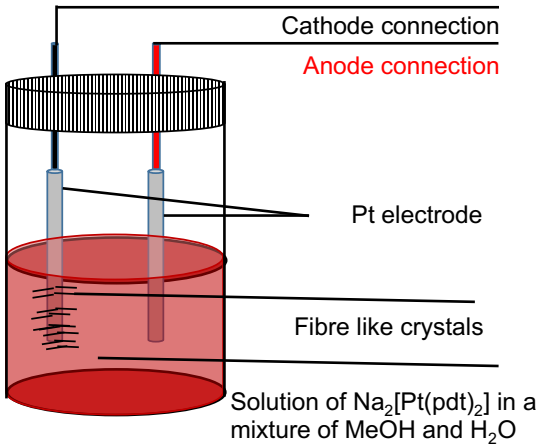

Figure 4.3.1 Schematic illustration of electrolysis method used for the synthesis of $Na[Pt(pdt)_2].2H_2O$ single crystals.

Characterization

4.4 Crystal description

Single crystals of $Na[Pt(pdt)_2].2H_2O$ were obtained by recrystallization in acetone were analyzed using single-crystal X-ray diffraction (SXRD). It crystalizes in a orthorhombic crystal system with an space group of Pnnm. Each Pt center is coordinated to 4 S atoms in a square planar geometry **(Figure 4.4.1a)**. Sulfur atoms are derived from 2 pdt^{2-} ligands. One of the two nitrogen atoms from the pyrazinedithiolate ligand was coordinated to sodium atom (N-Pt distance=2.564) via weak N-Pt coordination bond. So basically, sodium atom acts as a bridge between two $[Pt(pdt)_2]$ unit in *bc* plane **(Figure 4.4.1a)**. The geometry around Na is octahedral where four other positions are occupied oxygen atom from four aqua molecules. Thus a 1-D chain is formed in *a* direction with Na and two aqua molecules placed alternatively with an Na-Na distance of 3.63 Å **(Figure 4.4.2b)**. Each aqua molecules are bonded to two sodium atoms in a μ_2 manner. The square planar units are face to face stacked in a direction with an interplanar distance of 3.63 Å. A strong π-π interaction between the ligands in *a*-direction result in a 3D extended framework **(Figure 4.4.2a)**. In case of the ligand such as semiquinones, bond length estimation plays an important role in order to decide the nature of aromatic ligand weather it is open shell or closed shell. Where open shell aromatic ring usually exhibits short-long-short order of bond length, which implies a presence of pi radical system. On the other hand, aromatic ring containing closed ring shows all the C-C bonds of equal size. In our report of Pt, considering the bond length semi thionate character was emerged which could be because of strong charge transfer from ligand to metal center.

4.4.1 Crystal structure of $Na[Pt(pdt)_2].2H_2O$

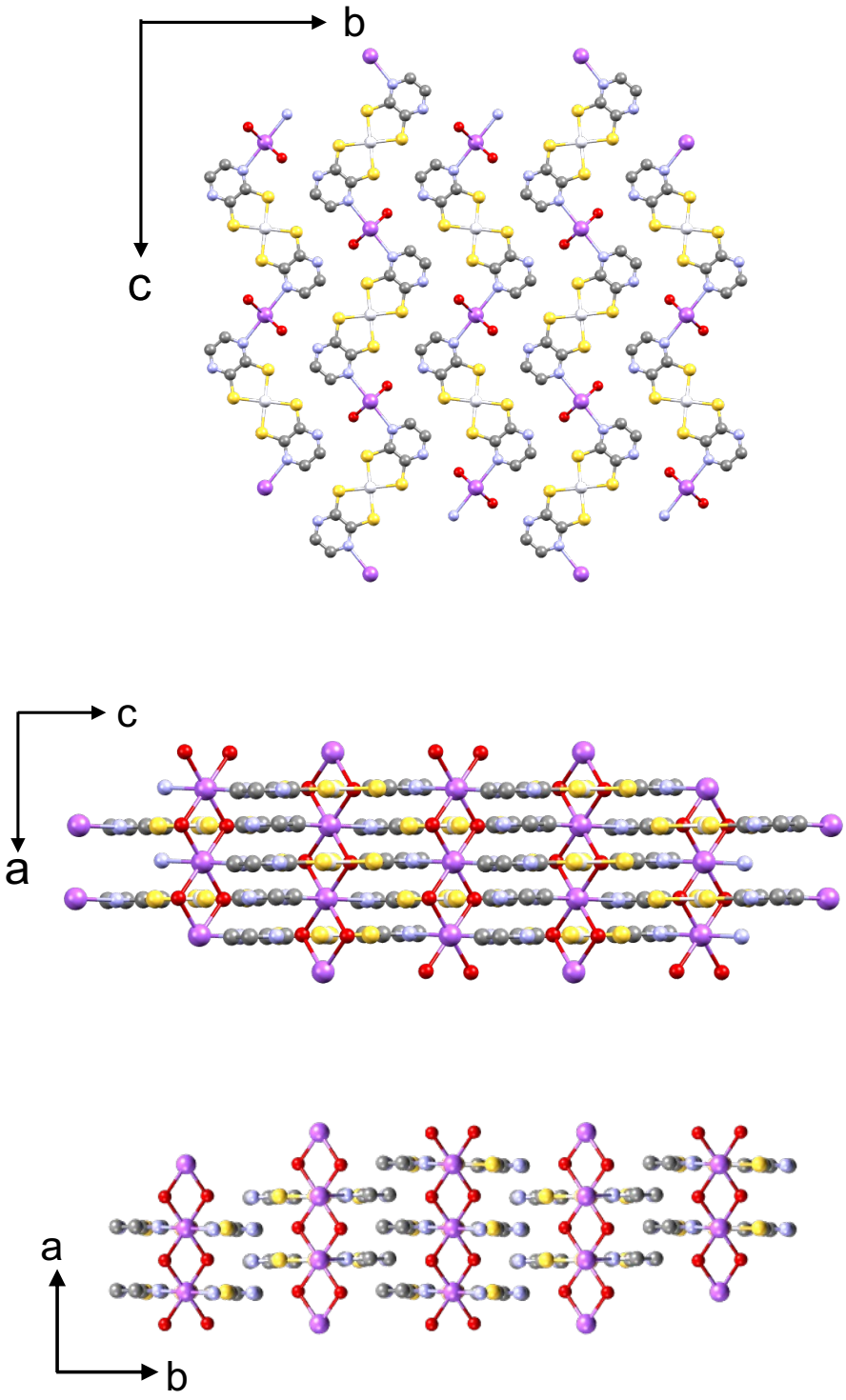

Figure 4.4.1 (a) View along a axis (Stacking axis) **(b)** along b axis **(c)** along the c axis (shortest axis) Violet (sodium), yellow (sulfur), red (oxygen), purple (nitrogen), gray (carbon).

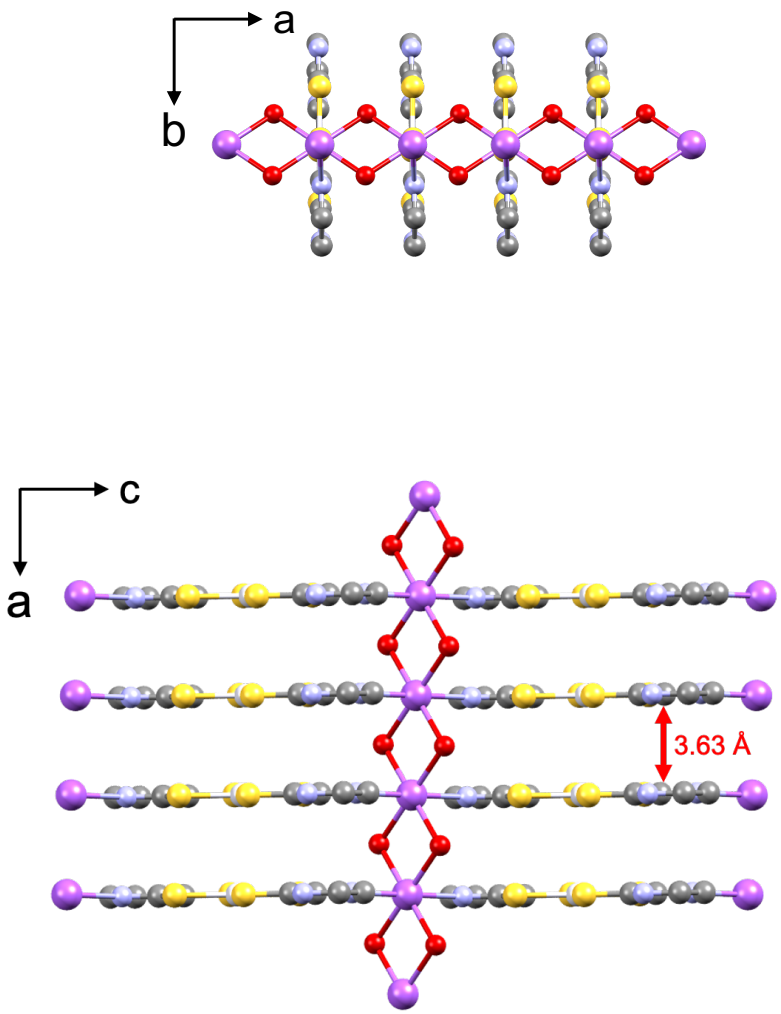

Figure 4.4.2 (a) Octahedral coordination environment around Na center. Infinite chain of —Na–(μ-O_{aq}) –Na–(μ-O_{aq}) along b axis. **(b)** representation of stacked structure along a-axis with intermolecular stacking of 3.63 Å.

Table 4.4.1 Crystallographic information of $Na[Pt(pdt)_2].2H_2O$

Empirical formula	$C_8H_8N_4NaO_2PtS_4$
Formula weight	538
Temperature/K	120
Crystal system	monoclinic
Space group	$P2_1/n$
a/Å	3.63000(10)
b/Å	15.1334(6)
c/Å	12.4026(5)
α/°	90
β/°	92.502(4)
γ/°	90
Volume/Å^3	680.68(4)
Z	4
ρ_{calc} g/cm^3	2.627
μ/mm^{-1}	10.955
F(000)	506.0
Crystal size/mm^3	0.1 × 0.02 × 0.02
Radiation	Mo Kα (λ = 0.71073)
2Θ range for data collection/°	7.106 to 63.852
Index ranges	$-5 \leq h \leq 5$, $-22 \leq k \leq 19$, $-17 \leq l \leq 17$
Reflections collected	7737
Data/restraints/parameters	2017/0/94
Goodness-of-fit on F^2	1.081
Final R indexes [I>=2σ (I)]	R_1 = 0.0270, wR_2 = 0.0709
Final R indexes [all data]	R_1 = 0.0351, wR_2 = 0.0746
Largest diff. peak/hole / e Å^{-3}	3.99/-1.64

4.4.2 PXRD data

Phase purity of the bulk sample was investigated with the help of PXRD measurement. As shown in **Figure 4.4.2** bulk sample showed the same diffraction pattern to that of the simulated data and also confirmed the phase purity.

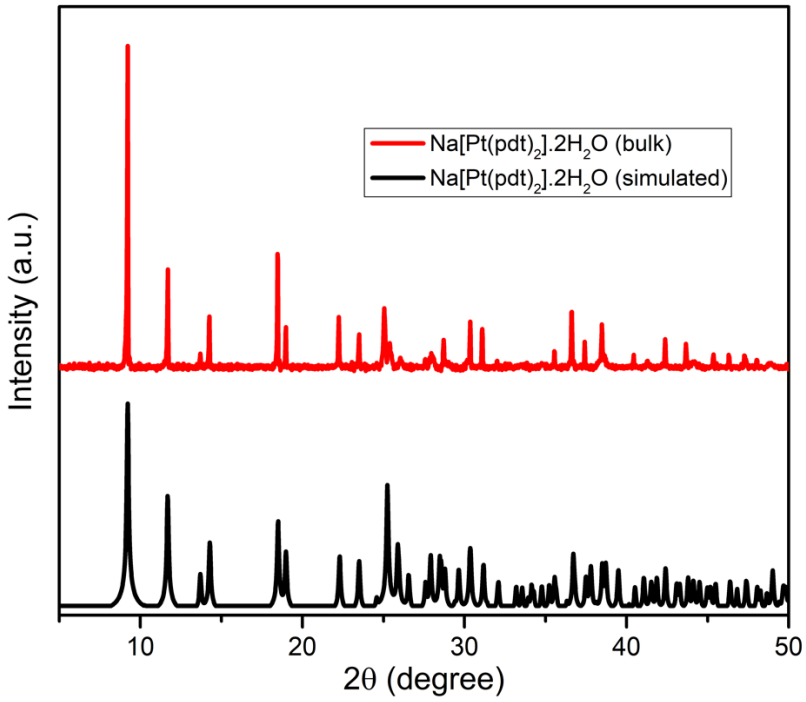

Figure 4.4.2 PXRD pattern of $Na[Pt(pdt)_2].2H_2O$ (simulated) and as synthesized .

4.5 Structural investigation of recrystallized sample

As mentioned in the section 3.1, square planar dithiolene based metal complexes can exists in the form of dianions, monoanions or the neutral form. In the case of monoanions, the HOMO is having one electron. When the delocalized band will form upon overlapping the HOMO of the adjacent molecules, it will result in the half full delocalized band. Such kind of systems are prone dimerization which in turn causes a formation of filled bands

and hence a semiconducting property. Since all the investigation related to electrical properties were performed using the single crystal obtained by recrystallization, so it's very crucial to investigate if the crystal structure is same after the recrystallization. The first investigation was performed using PXRD. In **Figure 4.5.1** the PXRD pattern of both the samples are same, which indicates that structural skeleton was same. Just a little bit of crystallinity loss was there in case of recrystallized one.

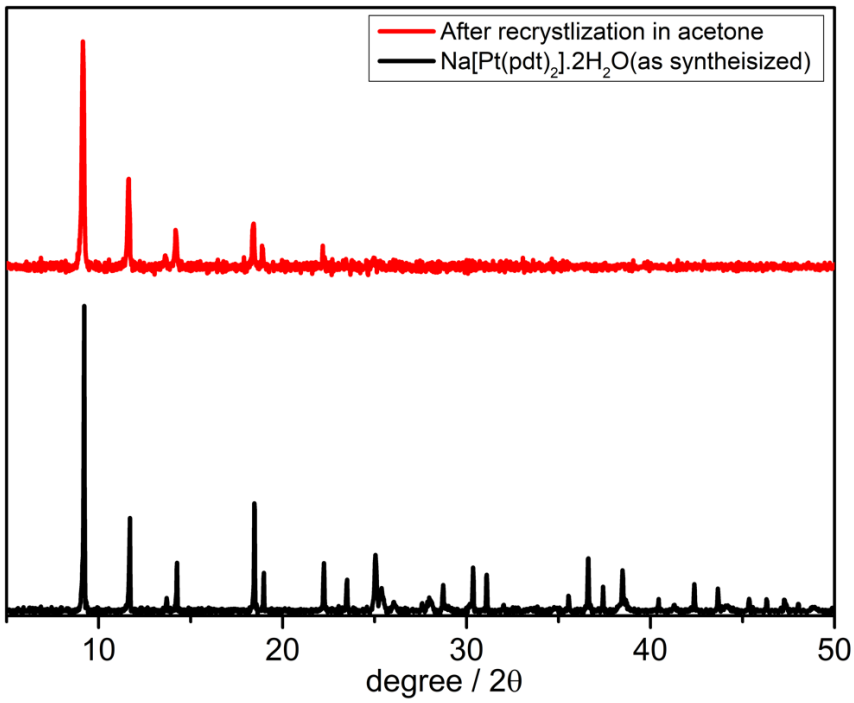

Figure 4.5.1 PXRD pattern of $Na[Pt(pdt)_2].2H_2O$ (as synthesized and) and recrystallized.

Later we measured the FTIR spectra of both the samples and we found that transmittance spectra of both the samples were same **Figure 4.5.2**. In the solid state, both of the above investigation suggested that the sample was retained the same even after the recrystallization. But what about in the solution state? To know more detailed information about the structural changes in the solution state we measured the mass spectra of the

sample in the solution to investigate if there is any dimerization is occurring. **Figure 4.5.3** shows the mass spectra in the acetone, the base peak at 479 corresponds to $[Pt(pdt)_2]$. There was no any peak was observed which corresponds to the dimerization of $Pt(pdt)_2$ unit.

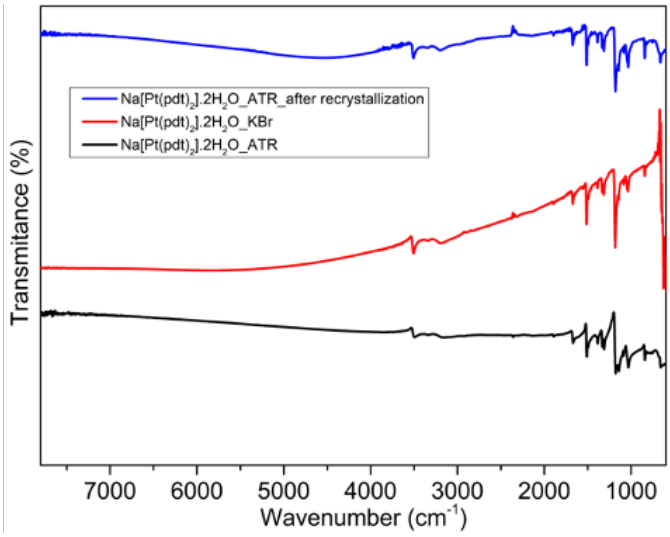

Figure 4.5.2 FTIR spectra of $Na[Pt(pdt)_2].2H_2O$ (as synthesized and) and recrystallized.

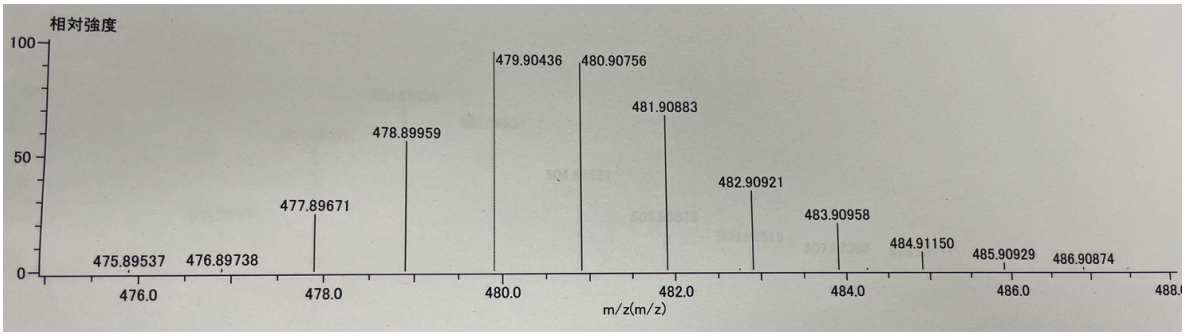

Figure 4.5.3 Mass spectra of $Na[Pt(pdt)_2].2H_2O$ in acetone

In order to confirm the formal charge of Pt in $Na[Pt(pdt)_2].2H_2O$, we perform the X-ray absorption near-edge structure (XANES) at the Pt L_3 edge of $Na[Pt(pdt)_2].2H_2O$. For the reference sample, we used XANES spectra of $TBA_2[Pt(pdt)_2]$ (**Figure 4.5.4)**. The complex was synthesized using the reported procedure. $TBA_2[Pt(pdt)_2]$ has Pt center in +II oxidation state. Figure shows the XANES spectra of both the above-mentioned complexes. Absorption edge energy of $Na[Pt(pdt)_2].2H_2O$ was found to be very close to $TBA_2[Pt(pdt)_2]$. So, XANES spectral analysis was not sufficient enough to justify the formal oxidation state of Platinum to be in +III.

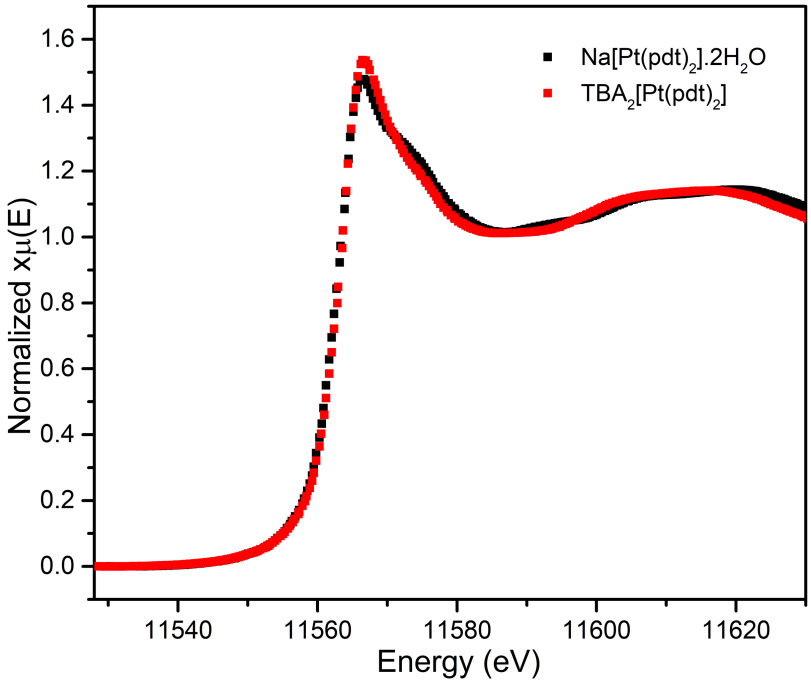

Figure 4.5.4 XANES $Na[Pt(pdt)_2].2H_2O$ (black line). Red line in the graph indicates XANES spectra of $TBA_2[Pt(pdt)_2]$ used as a reference sample.

EPR spectra of $Na[Pt(pdt)_2].2H_2O$ was measured in solution (solvent = acetone) as well as in solid state at 293 K. The spectrum displayed a broad signal at g =2.03 in the solution state. However, a rhombic signal was obtained in a solid state. Considering the SOMO obtained from the TD DFT calculation. It seems like SOMO has considerably huge contribution from the ligand and ESR signal is basically coming as a result of electron resides in the molecular orbital that have $[PtS_4]$ character.

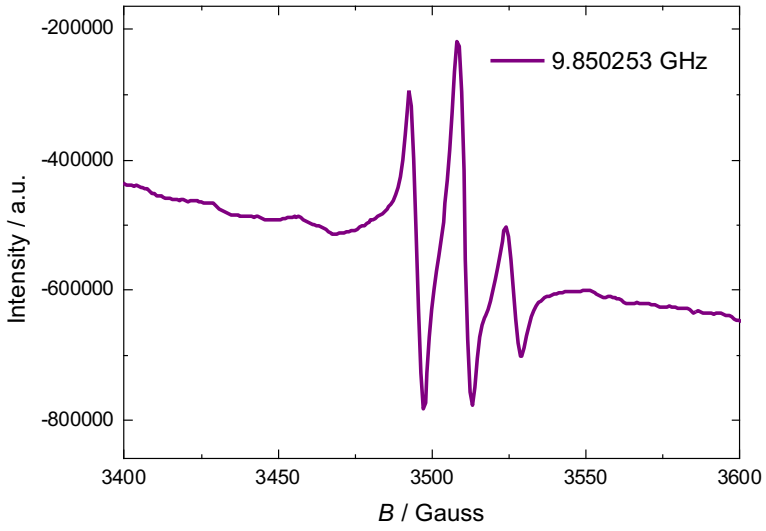

Figure 4.5.5 Solid state ESR spectra of $Na[Pt(pdt)_2].2H_2O$ at room temperature.

In order to get more detailed information, DFT calculation was performed. Electronic structural calculation was performed using Gaussian16, B3LYP/Lanl2dz method, shown in **Figure 4.5.6**. SOMO is mainly consists of π orbital of ligand. So, basically the relevant electron is not located in metal orbital, instead being reside in SOMO having [PtS4] character with mostly contribution from ligands.

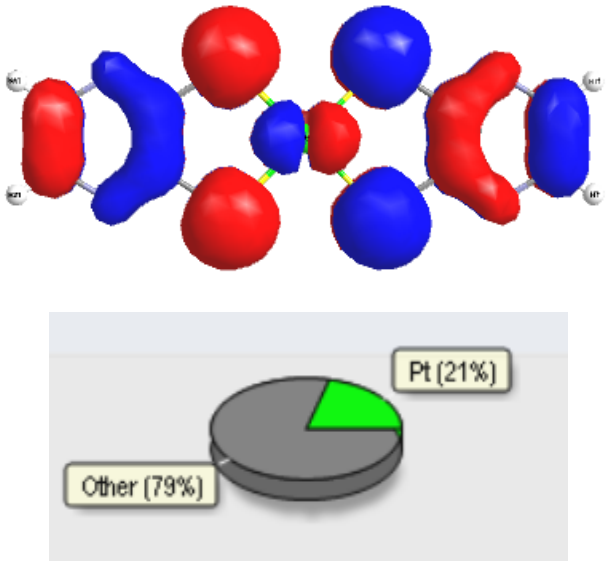

Figure 4.5.6 SOMO of $Na[Pt(pdt)_2].2H_2O$

^1H NMR spectrum has been playing an important role in order to characterize d^8 square planar diamagnetic complexes. Diamagnetic complexes containing aromatic protons shows a sharp peak in the aromatic region. However, paramagnetic complexes show broaden or no signal for the aromatic protons of the ligand. ^1H NMR spectra of $Na[Pt(pdt)_2].2H_2O$ was measured in acetone d^6 and deuterated methanol as sown in **Figure 4.5.7**. The spectra clearly indicate no signals for the protons attached to pyrazine molecules.

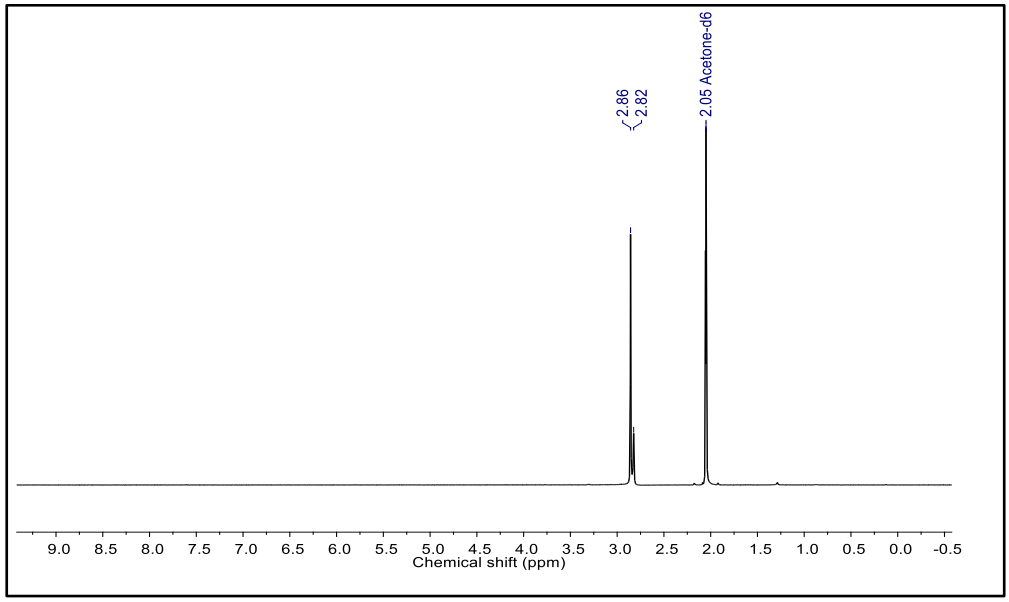

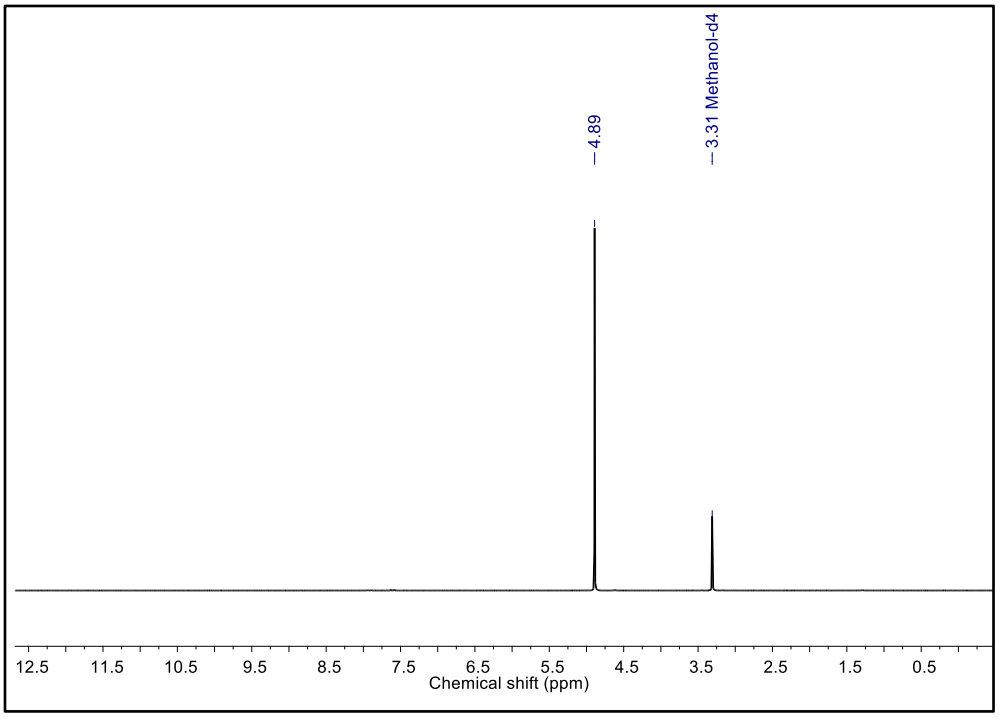

Figure 4.5.7 ^{1}H NMR spectra of $Na[Pt(pdt)_2].2H_2O$ (a) in acetone (b) in methanol.

4.6 Thermal stability

Thermal stability of the compound was investigated with the help of thermogravimetric analysis (TGA). Thermogravimetric measurement was performed upon activating the samples to 80 ºC for 24 hr under reduced pressure. Data was collected under N_2 atmosphere with a flow rate of 5º/ C. It can be seen in Figure that no weight was observed upto 160 ºC which implies that compound is thermally stable up to 160 ºC. After that a clear weight loss of 5.5% was observed. Which was in agreement with the 2 two water molecules that are coordinated to the sodium atom. TGA result was consistent with the elemental analysis (5.8%). There is no weight loss was observed up to 300 ºC. PXRD measurements of recovered sample from the TGA was performed. As shown in **Figure 4.6.1** loss of crystallinity was observed which implies that with the loss of the water molecules the crystal structure was decomposed. Water molecules played an important role for the stability of the compound.

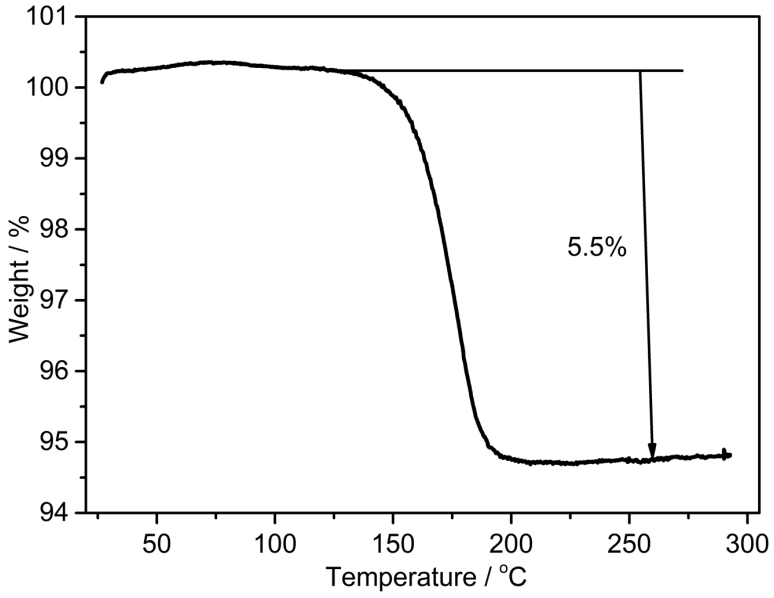

Figure 4.6.1 Thermogravimetric analysis up to 300 ºC under N_2 flow.

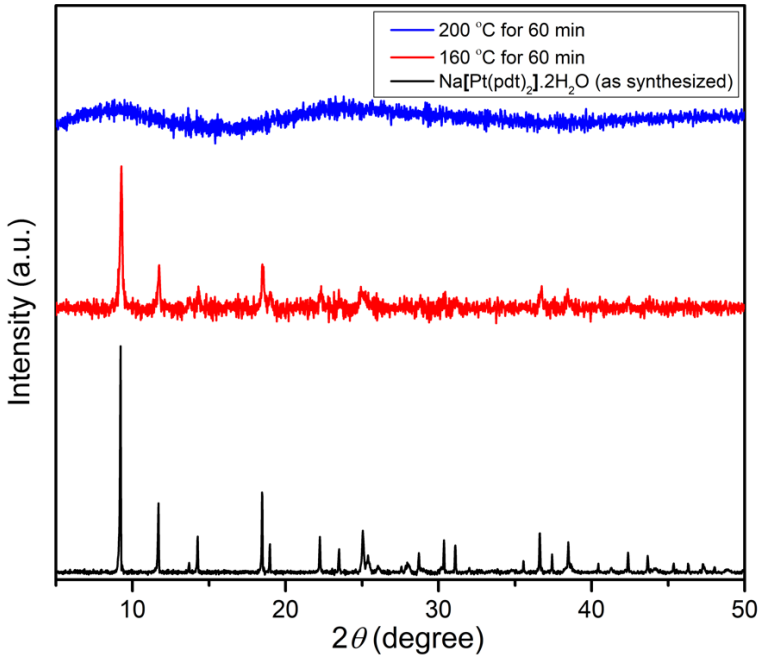

Figure 4.6.2 PXRD pattern of $Na[Pt(pdt)_2].2H_2O$ after TGA at different temperatures

Optical properties

4.7 UV-Vis-NIR spectroscopy

UV-Vis spectra was performed in the solution as well as in solid state. Solution state UV was carried out in acetone. A very intense band at 900nm was observed which was assigned to ligand-based transition i.e., π to π* transition. In the lower wavelength, at 450 nm relatively low intensity peak was observed. This peak was assigned as HOMO to LUMO transition.The UV-vis spectra were performed using polar protic (methanol and ethanol) and polar aprotic (acetone and acetonitrile) solvents. The compound showed solvatochromism effect (**Figure 4.7.1)**. Absorption spectra correspond to HOMO-LUMO transition showed bathochromic shift upon changing the solvents from polar aprotic to polar protic. i.e., absorbance shifted toward higher wavelength.

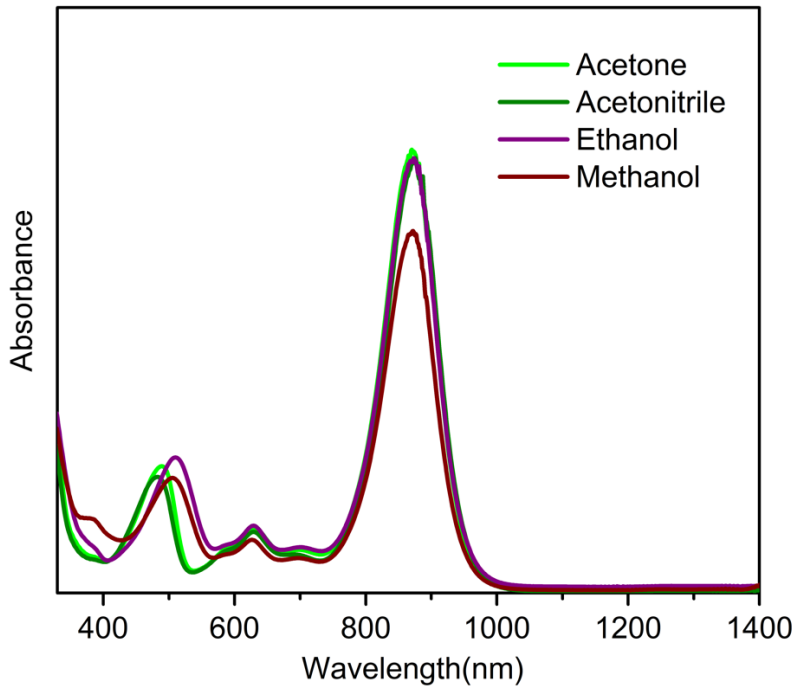

Figure 4.7.1 UV-vis spectra of $Na[Pt(pdt)_2].2H_2O$ in acetone (light green), acetonitrile (dark green), ethanol (purple) and methanol (brown).

UV-vis-NIR diffuse reflectivity spectra were collected on Shimadzu UV-3100PC spectrometer attached with Shimadzu ISR-3100 integrating sphere. $BaSO_4$ was used as a non-absorbing matrix to dilute the sample. The solid-state UV-vis-NIR spectrum illustrate a broad band at 0.7 eV, which indicates that the polymer possess a very small band gap of 0.7 eV (**Figure 4.7.2).**

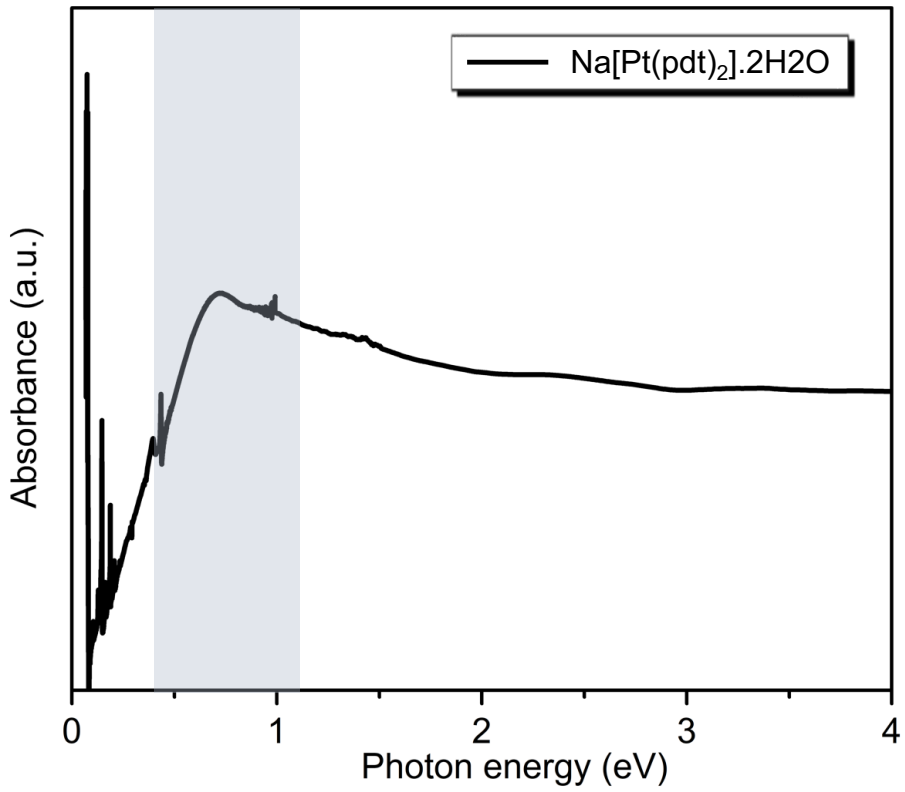

Figure 4.7.2 UV-vis-NIR diffuse reflectivity spectra of $Na[Pt(pdt)_2]2H_2O$.

4.8 Cyclic Voltammetry

Redox activity of the compound was investigated with the help of Cyclic voltammetry. Measurement was carried out in acetonitrile using $TBAPF_6$ as an electrolyte at a scan rate of 100 mVs^{-1}. The CV of $Na[Pt(pdt)_2].2H_2O$ showed only one redox phenomena. Reversible wave at $E_{1/2}$ =0.40 V vs Fc/Fc^+ is assigned to the $[Pt(pdt)_2]^{2-/1-}$ couple (**Figure 4.8)**. The reversible $[Pt(pdt)_2]^{2-/1-}$ couple was earlier reported in DMF. The obtained $E_{1/2}$ value is in agreement with literature report of $TBA_2[Pt(pdt)_2]$. Other than that, no any peak was observed which was in agreement with the other complexes based on pdt^{2-} and Cu/Ni/Pt/Pd. Furthermore, in the case all four metals different value of redox potential confirms the fact that redox process centered on metal atom rather than ligand.

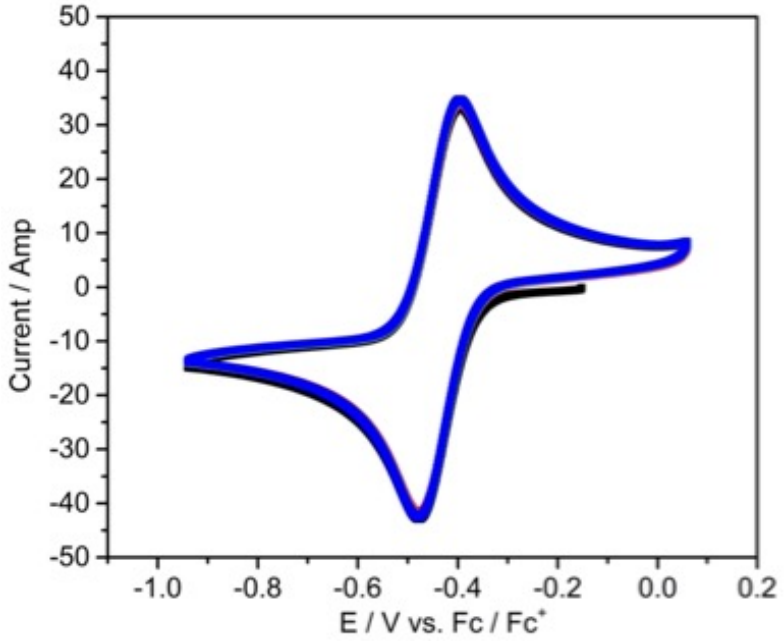

Figure 4.8 Cyclic voltammogram plot in acetonitrile using 0.1 M $TBAPF_6$ as an electrolyte.

4.9 Electrical properties

4.9.1 Temperature dependence of conductivity

Single crystal electrical conductivity was performed using a two-probe method. Dependency of temperature on conductivity was measured in the range of 150 to 300 K with heating and cooling cycles. As can be seen in **Figure 4.9.1a** electrical conductivity is increasing as result of result temperature increment, which confirms the semiconductor behavior of the compound. The compound showed an electrical conductivity of 1.2×10^{-2} S cm^{-1} at 300 K.

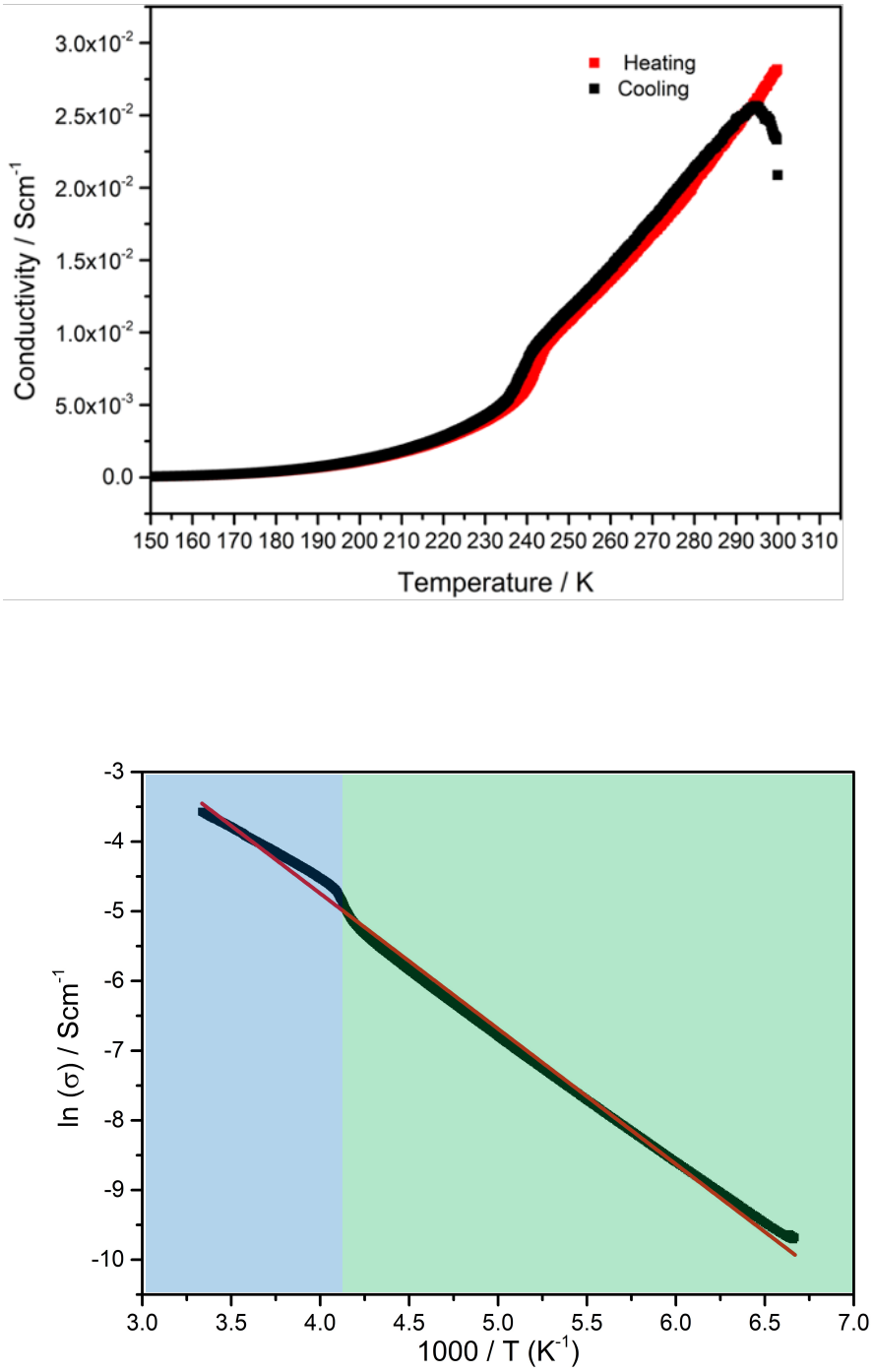

Figure 4.9.1 Temperature dependent electrical conductivity **(a)** Two probe single crystal conductivity **(b)** Arrhenius fitting of the conductivity data.

Such a high electrical conductivity is a result of π–π interaction between the organic core along *a*-axis. The strong π–π interaction leads to a 1D π stacked column which provides the pathway for the electron delocalization in the direction of stacking. Although the interlayer distance along the direction of stacking is relatively large (3.6 Å) but the extended orbital of the Sulfur atom and the face on stacking results in a proper overlapping of the wavefunction of two planes. **Figure 4.9.1b** shows the Arrhenius plot of the conductivity data and calculated activation energy is found to be 167 meV. Which indicates a narrower band gap. The very tiny and fragile crystal of the compound prevented the reproducibility of resistivity measurements. However, upon fitting the two halves of the Arrhenius plot showed an activation energy of 124 and 156 meV in the range of 300-240 K and 240-150 K respectively.

In order to confirm the room temperature conductivity, we also investigated the temperature dependent conductivity using a pressed pellet sample via two-point contact method. The observed data was in great agreement with the data obtained from single crystal which shows an electrical conductivity of 1.2×10^{-2} S cm^{-1} at 300 K. Arrhenius fitting of the conductivity data indicate an activation energy of 178 meV. (**Figure 4.9.2)**

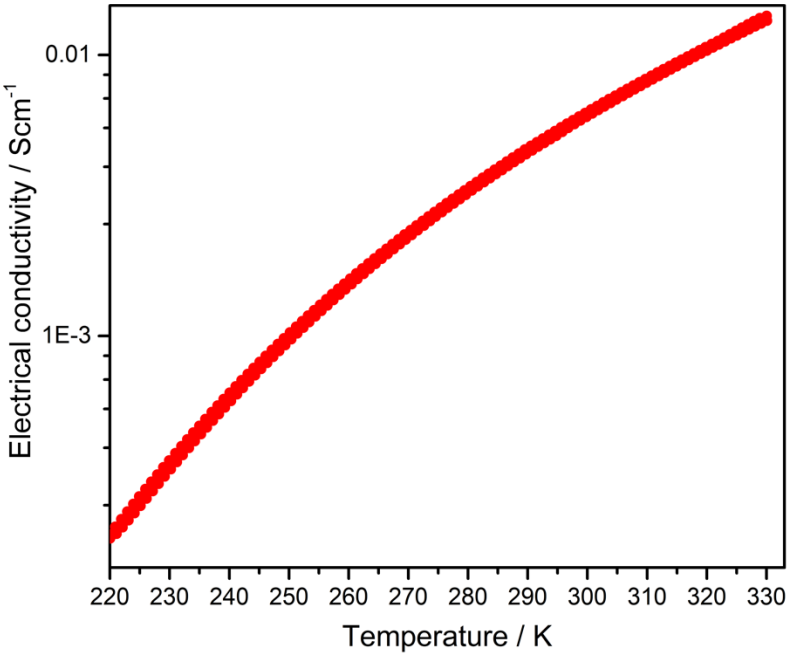

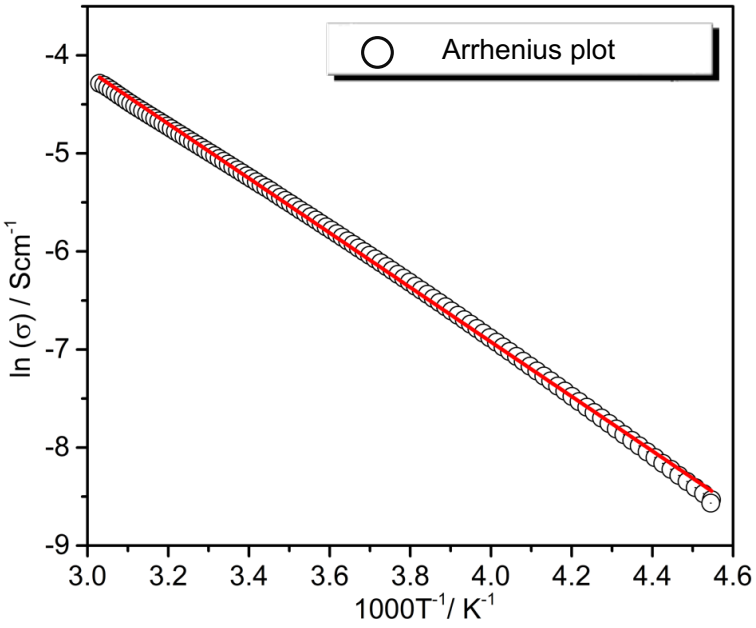

Figure 4.9.2 (a) Temperature dependent electrical conductivity of pressed pellet sample using two probe method **(b)** Arrhenius fitting of the conductivity data.

4.9.3 Current (*I*)/ Voltage (*V*) characteristics

The room temperature electrical conductivity of bulk sample was also investigated with the help of current(*I*) - voltage (*V*) characteristic using a pressed pellet of surface area 0.07 cm^2 and length 0.06cm as shown in **Figure 4.9.3** A linear relationship between current and voltage indicates that it follows ohmic relationship. The slope of this plot gives the resistance of the sample. The conductivity was estimated to 1.6×10^{-3} S cm^{-1} from *I-V* plot. One order lower conductivity in the case of *I-V* measurement could probably be due to the grain boundary effect or the thermally induced resistance.

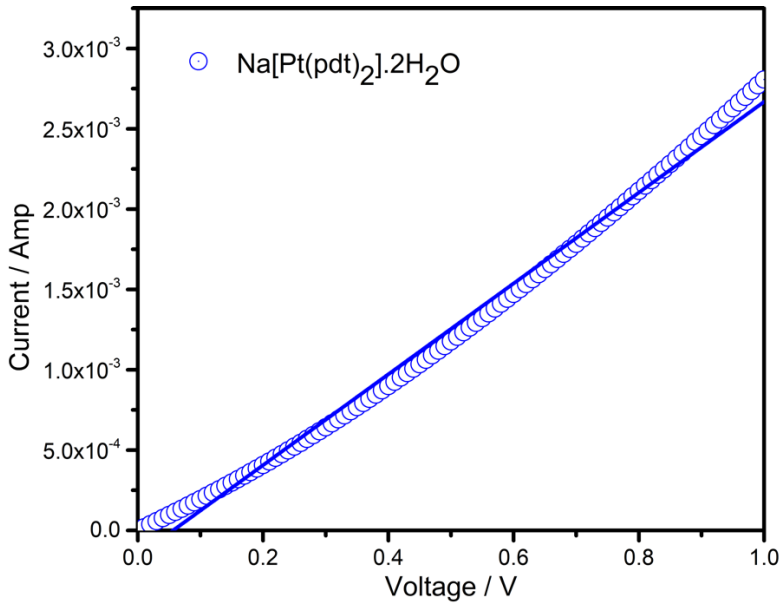

Figure 4.9.3 *I-V* characteristic of $Na[Pt(pdt)_2].2H_2O$ using pressed pellet sample at room temperature.

4.10 Thermoelectromotive force measurement

We investigated the charge carrier type using thermoelectromotive force measurement. **Figure 3.10** shows a plot of generation of ΔV when there is temperature difference of ΔT

applied. Negative of the slope of the plot gives the value of Seebeck coefficient. $Na[Pt(pdt)_2].2H_2O$ exhibited a Seebeck coefficient of +570 μVK^{-1} , positive sign of the Seebeck coefficient reveal that it's a p-type semiconductor with holes as a majority of charge carriers.

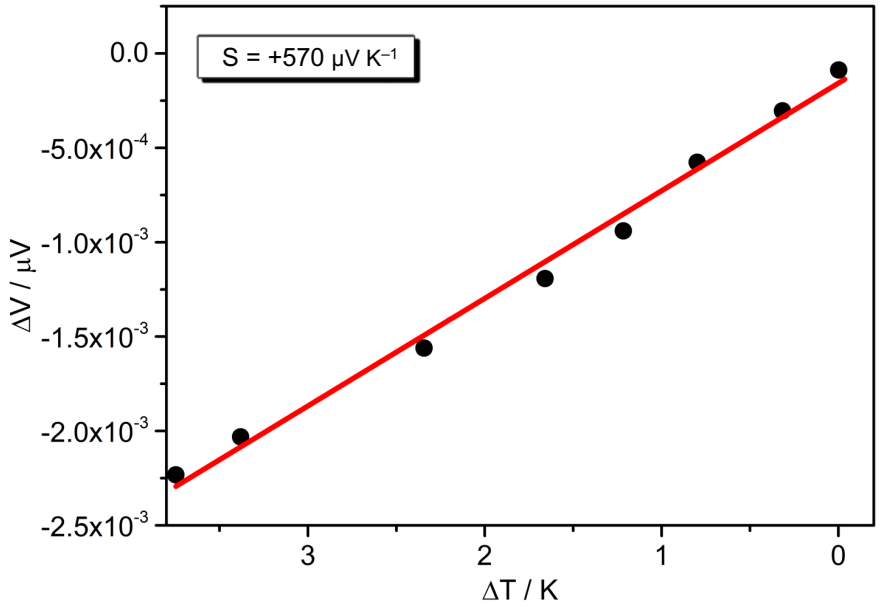

Figure 4.10 Thermoelectromotive force

4.11 Magnetic resonance Spectroscopy

In order to investigate the magnetic behavior of $Na[Pt(pdt)_2].2H_2O$, variable- temperature dc magnetic susceptibility data were collected at 1000 Oe, and the resulting plots of $\chi_M T$ and χ_M vs T are shown in **Figure 4.11** (χ_M = molar magnetic susceptibility). It can be seen that $\chi_M T$ shows a linear relationship with temperature. For $Na[Pt(pdt)_2].2H_2O$, considering the Pt center in +III oxidation state the expected magnetic moment corresponds to S = 1/2 is 0.375 cm^3 K/ mol at room temperature. However, the

experimental result shows $\chi_M T$ value of 1.2 cm^3 K/ mol per formula unit indicating that the obtained value is significantly higher than the theoretical one.

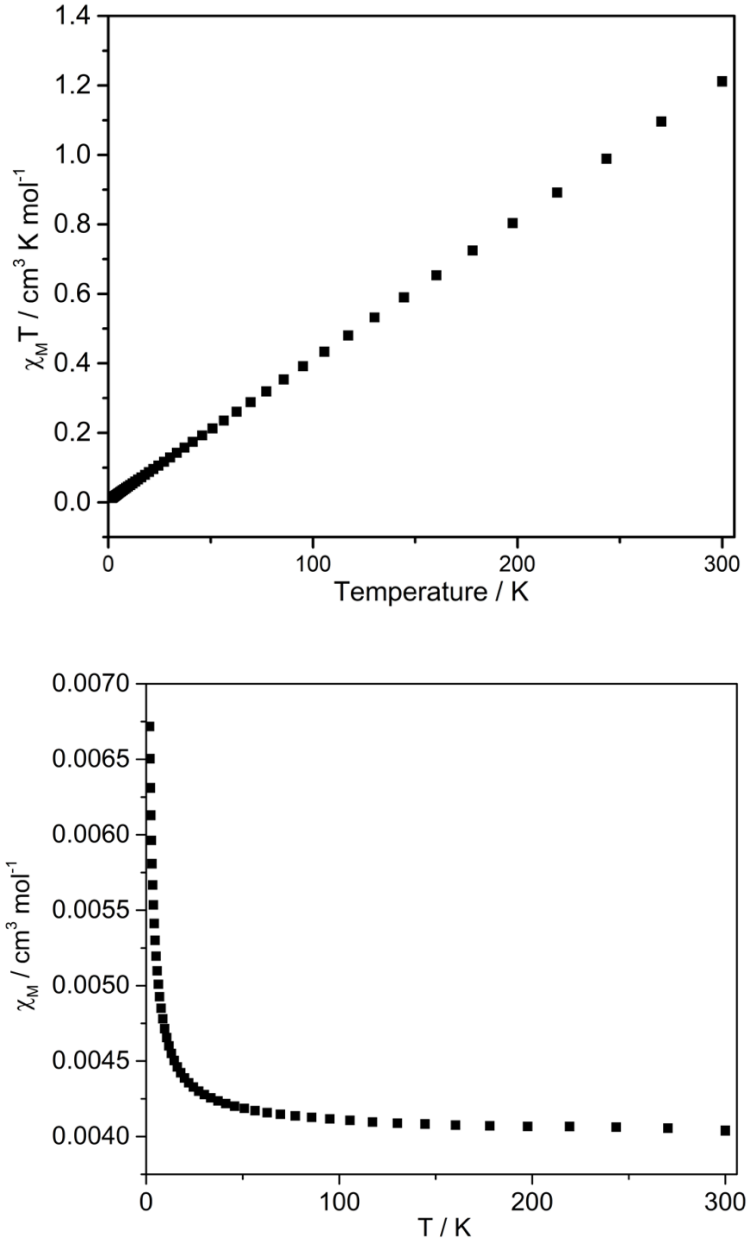

Figure 4.11 (a) Plot of $\chi_M T$ vs temperature and **(b)** Plot of χ_M vs temperature

4.12 Conclusion

In this work, we have reported a 3-D conducting coordination polymer using Platinum and 2,3-pyrazene dithiol ligand. The polymer was synthesized using electro-crystallization technique. Crystal structure analysis reveals that it has face-to-face stacking along *a*-axis, which resulted in a 3-dimensional coordination polymer. Cyclic voltammetry measurement showed that the polymer exhibited $1e^-$ reversible redox behavior. The electron being removed is located in the SOMO. Which has a contribution from metal as well as ligand. Since the SOMO has a comparatively large contribution from the ligand hence, the electron is localized on the ligand. This result also supported by the XANES, ESR and DFT calculations. Thermal stability investigation illustrates that the polymer was stable up to 180 ^oC. The polymer exhibited a relatively high electrical conductivity of 1.6×10^{-2} Scm^{-1}. Such a high electrical conductivity is a result of π–π interaction between the organic core along the *a*-axis. The strong π–π interaction leads to a 1D π stacked column which provides the pathway for the electron delocalization in the direction of stacking. Further charge carrier type investigation was performed using thermoelectromotive force measurement. Where, the positive sign of the Seebeck coefficient indicates that holes are the majority charge carrier. Considering the fact that it has an unpaired electron, we investigated the temperature dependence of magnetic susceptibility and it was found that $\chi_M T$ shows a linear relationship with temperature. However, the experimental result shows $\chi_M T$ value of 1.2 cm^3 K/ mol per formula unit at room temperature, indicating that the obtained value is significantly higher than the theoretical one. Unfortunately, at this moment we do not have appropriate reasoning to explain such a magnetic behavior.

Reference:

(1) Eduok, E. E.; Krawiec, mariusz; Buisson, Y.-S. L.; O'Conner, C. j.; Sun, D.; Watson, W. H. Structure and Properties of Transition Metal Complexes of Naphthoquinonedithiolate. *J Chem Crystallogr* **1996**, *26* (9), 621–638. https://doi.org/10.1007/BF01668623.

(2) Hummel, H.-U. Synthesis and X-Ray Crystal Structure of Tetraethylammonium Bis[1, 1-Dicyanoethylene-2, 2-Dithiolato]Platinate(II). *Transition Met Chem* **1987**, *12* (2), 172–174. https://doi.org/10.1007/BF01022349.

(3) Holm, R. H.; Chakravorty, A.; Theriot, L. J. The Synthesis, Structures, and Solution Equilibria of Bis(Pyrrole-2-Aldimino)Metal(II) Complexes. *Inorg. Chem.* **1966**, *5* (4), 625–635. https://doi.org/10.1021/ic50038a028.

(4) Cl.1987.Pdf.

(5) Cl.1993.Pdf.

(6) *PII: 0010-8545(91)80024-8 | Elsevier Enhanced Reader*. https://doi.org/10.1016/0010-8545(91)80024-8.

(7) Ja00896a028.Pdf.

(8) Martín, N.; Segura, J. L.; Seoane, C. Design and Synthesis of TCNQ and DCNQI Type Electron Acceptor Molecules as Precursors for 'Organic Metals.' *J. Mater. Chem.* **1997**, *7* (9), 1661–1676. https://doi.org/10.1039/a702314f.

(9) *PII: 0379-6779(90)90025-G | Elsevier Enhanced Reader*. https://doi.org/10.1016/0379-6779(90)90025-G.

Chapter- 5. Conclusion

5.1 Conclusion

In this work, we have reported electrically conductive coordination polymers that exhibit redox activity based on metal or ligand. Semiconducting and Thermoelectric properties were investigated. Thermoelectromotive force measurement was incorporated in order to investigate conductive carriers. Thermoelectromotive force is well-known among thermoelectric materials to investigate the electronic structure and find the efficiency of the material in converting heat into electrical energy. And it's a new concept in the field of MOF chemistry. Where, this can be used to investigate conducting carrier types in case of conductive MOF. And the study in this work shows that in the MOFs, if the metal centre is in the easily accessible reduced state, which means that charge carrier of holes can be generated thermally. This implies that the fermi energy level will be close to the valence band and hence it's a p-type semiconductor. Whereas, if the metal centre is in the easily accessible oxidized state, which means that charge carrier of electrons can be generated thermally. This implies that fermi energy level will be close to the conduction band and hence it's an n-type semiconductor. In chapter 2, we presented the extended application range of the $Cu[Cu(pdt)_2]$ MOF in the field of electronics. For the first time, we reported the change in the Seebeck coefficient of MOFs via halogen doping. Conducting carrier has changed from holes to electrons after a certain fraction of halogen doping while maintaining the original structure. And halogen doping causes an appreciable amount of enhancement in the electrical conductivity. The improved conductivity and device engineering will make this material a versatile candidate for the field of MOF-based electronic devices. $Cu[Cu^{II}(pdt)_2]$ possesses holes as conductive carriers and act as p-type semiconductor and upon halogen doping $[Cu^{II}(pdt)_2]$ oxidizes to $[Cu^{III}(pdt)_2]$.

$[Cu^{II}(pdt)_2]^{2-}$ can easily be oxidized to $[Cu^{III}(pdt)_2]^{-}$, while is hardly reduced to $[Cu^{I}(pdt)_2]^{3-}$, indicating that the charge carriers of hole are thermally generated, in other words, the Fermi energy (E_F) is closer to top of the valence band than bottom of the conduction band. Which means that it is a p-type semiconductor. On the other hand, the bromine-doped compound is in the $[Cu^{III}(pdt)_2]^{-}$ state, which can easily be reduced to $[Cu^{II}(pdt)_2]^{2-}$ whereas hardly oxidized to $[Cu^{IV}(pdt)_2]^{0}$, indicating that the charge carriers of an electron are thermally generated (n-type semiconductor).

In chapter 3 we reported neutral electrically conducting MOF $Fe^{III}_2dhbq_3$. And the MOF possess redox activity based on metal as well as ligand. It exhibited significantly high electrical conductivity of 1.2×10^{-2} S cm^{-1}at 300 K as a result of strong covalency between metal and ligand. The majority of charge carrier was found to be electron investigated by thermoelectromotive force measurements. In the case of $Fe^{III}_2dhbq_3$, for Fe^{III} it is easy to reduce to Fe^{II} rather than to oxidize to Fe^{IV} ,(which is also supported by the cyclic voltammetry measurement), indicating that the charge carriers of electrons are thermally generated, in other words, the Fermi energy (E_F) is closer to bottom of the conduction band (n-type semiconductor). Upon fabricating the MOF as a cathode for a LIB, it showed a significantly high specific capacity (322 mA h / g) while undergoing first discharge. Such a high value of discharge capacity is the result of the many-electron uptakes which was consistent with the result obtained by solid CV. In chapter 4, we have reported a 3-D conducting coordination polymer $Na[Pt(pdt)_2].2H_2O$ using Platinum and 2,3-pyrazene dithiol ligand. It has face-to-face stacking along *a*-axis, which results in a 3-dimensional coordination polymer. Cyclic voltammetry measurement showed that the polymer exhibited $1e^-$ reversible redox behavior based on metal. The polymer exhibited a relatively

high electrical conductivity of 1.6×10^{-2} Scm^{-1}. Such a high electrical conductivity is a result of π–π interaction between the organic core along the *a*-axis. The strong π–π interaction leads to a 1D π stacked column, which provides the pathway for the electron delocalization in the direction of stacking. Further charge carrier type investigation was performed using thermoelectromotive force measurement. Where the positive sign of the Seebeck coefficient indicates that holes are the majority charge carrier. For $Na[Pt(pdt)_2].2H_2O$, Since Pt is in +III oxidation state and for Pt both the oxidation state (i.e. reduced form Pt^{II} and oxidized one Pt^{IV}) are accessible as there are already reports on Pt^{II} and Pt^{IV} complexes. At this moment, we do not have idea most easily accessible oxidation state. Although, based on the results obtained from the thermoelectromotive force (as it's a p-type semiconductor), it seems that for Pt^{III} it is easier to oxidize to Pt^{IV} rather than to reduce to Pt^{II} .

Acknowledgements

First and foremost, my sincere gratitude goes to Professor Masahiro Yamashita for providing me with the opportunity to pursue my PhD in his well-equipped lab. His passion for science is incredibly impressive that not just motivated me but a thousand researchers as well. I felt an honor to meet him personally and to know him.

I must thank Professor Ryota Sakamoto for providing me a well-equipped laboratory and all the facilities to pursue my research. I have to thank my supervisor, Associate Professor Shinya Takaishi. Without his guidance and engagement, this work would not have been possible. There are so many things for which I will always be extremely grateful to him. He has been very humble to each of the lab members. He taught us how not to just focus on the end results but to embrace each failure and try to find the explanation for that, try to find what is actually happening. He helped me in many ways, including teaching new techniques, how to solve a problem, measuring diffuse reflectance spectra, Seebeck coefficient, *I-V* characteristic and so on. Thank you so much for all your support and advice over the last three years.

I would like to thank Assistant Professor Hiroaki Iguchi for his constant support throughout my research. His valuable suggestions in the group meetings helped me a lot in tackling the problems. He was always ready to help me whenever I needed him. I really appreciate his management skills. How beautifully he managed the lab along with the research.

I want to thank every member of the lab for their valuable suggestions and constant help especially Mr Tetsu Sato. He helped me a lot in learning new skills, new techniques, and finding solutions to problems. I really enjoyed discussing research-related problems and results with him. Mr Koyama for helping me doing theoretical calculations and finding charge transfer integral. Mr Tanaka for teaching me to perform solid state electrochemistry. I am grateful to Japan International Corporation Agency (JICA) for helping me fulfil my dream of doing PhD in Japan by providing the Scholarship. Other than the academic support, I have to thank many people for their emotional support throughout this journey. Thanks to my parents for believing in me and giving me the freedom to shape my career. Everything was impossible for me without your unconditional love and motivation. My senior, Mr Bishnubasu Giri for always providing me the right track, and teaching me how to think about problem solving. My friend Mr. Anand Anil Kadu, for always standing by my side like a family.